The Gulf Stream:
Along-stream evolution of volume transport and water properties observed by underwater gliders

by

Joleen Heiderich

Bachelor of Science, Jacobs University Bremen, 2015

Submitted to the Department of Earth, Atmospheric and Planetary Sciences
in partial fulfillment of the requirements for the degree of

Doctor of Philosophy

at the

MASSACHUSETTS INSTITUTE OF TECHNOLOGY

and the

WOODS HOLE OCEANOGRAPHIC INSTITUTION

September 2021

Signature of Author . . . .
Joint Program in Oceanography/Applied Ocean Science & Engineering
Massachusetts Institute of Technology & Woods Hole Oceanographic Institution
August 27, 2021

Certified by . . . .
Dr. Robert E. Todd
Thesis Supervisor
Woods Hole Oceanographic Institution

Accepted by . . . .
Prof. Glenn R. Flierl
Chair, Joint Committee for Physical Oceanography
Massachusetts Institute of Technology & Woods Hole Oceanographic Institution

The Gulf Stream:
Along-stream evolution of volume transport and water properties observed by underwater gliders

by

Joleen Heiderich

Submitted to the Department of Earth, Atmospheric and Planetary Sciences
on August 27, 2021, in partial fulfillment of the requirements for the degree of
Doctor of Philosophy
at the Massachusetts Institute of Technology
and the Woods Hole Oceanographic Institution

Abstract

The Gulf Stream, the western boundary current of the subtropical North Atlantic, plays a key role in the Earth's climate system with its poleward volume and heat transports being major components of the upper limb of the Atlantic Meridional Overturning Circulation. Extensive observations collected using Spray autonomous underwater gliders from 2004 through 2020 fill a 1500-km-long gap in longer-term sustained subsurface measurements of the Gulf Stream. The gliders provide concurrent, high-resolution measurements of Gulf Stream hydrography and velocity over more than 15 degrees of latitude between Florida and New England. These observations are used to characterize the along-stream evolution of Gulf Stream volume transport; its long-known poleward increase is shown to result primarily from entrainment of subthermocline waters. Antarctic Intermediate Water, which makes up the deepest waters within the Gulf Stream in the Florida Strait, is eroded through both vertical mixing and lateral stirring as it flows downstream. Satellite-based observations of sea surface height coincident with the glider observations are used to evaluate the efficacy of inferring Gulf Stream transport from remotely sensed measurements. The detailed analyses of Gulf Stream transport and water property evolution herein provide targets for regional and global circulation models to replicate.

Thesis Supervisor: Dr. Robert E. Todd
Title: Associate Scientist
Woods Hole Oceanographic Institution

Acknowledgments

Even though there is only a single author listed on this document, it should not be forgotten that it takes the support and encouragement of many people to complete a PhD thesis. I have many people to thank who enriched my life both personally and academically over the past six years and who have made this journey unforgettable, rewarding, intense, and who filled it with laughter.

First and foremost, I would like to thank my advisor, Robert Todd. Seven years ago, I emailed him out of the blue and he decided to take me on as a Summer Student Fellow. After a short detour to polar oceanography, I returned to his glider lab to delve into Gulf Stream observations. Since then, I have learnt so much from him – from coding, to analyzing glider observations and understanding Gulf Stream dynamics, to what it means to be a scientist. I am grateful for his thoughtful feedback, availability for questions, attention to detail, and continued support (and for sending me on scientific quests around the world for both glider deployments and conferences).

This work would not have been possible without the invaluable input from my committee members Magdalena Andres, John Bane, Glenn Flierl, and John Toole. Frequent discussions with them and their detailed comments on all of my written drafts have made this final product so much better. I would also like to thank Jake Gebbie for chairing my defense and for his enthusiastic teaching in several of my courses. Together, my advisor and my committee have inspired me with their rigorous scientific approaches and deep insights into so many different fields. They have challenged me to be precise, carefully consider my words, and keep improving this work.

The basis of this entire thesis is a large observational program that surveys the Gulf Stream with autonomous underwater gliders. It takes many hands to keep such a program going and therefore I would like to thank all of the past and present members of the Todd lab: Kyle Kausch, Julie Jakoboski, Ray Graham, Larry George, and of course Patrick Deane. During countless compass calibrations and about 10 trips to Miami for glider deployments, Patrick has taught me so much about glider operations and the amount of work that is needed before we even get a single data point.

Over the past decade, I was fortunate to have the support from many scientific mentors and friends who have inspired me with their creative approaches to science and their outlook on life in general. I would especially like to thank Lola Pérez, Wilken von Appen, and Glen Gawarkiewicz.

When I started this program, I never thought that I would end up studying the Gulf Stream. My first advisor, Fiamma Straneo, and her group – including Mattias Cape, Becca Jackson, and Nick Beaird – welcomed me to their lab with open arms and made the transition from Germany to the United States much easier. They have taught me a lot about subpolar oceanography and gave me the chance to join some of them for my first long research cruise to Greenland. I am incredibly grateful for these experiences and for the fact that Fiamma gave me the option to either remain in the Joint Program or to join her when moving to Scripps. She was very supportive when I decided to stay and both her and Robert made the transition to a new advisor

as smooth as possible.

I am glad that Robert accepted me as a student again in my second year of graduate school and that the timing aligned perfectly with working on this Gulf Stream project. I have never regretted the decision of staying in the MIT-WHOI Joint Program. The Joint Program community is special and I feel lucky to have been a part of it. The institution-wide open door policy makes it a welcoming environment and allowed me to meet so many extraordinary people over the past few years. The students and faculty, the Academic Programs Office and the PO department administrators, the technicians, engineers, and marine crews make this program as great and unique as it is. I also wish to thank the crew of the R/V *Neil Armstrong*, who I was fortunate enough to explore different parts of the North Atlantic with on several long cruises.

As a true "JP commuter", I have been a part of both the local Woods Hole community and the larger MIT community in Cambridge. Since the beginning of grad school, the MIT Rowing Club has been an important part of my life. I have been lucky to travel to China, Korea, and all over the northeast U.S. with them and I already miss the early morning workouts on the Charles. I also would like to acknowledge the MIT Ballroom Dance Team, who have kept me sane with virtual dance lessons over the pandemic.

On a more personal level, I would like to thank my friends, a lot of whom are Joint Program and EAPS students. The JP jellyfish and the PO students have been my biggest support system in all the ups and downs of grad school (and a global pandemic). I would not have made it through this program and especially the last years without Suzi Clark, Rachel Housego, Jen Karolewski, and Nathan Mollica. Time and time again, Suzi's and Rachel's support and care have shown me what true friendship is - not least when they surprised me for my defense. I could not ask for better friends. Jen and Mara Freilich have been with me through it all since we were summer student fellows seven years ago and I am sure that they will be among my best friends for many more years to come. Jing He and Astrid Pacini are some of the kindest people I know and I am incredibly grateful to have them in my life. Pamela Bellavita has not only been my roommate, rowing buddy, and fellow expat, but also a wonderful friend that I can rely on and stay in touch with even over long distances. Likewise, my fellow European Marianne Acker has been my constant source of support and commiseration for any issues related to homesickness and my favorite person to go out with in Cambridge. I cannot wait to join her on the other side of the Atlantic. Jake Forsyth has been my office mate for seven years and also was my co-chief scientist on a student-led R/V *Neil Armstrong* cruise. As the pandemic has shown, being in the office without him is much less fun. I would like to thank him for the "sometimes actual scientific conversations" (as he put it) and for always being available for questions, silly bets, and other shenanigans. Moreover, grad school would not have been the same without the following wonderful people: Chrissy Hernandez, Kevin Archibald, Lizzie Wallace, Ryan O'Shea, Eesh Bhatt, Laura Fleming, Jeffrey Mei, Sam Levang, Emma Homstad, Bethany Fowler, and Scotty Stevens. Besides the people that I met in Boston, I count myself lucky to have a network of friends around the world, many of whom have visited me during my time in Massachusetts.

I especially would like to acknowledge Paula Möhlenkamp, Johannes Hansen, Andrei Ignat, and my host families in Bolivia and Spain.

Last, but certainly not least, I would like to give a huge thank you and shout-out to family. They are the most important people in my life and the reason why I have no second thoughts about leaving all the wonderful people in the U.S. behind and and moving back to Europe. By setting phenomenal examples, my family has shaped me into the person that I am today and I am certain that I would not have persevered without them. They have supported me in all of my decisions, even when those have sent me to two different continents for extended periods of time. Even when I am physically far away, we have always figured out how to remain close and how to be there for each other remotely. Every time I leave makes me realize even more how much I value home and my family. I cannot put it into words how much it means to me that I can count on them and that I have a safe and supportive place to return to that accepts me for who I am with all of my crazy ideas and plans.

Many more people were critical to the success of the Spray glider missions, including Ben Hodges and Breck Owens at WHOI and Dan Rudnick, Ben Reineman, Jeff Sherman, and Evan Randall-Goodwin of the Instrument Development Group at the Scripps Institution of Oceanography. The Physical Oceanography Division at NOAA's Atlantic Oceanographic and Meteorological Laboratory (AOML) and the University of Miami's Rosenstiel School of Marine and Atmospheric Science (RSMAS) provided laboratory space for glider preparation. The East Carolina University Coastal Studies Institute and North Carolina State University's Center for Marine Sciences and Technology (CMAST) provided support for glider recoveries.

We gratefully acknowledge funding from the National Science Foundation (OCE-0220769, OCE-1633911, OCE-1923362, OCE-1558521), NOAA's Global Ocean Monitoring and Observing Program (NA14OAR4320158, NA19OAR4320074), the Office of Naval Research (N000141713040), WHOI's Oceans and Climate Change Institute, Eastman Chemical Company, and the W. Van Alan Clark, Jr. Chair for Excellence in Oceanography at WHOI (awarded to Breck Owens).

Spray glider observations in the Gulf Stream are available from `http://spraydata.ucsd.edu` and should be cited using the following DOI: 10.21238/S8SPRAY2675 (Todd and Owens 2016). Line W shipboard hydrographic data are accessible from the Line W project website (`https://scienceweb.whoi.edu/linew/index.php`). The daily delayed-time (SEALEVEL_GLO_PHY_L4_REP_OBSERVATIONS_008_047) and near-real-time (SEALEVEL_GLO_PHY_L4_NRT_OBSERVATIONS_008_046) absolute dynamic topography products used in this study are provided by the EU Copernicus Marine Environmental Monitoring Service. Figures utilize color pallets suggested by Thyng et al. (2016).

Contents

List of Figures

List of Tables

Chapter 1

Introduction

The Gulf Stream is a fast ($\mathcal{O}(1)$ m s^{-1}) and narrow ($\mathcal{O}(100)$ km) oceanic current that originates in the Florida Strait as a continuation of the Gulf of Mexico Loop Current. It flows along the eastern coastline of the United States before separating from the coast near Cape Hatteras and heading towards Europe. As the western boundary current of the subtropical North Atlantic Ocean (i.e., a current that flows along the western side of the North Atlantic Ocean basin), the Gulf Stream carries warm, salty waters from the tropics to higher latitudes (Fig. 1-1), thereby playing a crucial role in poleward heat transfer (e.g., Wunsch 2005; Cunningham et al. 2007) and regional and global climate (e.g., Kwon et al. 2010). The Stream affects regional sea level through changes in its strength, position, and eddy shedding (e.g., Blaha 1984; Noble and Gelfenbaum 1992; Vellinga and Wood 2008; Ezer 2016). Moreover, the Gulf Stream influences marine ecosystems and consequently plays a role in the global carbon cycle through the redistribution and upwelling of nutrients associated with its front, eddies, and rings (e.g., Redfield 1936; Yoder et al. 1983; Lee et al. 1991; Palter and Lozier 2008; Schmittner and Galbraith 2008; Hoarfrost et al. 2019). As a large reservoir of kinetic energy, the Gulf Stream stirs the ocean on a variety of scales and is therefore important for the ocean energy budget (e.g., Wyrtki et al. 1976). Along its way (i.e., in the along-stream direction), the Gulf Stream traverses different regions that affect its dynamics, stability, and properties.

Using a large set of observations collected by autonomous underwater vehicles called Spray gliders (Sherman et al. 2001) in combination with other observations, this thesis investigates how the Gulf Stream evolves in the along-stream direction.

In particular, the work focuses on the along-stream evolution of Gulf Stream volume transport (Chapters 2 and 4) and the corresponding changes in the properties of the waters making up the poleward flow (Chapters 2 and 3). This introduction provides the overall scientific context and motivation for this thesis. Section 1.1 reviews western boundary current theories that explain the existence of the Gulf Stream and the Deep Western Boundary Current that it interacts with. Section 1.2 presents a brief overview of how the Gulf Stream has historically been observed, while section 1.3 identifies open questions in the scientific literature that motivate this thesis. The main data sets analyzed in this thesis, particularly the glider observations, are introduced in section 1.4. Section 1.5 lays out a road map for the remaining chapters.

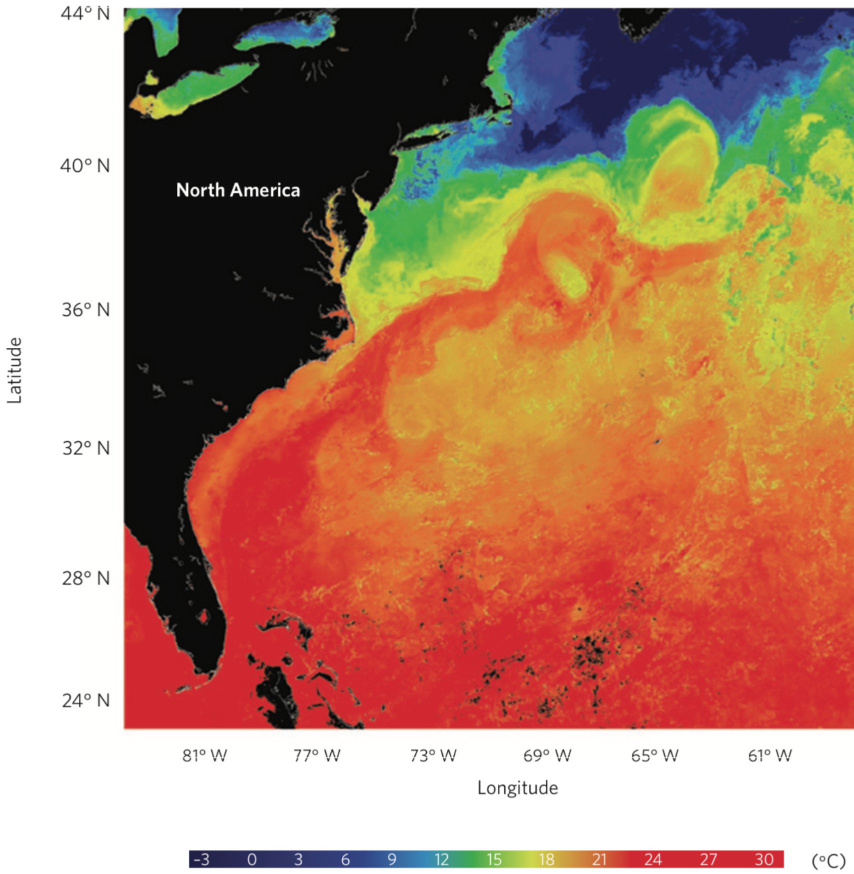

Figure 1-1: Satellite image of sea surface temperature in the western North Atlantic. Red colors indicate warmer temperatures (e.g., the Gulf Stream) and blue colors indicate colder temperatures. This image is a composite of cloud-free NASA MODIS data from 13 to 21 May 2006 with any remaining missing data replaced by a monthly composite. Figure from Williams (2012).

1.1 The Gulf Stream: a western boundary current

The large-scale ocean circulation significantly influences global climate through the redistribution of heat and salt (e.g., Wunsch 2005) and its effects on the carbon cycle (e.g., Schmittner and Galbraith 2008). The global ocean circulation is driven by two main forcing mechanisms: wind and buoyancy. The wind-driven circulation is dominated by the prevailing global wind pattern consisting of polar easterlies, midlatitude westerlies, and easterly trade winds in the tropics. Changes in buoyancy caused by evaporation, precipitation, brine rejection, and surface cooling at higher latitudes lead to thermohaline overturning and drive a flow called the Meridional Overturning Circulation (MOC, or AMOC in the Atlantic).

Both the wind-driven and the overturning circulation require strong and narrow currents along the basin's western boundary for dynamic consistency. In both Stommel's (1948) and Munk's (1950) theories of the wind-driven circulation, the interior ocean is assumed to be in Sverdrup balance (Sverdrup 1947). Strong western boundary currents are needed to balance the wind stress curl over the rest of the ocean basin. While Stommel's solution dissipates energy in the western boundary current via bottom friction, Munk suggests lateral friction as the acting dissipative mechanism. Stommel and Arons's (1959) theory for the abyssal circulation also invokes western boundary currents at depth to close the circulation. Specifically, Stommel and Arons predict abyssal poleward flow towards deep water sources in the interior ocean basins based on vertical stretching caused by deep water formation. To satisfy continuity requirements and conservation of a dynamical tracer called potential vorticity, the flow needs to be balanced by an equatorward directed western boundary current.

These simplified theories capture large-scale ocean circulation patterns quite well: western boundary currents are indeed observed in all ocean basins in both hemispheres. However, Munk's and Stommel's models underestimate western boundary current transports. Furthermore, both models assume a homogeneous ocean with a flat bottom and only describe steady circulations without the consideration of instabilities. Theories predicting the structure and transport of western boundary currents can be improved by considering nonlinear inertial boundaries (Fofonoff 1954; Charney 1955), stratification and bathymetry (Holland 1972), or an unstable jet with eddy recirculations (Rhines and Holland 1979; Holland and Rhines 1980). Moreover, Parsons's (1969) simple two-layer model with a surfacing isopycnal provides an explanation for the observed separation of western boundary currents from the coast.

In the North Atlantic, the wind-driven circulation forms both a subtropical and a subpolar gyre. The thermohaline circulation consists of cold, deep water formed at high latitudes in the Labrador, Greenland, Iceland, and Norwegian Seas that is transported equatorward and replaced by a warm return flow at the surface. There are several western boundary currents in the North Atlantic, including the Gulf Stream and the Labrador Current (which both balance the wind-driven Sverdrup circulation and are the western boundary currents of the subtropical and subpolar gyres, respectively), and the Deep Western Boundary Current (which is often abbreviated as DWBC and balances the thermohaline circulation).

The AMOC consists of both deep and surface boundary currents. The Gulf Stream is a major component of the upper limb of the AMOC in the subtropical gyre, carrying warm, saline waters poleward as it follows the eastern seaboard of the U.S. before separating from the continental margin near Cape Hatteras, North Carolina. The Labrador Current reaches from Baffin Bay and Hudson Strait to the tail of the Grand Banks of Newfoundland and transports cold and relatively low salinity water southward at the surface. The DWBC is a deep limb of the AMOC that carries cold water masses that are collectively termed North Atlantic Deep Water (NADW) from the tail of the Grand Banks of Newfoundland equatorward (Pickart and Watts 1990).

The Gulf Stream and the DWBC carry waters that originate in widely separated source locations and that consequently have different properties and ages. The NADW in the DWBC is comprised of Labrador Sea Water (LSW; an intermediate water mass that is formed by deep convection in the Labrador Sea) and denser, deeper Overflow Waters (Andres et al. 2018). Among the waters carried by the Gulf Stream is an intermediate water mass (i.e., a water mass that is found at middepths in the ocean) called Antartic Intermediate Water (Tsuchiya 1989; Szuts and Meinen 2017), which originates in the polar southern hemisphere as the name suggests. Shallower water masses in the Gulf Stream are entrained from the surrounding areas like the subtropical gyre and the shelf and slope regions (e.g., Ford et al. 1952; Worthington 1959; Talley and McCartney 1982; Toole et al. 2011; Qu et al. 2013).

Where the DWBC encounters the Gulf Stream, waters of different properties and origins interact with and influence each other. The DWBC crosses underneath the Gulf Stream at Cape Hatteras, where part of it is entrained back into the abyssal interior (Bower and Hunt 2000a,b; Pickart and Smethie 1993) with the balance continuing to flow equatorward along the western boundary (Hogg and Stommel 1985). Interactions between the Gulf Stream and the DWBC and the associated pathways and mechanisms have long been the focus of a variety of studies, both at Cape Hatteras and elsewhere (e.g., Talley and McCartney 1982; Thompson and Schmitz 1989; Spall 1996a,b; Bower and Hunt 2000a,b; Pickart and Smethie 1993; Toole et al. 2011; Rhein et al. 2015; Andres et al. 2018). Since the Gulf Stream is a surface intensified current while the DWBC is a deep current, the shallowest layer of the DWBC (namely Labrador Sea Water) may be prone to interactions with the Gulf Stream through mixing and entrainment. Underwater gliders surveying the upper kilometer of the Gulf Stream frequently observe the upper layer of Labrador Sea Water (uLSW) along most of the U.S. East Coast, suggesting interactions between the Gulf Stream and the DWBC. Among the water masses that uLSW may interact with is Antarctic Intermediate Water, since they are both found at similar depths.

1.2 History of Gulf Stream observations

Mariners have known about the existence of a strong current in the western North Atlantic since the 16th century due to its effects on navigation (MacLeish 1989; Richardson and Adams 2018). The earliest known chart of the Gulf Stream (Fig. 1-2) was created by Benjamin Franklin based on the reports of Captain Folger, a whaler from Nantucket who informed him about the “course, strength, and extent” of the current.

R E M A R K S

Upon the Navigation from

NEWFOUNDLAND TO NEW-YORK,

In order to avoid the

GULPH STREAM

On one hand, and on the other the SHOALS *that lie to the Southward of Nantucket and of St. George's Banks.*

AFTER you have paſſed the Banks of Newfoundland in about the 44th degree of latitude, you will meet with nothing, till you draw near the Iſle of Sables, which we commonly paſs in latitude 43. Southward of this iſle, the current is found to extend itſelf as far North as 41° 20′ or 30′, then it turns towards the E. S. E. or S. E. ¼ E.

Having paſſed the Iſle of Sables, ſhape your courſe for the St. George's Banks, ſo as to paſs them in about latitude 40°, becauſe the current ſouthward of thoſe banks reaches as far North as 39°. The ſhoals of thoſe banks lie in 41° 35′.

After having paſſed St. George's Banks, you muſt, to clear Nantucket, form your courſe ſo as to paſs between the latitudes 38° 30′ and 40° 45′.

The moſt ſouthern part of the ſhoals of Nantucket lie in about 40° 45′. The northern part of the current directly to the ſouth of Nantucket is felt in about latitude 38° 30′.

By obſerving theſe directions and keeping between the ſtream and the ſhoals, the paſſage from the Banks of Newfoundland to New-York, Delaware, or Virginia, may be conſiderably ſhortened; for ſo you will have the advantage of the eddy current, which moves contrary to the Gulph Stream. Whereas if to avoid the ſhoals you keep too far to the ſouthward, and get into that ſtream, you will be retarded by it at the rate of 60 or 70 miles a day.

The Nantucket whale-men being extremely well acquainted with the Gulph Stream, its courſe, ſtrength and extent, by their conſtant practice of whaling on the edges of it, from their iſland quite down to the Bahamas, this draft of that ſtream was obtained from one of them, Capt. Folger, and cauſed to be engraved on the old chart in London, for the benefit of navigators, by

B. FRANKLIN.

Note, The Nantucket captains who are acquainted with this ſtream, make their voyages from England to Boſton in as ſhort a time generally as others take in going from Boſton to England, viz. from 20 to 30 days.

A ſtranger may know when he is in the Gulph Stream, by the warmth of the water, which is much greater than that of the water on each ſide of it. If then he is bound to the weſtward, he ſhould croſs the ſtream to get out of it as ſoon as poſſible.

B. F.

Figure 1-2: Early chart of the Gulf Stream by Franklin (1786). Retrieved from the Library of Congress (`https://lccn.loc.gov/2004627238`).

The diagram appeared in the Transactions of the American Philosophical Society around 1786. Franklin noted that the Gulf Stream is characterized "by the warmth of the water, which is much greater than that of the water on each side of it".

Since Franklin's time, our knowledge of the Gulf Stream has vastly expanded, making it one of the best studied ocean currents on Earth. For many years, most Gulf Stream studies were limited to short-term experiments in isolated locations and shipboard transects across the current (e.g., Webster 1961, 1965; Oort 1964; Knauss 1969; Brooks and Niiler 1977; Rossby 1987). Over the last few decades, there have been several long-term observational programs surveying the Gulf Stream (observational transects corresponding to these programs are indicated in red in Fig. 1-3). Examples are the PEGASUS program at 73°N (1980–1983; Halkin and Rossby 1985), the SYNoptic Ocean Prediction (SYNOP) moored arrays between Cape Hatteras and the Grand Banks (1987–1990; Hogg 1993; Johns et al. 1995; Shay et al. 1995; Watts et al. 1995), the Gulf Stream Observations (GUSTO) mooring at 68°W (1982–1983; Hall and Bryden 1985; Hogg 1992), and Line W. The Line W mooring and hydrographic line at 39°N monitored the DWBC and Gulf Stream from 2004 to 2014 (Toole et al. 2011, 2017).

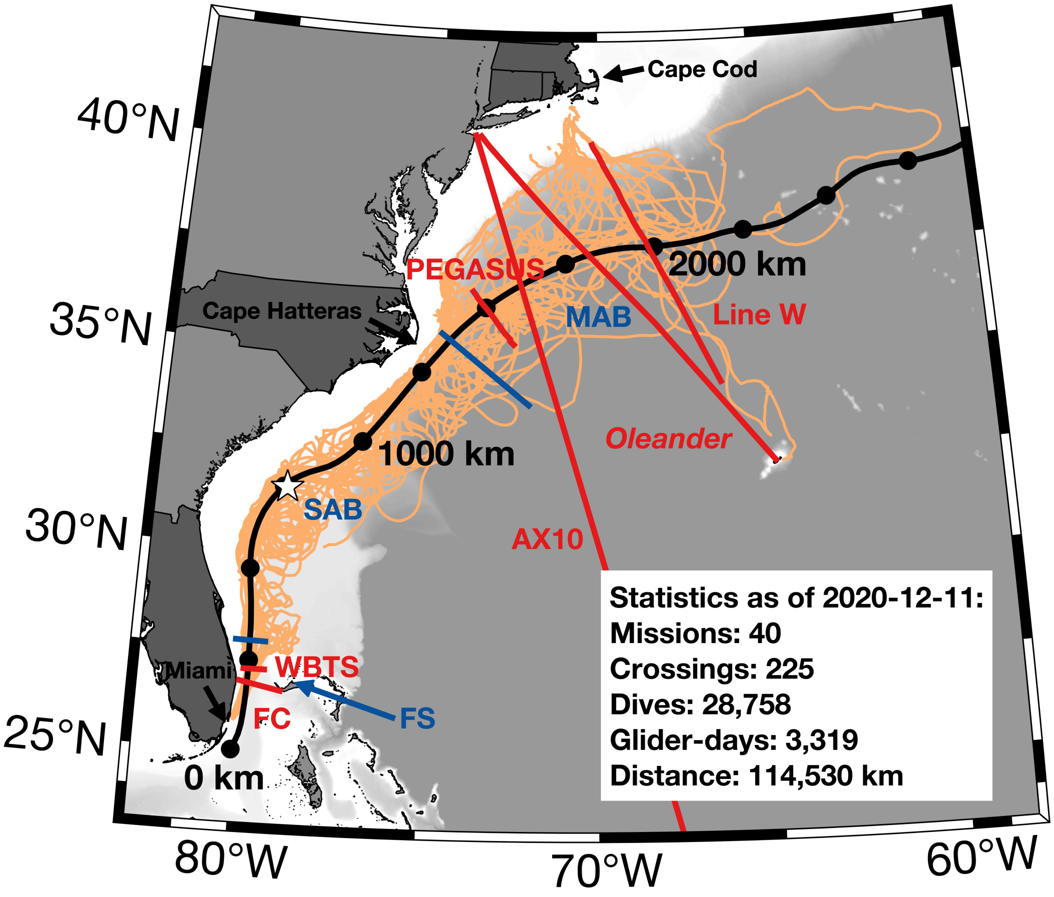

Figure 1-3: Trajectories of all Spray glider missions in and near the Gulf Stream that are used in this thesis (orange). Locations of in situ Gulf Stream observations from other long-term programs (red): the Florida Cable (FC) and routinely occupied ship transect of the Western Boundary Time Series (WBTS), the CMV *Oleander* line, the AX10 line, the PEGASUS line near 73°W, and Line W. The mean 40-cm SSH contour averaged over 17 calendar years (1 January 2004–31 December 2020) represents the mean Gulf Stream position and provides an along-stream coordinate system (black with dots every 250 km). Blue lines delineate different dynamical regions: the Florida Strait (FS), South Atlantic Bight (SAB), and Middle Atlantic Bight (MAB). The white star denotes the location of the Charleston Bump. From south to north, Florida, North Carolina, and the New England states are highlighted in dark gray, and important locations are indicated with arrows. Glider mission statistics are displayed in the inset box in the lower right.

Sustained, subsurface measurements of the Gulf Stream are currently only conducted in three locations along the U.S. East Coast: in the Florida Strait, along the CMV *Oleander* line between New Jersey and Bermuda, and along the AX10 line between Puerto Rico and New York (also indicated in red in Fig. 1-3). Voltage differences along submerged submarine telephone cables that span the Florida Strait near 26.5°N have been used to infer daily transports of the Florida Current (the upstream predecessor of the Gulf Stream) since 1982 (Baringer and Larsen 2001). These estimates are combined with a routinely occupied transect of nine CTD and Lowered Acoustic Doppler Current Profiler (LADCP) stations at 27°N to estimate property transports as part of the Western Boundary Time Series (WBTS), also known as the Florida Current Transport Time Series (Shoosmith et al. 2005). Repeat transects by the container vessel CMV *Oleander* have provided temperature profiles from eXpendable BathyThermographs (XBTs) since 1978 and velocities in the upper few hundred meters from a shipboard ADCP since 1992 (Flagg et al. 2006). Similar to the CMV *Oleander* line, the AX10 program has used a ship of opportunity to collect upper ocean XBT temperature profiles since 1992 (Goni et al. 2010; Molinari 2011). Both the CMV *Oleander* and AX10 lines cross the Gulf Stream downstream of its separation from the continental margin at Cape Hatteras. Historical estimates of Gulf Stream volume transport from a variety of these long-term observational programs are shown in Fig. 1-4.

Satellites can sample the surface of the global ocean over much broader scales in relatively short time periods compared to in situ instrument systems. Satellite remote sensing started about half a century ago in the 1970s (Fu and Cazenave 2001; Minnett et al. 2019) and has since been in integral part of many Gulf Stream studies (e.g., Bane et al. 1981; Brooks and Bane 1983; Hood and Bane 1983; Lee et al. 1981, 1991). It added a new layer to our understanding of the spatial complexity and variability of its surface signature (Legeckis 1975; Minnett et al. 2019), especially in terms of its meandering and shedding of warm and cold core rings downstream of Cape Hatteras. High resolution images of sea surface temperature (SST) obtained with satellite-based infrared and microwave radiometers show the rich meso-to-submesoscale structure

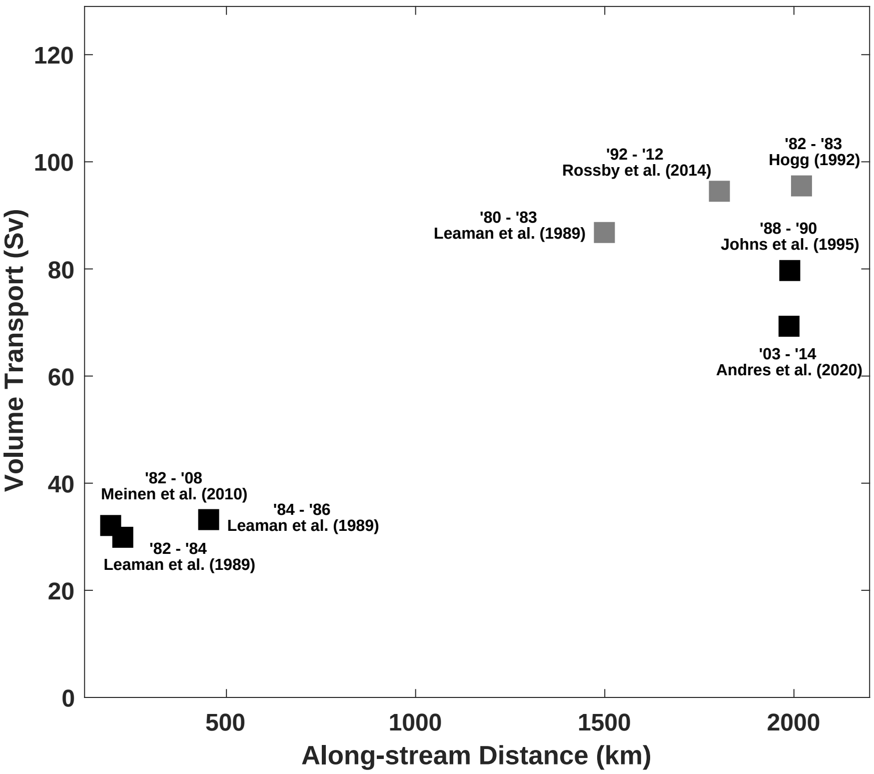

Figure 1-4: Historical estimates of Gulf Stream volume transport from observational programs lasting at least a year (in Sverdrup, where 1 Sv $\equiv 10^6$ m^3 s^{-1}). Plotted as a function of along-stream distance using the black coordinate system based on the mean 40-cm SSH contour in Fig. 1-3. Black squares indicate transport estimates to 1000-m depth or the bottom where the ocean is shallower than 1000 m, while gray squares show transport estimates to different depths. The time periods of the observations and the corresponding references are listed next to the squares. The transport estimates use data from the following observational programs: Meinen et al. (2010) – Florida Cable; Leaman et al. (1989) – three different PEGASUS lines, including the one near 73°W shown in Fig. 1-3; Rossby et al. (2014) – CMV *Oleander* line; Andres et al. (2020) – Line W; Johns et al. (1995) – SYNOP; Hogg (1992) – GUSTO mooring.

and strong gradients associated with the Gulf Stream and its eddies (e.g., Fig. 1-1). Satellite altimeters provide estimates of sea surface height (SSH) that can be used to derive geostrophic ocean surface currents. Satellites have been continually sampling the ocean providing near-global coverage since 1982 for SST (Strong et al. 2000) and 1991 for altimetry (Fu and Ubelmann 2014). They have been essential components of the Global Ocean Observing System (GOOS) since its formation in 1991.

1.3 Motivation for this thesis

The Gulf Stream is characterized by large cross-stream property gradients and high flow velocities ($\mathcal{O}(1)$ m s^{-1}). Consequently, high-resolution hydrographic and velocity measurements are required to capture Gulf Stream dynamics. To resolve the Gulf Stream's evolution along the U.S. East Coast, observational programs need to span multiple regions of the Gulf Stream that are governed by different dynamical regimes (separated by blue lines in Fig. 1-3): the Florida Strait (FS), the South Atlantic Bight (SAB), and the Middle Atlantic Bight (MAB). In the Florida Strait, the Gulf Stream flows through a channel between Florida and the Bahamas as a fairly straight meridional jet. As the current flows onto the relatively shallow ($\mathcal{O}(800)$ m) Blake Plateau in the South Atlantic Bight, it is still topographically stabilized and thus continues to flow as a relatively straight jet, except for some meandering downstream of the Charleston Bump (white star in Fig. 1-3), an underwater topographic feature (Bane and Dewar 1988; Gula et al. 2015). Once the Gulf Stream detaches from the continental slope at Cape Hatteras and enters the Middle Atlantic Bight, it becomes a freely meandering current that sheds warm and cold core eddies (e.g., Fig. 1-1).

Although the Gulf Stream has been studied for a very long time (section 1.2), observational campaigns have typically been conducted only at isolated locations and/or for relatively short periods of time, providing individual snapshots of Gulf Stream properties that are widely separated in space and/or time (e.g., Fig. 1-4). The wide variety of sampling methods employed further complicates intercomparison of various observational results. Moreover, contemporaneous measurements often stem from different dynamical regions in the Gulf Stream. While satellite remote sensing provides large-scale coverage of the surface expression of the Gulf Stream over relatively short time periods, it fails to capture the subsurface structure of the current.

In the Gulf Stream along the U.S. East Coast, an extensive field program using Spray autonomous underwater gliders (Fig. 1-5) provides regular, finescale, subsurface measurements of hydrography and velocity in the upper 1000 m of the ocean spanning more than 15° of latitude and filling in the 1500-km-long gap between the sustained subsurface Gulf Stream measurements in the Florida Strait and along the CMV *Oleander*/AX10 lines (see the black line with dots in Fig. 1-3 for distances, which represents an along-stream coordinate system based on the mean 40-cm SSH contour). These novel glider observations provide a unique opportunity to examine the evolution of Gulf Stream transport and water properties along the entirety of the U.S. East Coast.

The looming threat of changes to the Meridional Overturning Circulation as a consequence of anthropogenic climate change further motivates efforts to understand the current state and dynamics of the Gulf Stream. Climate forecasts predict a slow down of the AMOC under future climate scenarios (e.g., IPCC 2013, and references therein). While in situ measurements cannot yet detect any such slowdowns (Rossby et al. 2014), proxy-based reconstructions of past climate indicate likely slowing of the AMOC over the past century (e.g., Piecuch 2020; Caesar et al. 2021) and recent observational efforts have detected shifts in the Gulf Stream's meander envelope downstream of Cape Hatteras. Andres (2016) documented a recent upstream and westward shift of the location at which the Gulf Stream begins to meander down-

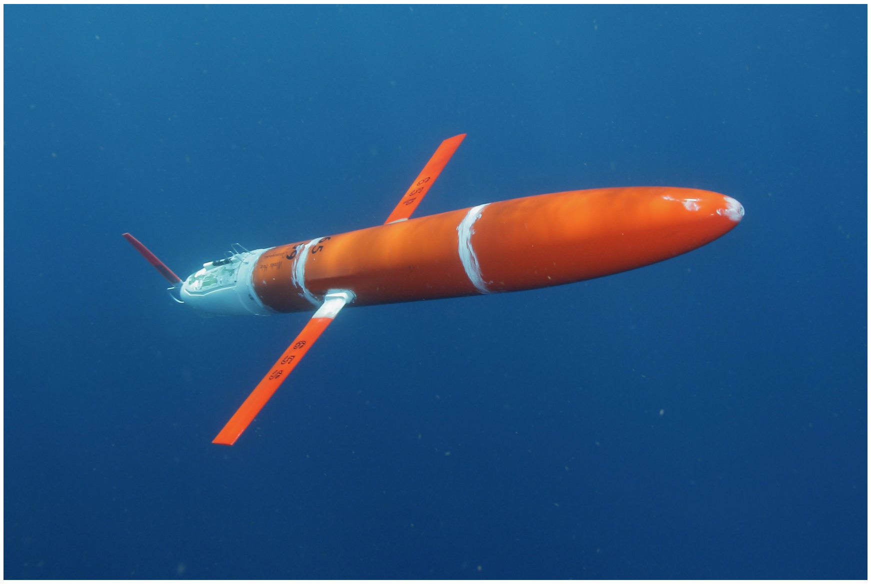

Figure 1-5: A Spray glider in the Gulf Stream. Image courtesy of Robert E. Todd, Woods Hole Oceanographic Institution.

stream of Cape Hatteras. As this destabilization point moves westward, the meandering Gulf Stream comes closer to the Middle Atlantic Bight continental margin and the equatorward currents that lie there, including the DWBC and the Middle Atlantic Bight shelfbreak jet (e.g. Linder and Gawarkiewicz 1998; Gawarkiewicz et al. 2018). Occasional strong deviations from mean meander tracks both upstream and downstream of Cape Hatteras have been detected (Gawarkiewicz et al. 2012; Zeng and He 2016). Gangopadhyay et al. (2019) additionally reported an increase in the frequency of Gulf Stream Warm Core Ring formation since the year 2000. These documented changes in Gulf Stream behavior, which increase the likelihood and frequency of the Gulf Stream directly impacting the Middle Atlantic Bight continental shelf, may have major impacts on regional climate, commercial fisheries, and other societally relevant issues. Together with other components of the observing system, the multi-year, broad-scale sampling by gliders in the Gulf Stream is providing key observations that allow us to understand the current state of the Gulf Stream system and will, if continued, capture future changes to the system. This thesis examines the glider observations to present a detailed overview of the Gulf Stream's structure and mean characteristics, as well as its spatial evolution in terms of volume transport and water properties.

1.4 Observations used in this thesis

The focus of this thesis is primarily on in situ observations collected by autonomous underwater gliders (section 1.4.1). These are complemented by ship-based observations collected along Line W and satellite-based measurements of sea surface height (section 1.4.2).

1.4.1 Glider observations

The Spray glider (Sherman et al. 2001; Rudnick et al. 2016) observations used in this thesis are part of an ongoing multi-year observational program examining the finescale structure and dynamics of the Gulf Stream. The gliders have routinely surveyed the

Gulf Stream between Florida and New England since April 2015 (details in Heiderich and Todd 2020, i.e., Chapter 2). The basic observational goal of this program is to maintain two gliders sampling in or near the Gulf Stream at all times, ideally one upstream and one downstream of Cape Hatteras, to ensure sufficient seasonal coverage. Observations from additional Spray gliders surveys of the Gulf Stream between 2004 and 2009 (Todd et al. 2016) and along the continental margin near Cape Hatteras (Todd 2020) are also included. Summary statistics for all glider missions in this large observational data set can be found in Fig. 1-3.

Spray gliders are buoyancy-driven autonomous underwater vehicles (Davis et al. 2002; Rudnick et al. 2004; Rudnick 2016) that fly through the water column in a sawtooth pattern using volume adjustments and shifting ballast, meaning that the gliders are not equipped with a propeller. Instead, the gliders change their volume while keeping their mass constant by pumping oil from an internal to an external bladder. This changes the buoyancy, which results in vertical displacement that is translated into forward momentum through two wings. During a typical dive cycle (Fig. 1-6), a glider receives a predive GPS fix and any commands and waypoints sent via the Iridium satellite system before descending to a maximum depth of 1000 m at a typical vertical speed of 0.1 m s^{-1}. At maximum depth (or on approach to the bottom in shallower regions), the glider pumps oil into the external bladder, increasing its displacement and allowing it to ascend at a similar vertical speed back to the surface, where it the receives another GPS fix and transmits data to shore. The near-real-time data transmitted via satellite have a lower resolution than the data logged on board, which can be accessed after glider recovery for postprocessing. Throughout the dive, movable battery packs are used to control pitch and roll, enabling horizontal movement relative to the water at about 0.25 m s^{-1} and directional control. A dive to 1000 m usually takes about 6 hours and covers about 5 km horizontally through the water; shallower dives take less time and cover less distance. At the surface, the glider rolls to one side to lift a wing that contains an antenna out of the water; this is the only time to communicate with them from shore via satellite.

Autonomous underwater gliders enable long-duration monitoring of the ocean; a

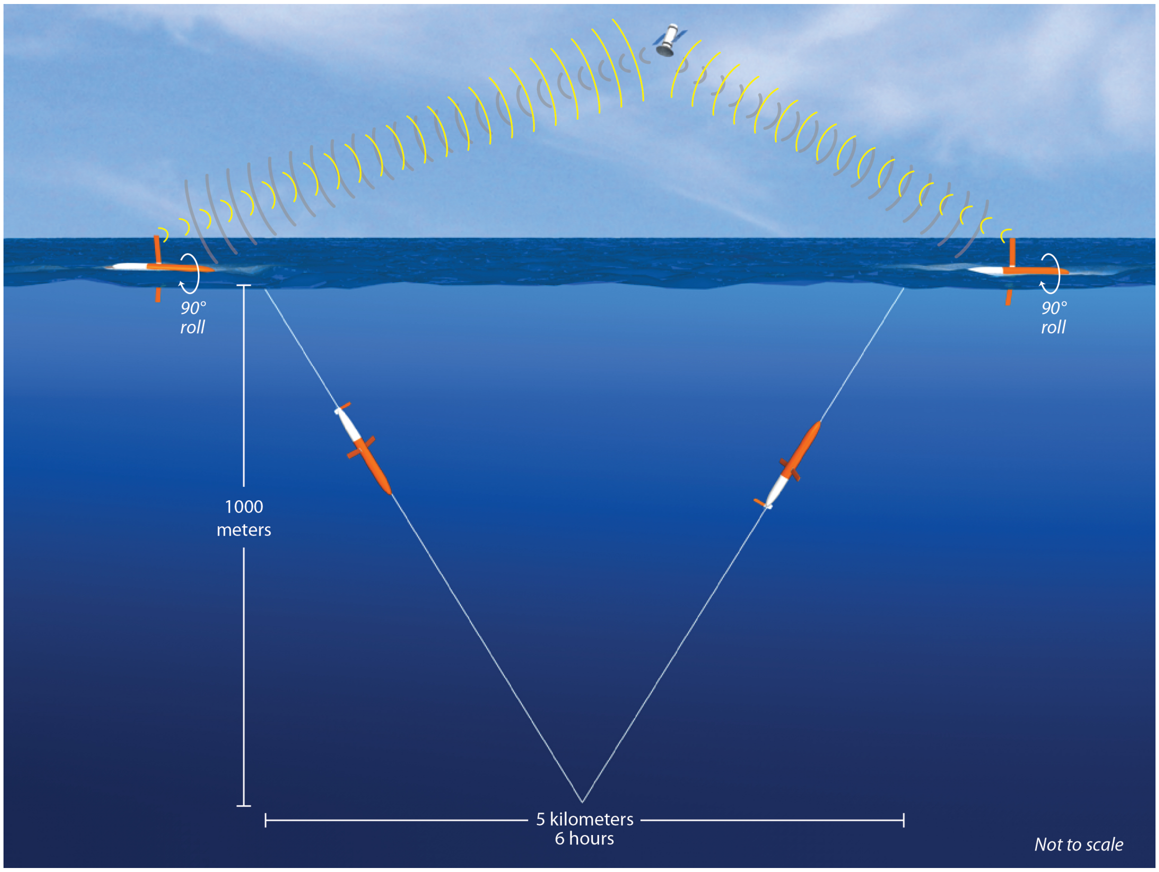

Figure 1-6: Illustration of a Spray glider dive cycle. Image courtesy of Jack Cook, Woods Hole Oceanographic Institution.

typical Spray glider mission in the Gulf Stream lasts approximately 120 days. During this time, a glider deployed from Miami, Florida, crosses the Gulf Stream about 10 times as it is carried downstream toward recovery in Cape Cod, Massachusetts. Glider deployments occur approximately every two months to ensure the observational target of two gliders in the Gulf Stream at a time. Deployment and recovery operations are typically conducted from small vessels during day trips from local ports. The gliders are commanded to fly perpendicular to the measured depth-average currents. Since the depth-average currents in the Gulf Stream often exceed 1 m s^{-1}, the gliders are advected downstream and cross the Gulf Stream obliquely, typically at angles of 25° – 40° to the left or the right of the flow. A variety of shark attacks, mechanical failures, and instrument failures have shortened some glider missions.

Each Spray glider measures temperature, salinity, and pressure using a pumped

Figure 1-7: Local streamwise coordinate system used for the analysis of glider data. The measured vertically averaged current (dark blue) at each dive defines the downstream direction y, which is oriented at an angle ϕ counterclockwise from east. R, the radius of curvature of the flow (light blue), can be estimated from the dive-to-dive change in orientation of the flow. Figure from Todd et al. (2016).

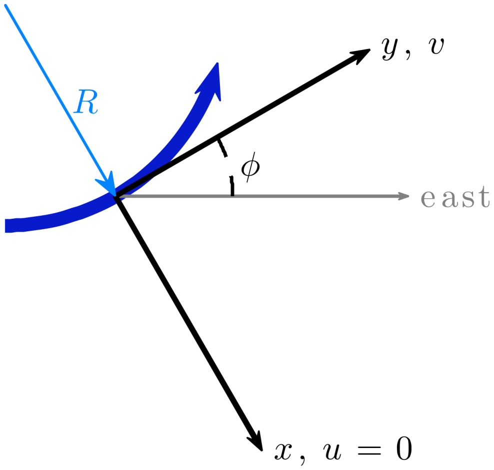

Sea-Bird Scientific 41CP conductivity-temperature-depth (CTD) instrument. The difference between GPS-measured and dead-reckoned displacements provides an estimate of depth-average current velocities as described in Rudnick et al. (2018). Gliders deployed since July 2015 have also been equipped with 1-MHz Nortek acoustic Doppler dual current profilers (AD2CPs) and Seapoint chlorophyll fluorometers. Since October 2018, some gliders have also been outfitted with Sea-Bird 63 dissolved oxygen sensors. An inverse method is used to estimate absolute horizontal velocity profiles by combining relative velocity measurements from the AD2CPs with the depth-average current estimates (Visbeck 2002; Todd et al. 2011, 2017). The AD2CP also functions as an altimeter during the descent to avoid collision with the seafloor and provides an in situ measurement of bottom depth. All properties are measured during the ascending portion of a glider dive to present an undisturbed profile to the upwards-oriented CTD sensor. For analyses herein, all profiles are processed to have uniform 10-m vertical resolution. Summary statistics for the subsets of glider observations used in the analyses herein are given in the individual chapters. Further details of the data processing, quality control, and selection of cross–Gulf Stream transects can be found in Heiderich and Todd (2020), i.e., Chapter 2.

Cross–Gulf Stream glider transects are presented in a local streamwise coordinate system following the method described in Todd et al. (2016). In a coordinate system moving with the water, the gliders cross the Gulf Stream at approximately right angles. For each individual glider dive, we define the downstream direction y based on the measured depth-averaged current, which is oriented at an angle ϕ counterclockwise from east (Fig. 1-7). The decomposition of the glider displacement during each dive into cross-stream (Δx) and along-stream components (Δy) allows us to quantify the change in current direction along a transect. Summing the cross-stream displacements during a transect results in a new horizontal coordinate, cross-stream distance (e.g., Fig. 2-3). Following Todd et al. (2016), we define the origin of this coordinate system to be the location where the 15°C isotherm is found at a depth of 200 m, a metric that has long been used to define the position of the Gulf Stream's North Wall (e.g., Fuglister and Voorhis 1965).

1.4.2 Other data sets

We use satellite-based estimates of absolute dynamic topography (ADT) to create an along-stream coordinate system for the Gulf Stream (Chapters 2–4) and to compare how well satellite altimetry captures the variability in Gulf Stream transport that is measured by the gliders (Chapter 4). ADT describes the sea surface height with respect to the geoid, which is itself the shape that the sea surface would take due to gravity and Earth's rotation alone (i.e., without the influence of winds, tides, or currents). ADT is derived from satellite altimetry in the following way: Altimetry measures the instantaneous sea surface height (SSH) above a reference ellipsoid, an arbitrary surface that roughly approximates the shape of the Earth. From SSH, sea level anomalies (SLA) can be derived by subtracting a multi-year mean sea surface (MSS). Subtracting the geoid from the temporal mean of SSH (MSS) gives mean dynamic topography (MDT). Finally, absolute dynamic topography is obtained by adding the sea level anomalies (SLA) to the estimated mean dynamics topography (MDT). The specific details of the ADT product used in this thesis and its limitations are described in more detail in Chapters 2 and 4.

In Chapter 2, ship-based observations collected along Line W (Toole et al. 2011; Andres et al. 2020) are used to augment the in situ observational glider coverage downstream of Cape Hatteras. Gliders had lower sampling density in this region due to some missions ending prematurely. The ship-based sampling using CTDs and lowered ADCPs (LADCPs) provides concurrent measurements of water properties and velocities that can be treated similarly to the glider observations.

1.5 Thesis overview

This thesis contains three different studies that explore the along-stream evolution of the Gulf Stream using a combination of underwater glider measurements and other observational data sets. The question at the center of all of these studies is: "How much water does the Gulf Stream carry, and what are the characteristics of that water?" Though this is an age-old question that many previous studies have addressed (see Sec. 1.2), the large glider data set allows us to address it in much more detail than was previously possible. Each of the three studies examines different aspects of the along-stream evolution of volume transport and water properties in the Gulf Stream:

- Chapter 2 characterizes the along-stream evolution of volume transport in the Gulf Stream between Florida and New England, including examination of the constituent water properties.
- Chapter 3 investigates the processes, including lateral stirring and vertical mixing, that contribute to an observed along-stream reduction in the volume transport of Antarctic Intermediate Water as the Gulf Stream flows between Florida and the Carolinas. Furthermore, the mechanisms leading to the observed entrainment of upper Labrador Sea Water into the Gulf Stream far south of Cape Hatteras are examined.
- Chapter 4 explores how well satellite altimetry estimates of sea surface height capture the variability in Gulf Stream transport observed by gliders.

The results in these three studies are summarized in Chapter 5, followed by a discussion of their implications and possible directions for future research.

Chapter 2

Along-stream evolution of Gulf Stream volume transport

This chapter was originally published as: Heiderich, J., and R. E. Todd, 2020: Along-Stream Evolution of Gulf Stream Volume Transport. *Journal of Physical Oceanography*, **50 (8)**, 2251 – 2270, doi: 10.1175/JPO-D-19-0303.1. © American Meteorological Society. Used with permission.

Abstract

The Gulf Stream affects global climate by transporting water and heat poleward. The current's volume transport increases markedly along the U.S. East Coast. An extensive observing program using autonomous underwater gliders provides finescale, subsurface observations of hydrography and velocity spanning more than 15° of latitude along the path of the Gulf Stream, thereby filling a 1500-km-long gap between long-term transport measurements in the Florida Strait and downstream of Cape Hatteras. Here, the glider-based observations are combined with shipboard measurements along Line W near 68°W to provide a detailed picture of the along-stream transport increase. To account for the influences of Gulf Stream curvature and adjacent circulation (e.g., corotating eddies) on transport estimates, upper and lower bound transports are constructed for each cross–Gulf Stream transect. The upper bound estimate for time-averaged volume transport above 1000 m is 32.9 ± 1.2 Sv (1 Sv $\equiv 10^6$ m^3 s^{-1}) in the Florida Strait, 57.3 ± 1.9 Sv at Cape Hatteras, and 75.6 ± 4.7 Sv at Line W. Corresponding lower bound estimates are 32.3 ± 1.1 Sv in the Florida Strait, 54.5 ± 1.7 Sv at Cape Hatteras, and 69.9 ± 4.2 Sv at Line W. Using the temperature and salinity observations from gliders and Line W, waters are divided into seven classes to investigate the properties of waters that are transported by and entrained into the Gulf Stream. Most of the increase in overall Gulf Stream volume transport above 1000 m stems from the entrainment of subthermocline waters, including upper Labrador Sea Water and Eighteen Degree Water.

2.1 Introduction

The Gulf Stream is the subtropical western boundary current of the North Atlantic and thus redistributes heat, salt, and carbon in the global climate system (Wunsch 2005; Schmittner and Galbraith 2008; Kwon et al. 2010). As a principal component of the upper limb of the Atlantic meridional overturning circulation, the Gulf Stream contributes significantly to poleward heat and volume transport (Cunningham et al. 2007). This strong, narrow current carries warm, saline waters from the tropics to higher latitudes, thereby balancing equatorward transport in the ocean interior, including both wind-driven equatorward transport in the upper ocean (Sverdrup 1947; Stommel 1948; Munk 1950) and equatorward thermohaline flow at depth (Stommel and Arons 1959; Wunsch and Roemmich 1985).

The Gulf Stream flows along the U.S. East Coast before separating from the continental margin near Cape Hatteras, North Carolina, encountering different dynamical regimes on its way north. The current transitions from a strong, relatively straight jet in the confined channel of the Florida Strait (FS) to a topographically stabilized jet along a boundary in the South Atlantic Bight (SAB) upstream of Cape Hatteras, and finally to a free, meandering, eddy-shedding jet downstream of Cape Hatteras in the Middle Atlantic Bight (MAB) and farther downstream. Gulf Stream structure and transport evolve markedly across these differing dynamical regimes (e.g., Meinen and Luther 2016). It has long been known that Gulf Stream volume transport increases in the downstream direction (Knauss 1969); transport approximately triples between the Florida Strait and the open North Atlantic downstream of Cape Hatteras (Leaman et al. 1989). Estimated full-depth transport increases from about 32 Sv (1 Sv $\equiv 10^6$ m^3 s^{-1}) in the Florida Strait (Meinen et al. 2010), to about 94 Sv near Cape Hatteras (Leaman et al. 1989), and to at least 150 Sv near 60°W (Hogg 1992). Meanders north of Cape Hatteras generally grow in the downstream direction (Watts and Johns 1982), although a local minimum in meander amplitude is found between the CMV *Oleander* survey line near 70°W and Line W near 68°W (Cornillon 1986; Joyce et al. 2000; Andres et al. 2020).

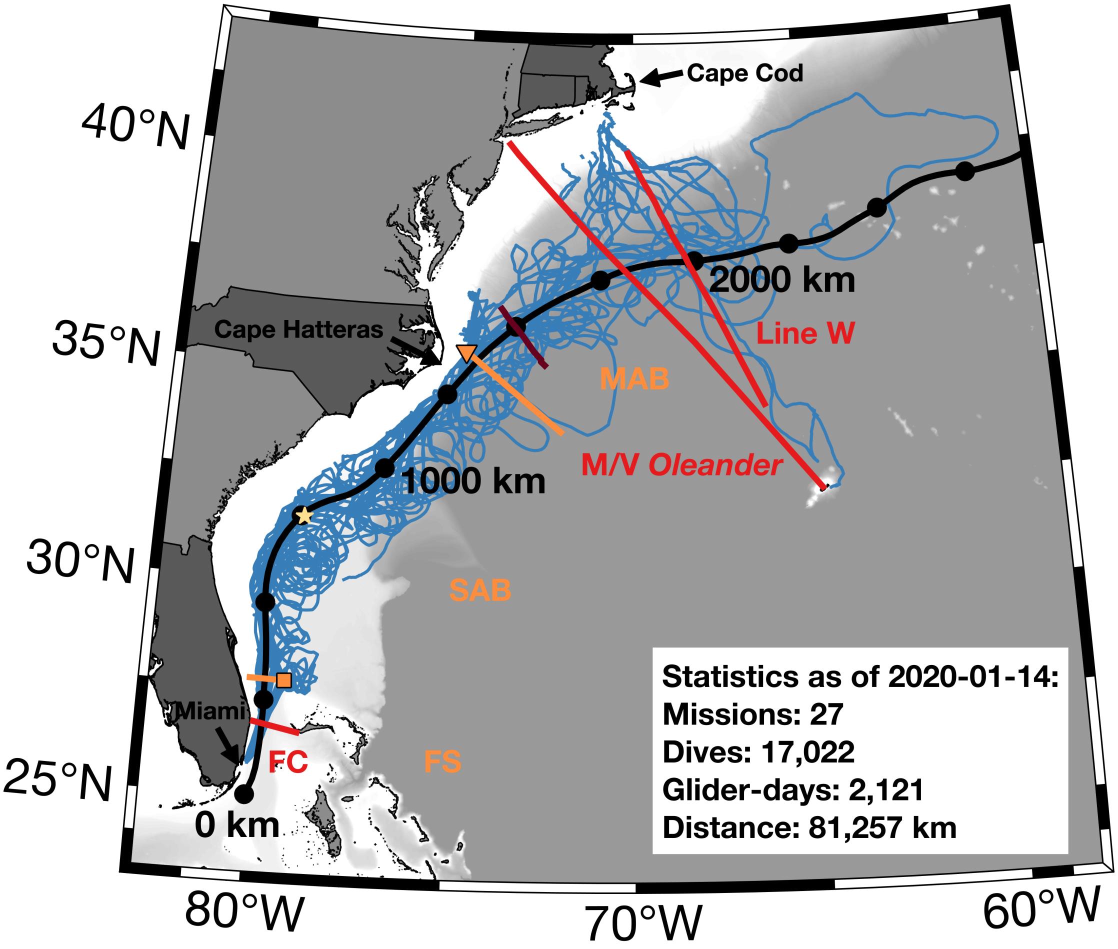

Figure 2-1: Trajectories of Spray glider missions in the Gulf Stream (blue). Locations of sustained in situ Gulf Stream observations from other programs (red): the Florida Cable (FC) a part of the Western Boundary Time Series; the *Oleander* line; and Line W. The mean 40-cm SSH contour averaged over 16 calendar years (1 January 2004–31 December 2019) represents the mean Gulf Stream position and provides an along-stream coordinate system (black with dots every 250 km). Orange lines delineate different dynamical regions: the Florida Strait (FS), South Atlantic Bight (SAB), and Middle Atlantic Bight (MAB). The orange triangle indicates the location of "The Point" near Cape Hatteras, and the orange square shows the northwesternmost point of Little Bahama Bank at the 500-m isobath. The yellow star denotes the location of the Charleston Bump. The PEGASUS line near 73°W is shown in maroon. From south to north, Florida, North Carolina, and the New England states are highlighted in dark gray, and important locations are indicated with arrows. Glider mission statistics are displayed in the lower right.

Many observational campaigns have focused on capturing Gulf Stream dynamics at fixed stations or with repeat ship-based transects. A variety of Gulf Stream transport estimates have been produced from observational efforts at certain positions along the Gulf Stream's path and with relatively short temporal extent (e.g., Halkin and Rossby 1985; Hall and Bryden 1985; Leaman et al. 1989; Hogg 1992; Johns et al. 1995). Measurements of Gulf Stream transport spanning a decade or longer are only available for three locations in the Gulf Stream: at the Florida Cable (FC) in the Florida Strait since 1982 (Baringer and Larsen 2001; Shoosmith et al. 2005; Meinen et al. 2010), along the *Oleander* line since 1992 (Flagg et al. 2006; Andres et al. 2020), and at Line W from 2004 to 2014 (Toole et al. 2011, 2017; Andres et al. 2020). These long-term observations are separated by more than 1500 km in the along-stream direction (Fig. 2-1) and thus do not resolve the space–time evolution of Gulf Stream transport across the varying dynamical regimes along the U.S. East Coast.

Gulf Stream transport variability may not be correlated between different dynamical regions; Sanchez-Franks et al. (2014) found that volume transport in the Florida Strait is uncorrelated with transport downstream of Cape Hatteras. This lack of correlation indicates varying entrainment along the Gulf Stream's path and points to the importance of recirculation gyres (e.g., Johns et al. 1995; Andres et al. 2020). Large, eddy-driven recirculations at depth exist both north (Richardson 1985; Hogg 1992) and south (Worthington 1976) of the Gulf Stream, contributing 20–40 Sv to the total transport (Hogg et al. 1986; Johns et al. 1995). Smaller upper-ocean recirculation cells have also been observed just downstream of the Gulf Stream's separation point at Cape Hatteras (Csanady and Hamilton 1988; Andres et al. 2020). The Antilles Current, which joins the Gulf Stream just north of the Bahamas, is another highly variable source of waters that are entrained into the Gulf Stream (Meinen et al. 2019).

Studies at isolated locations along the U.S. East Coast reveal differences in the properties of waters constituting the Gulf Stream. Meinen and Luther (2016) noted distinct upper and lower layers in the Florida Strait and three distinguishable layers downstream of Cape Hatteras when comparing full-depth observations from both locations. Farther downstream, at 42°N near the Southeast Newfoundland Ridge, the Gulf Stream structure returns to two distinguishable layers (Meinen and Luther 2016). Among the water masses advected and modified within the Gulf Stream are intermediate waters, including Antarctic Intermediate Water and Labrador Sea Water. Labrador Sea Water is formed through deep convection in the Labrador Sea and is transported southward in the uppermost layer of the Deep Western Boundary Current (DWBC; Le Bras et al. 2017). The shallowest component of Labrador Sea Water, often called upper Labrador Sea Water, is prone to interactions with the Gulf Stream when the DWBC encounters the Gulf Stream near Cape Hatteras (Pickart and Smethie 1993; Spall 1996a; Bower and Hunt 2000a). AAIW is formed remotely at high southern latitudes and reaches the Gulf Stream through the Florida Strait. Szuts and Meinen (2017) classified the volume transport through the Florida Strait based on water masses, but the along-stream evolution of water mass transport and the details of the varying inputs to total Gulf Stream transport remain unknown downstream of the Florida Strait.

Due to the large gradients and relatively small horizontal scales of the Gulf Stream, concurrent, high-resolution observations of hydrography and velocity are necessary to examine how different water masses contribute to total Gulf Stream transport. In the Gulf Stream along the U.S. East Coast, an extensive field program using autonomous underwater gliders (Todd et al. 2016; Todd 2017; Todd and Locke-Wynn 2017; Todd et al. 2018) provides routine, finescale, subsurface measurements of hydrography and velocity over more than 15° of latitude. These observations provide a detailed picture of the upper kilometer of the Gulf Stream's structure and fill the gap between long-term measurements in the Florida Strait and downstream of Cape Hatteras (Fig. 2-1).

Here we examine the along-stream evolution of Gulf Stream volume transport across different dynamical regimes along the U.S. East Coast. The transport estimates presented here are derived from a combination of glider-based observations and shipboard measurements along Line W that are described in section 2.2. Section 2.3.1 explains how we estimate volume transport from the observations, then discusses the along-stream increase in total volume transport with comparisons to previous studies. Section 2.3.2 focuses on the contributions of waters with various properties to Gulf

Stream transport. Section 2.4 summarizes the results and implications.

2.2 Observations

2.2.1 Glider missions

Spray autonomous underwater gliders (Sherman et al. 2001; Rudnick et al. 2016) have repeatedly surveyed the Gulf Stream along the U.S. East Coast over the course of 27 missions since 2004 (Fig. 2-1). Between 2004 and 2009, four missions sampled exclusively downstream of Cape Hatteras (details in Todd et al. 2016). Since 2015, 23 missions have sampled along the U.S. East Coast between Miami, Florida, and New England. For the ongoing sampling program, gliders are deployed offshore of Miami near 25°45′N, 80°W approximately every two months (Fig. 2-2a) to ensure sufficient seasonal coverage (Fig. 2-2b). During a typical 120-day mission, a glider crosses the Gulf Stream approximately 10 times between the Florida Strait and the continental shelf south of Cape Cod, Massachusetts, while profiling along a sawtooth path through the water column. Since June 2018, gliders have had clearance to enter Bahamian waters, allowing occupation of complete transects across the Florida Strait. Some missions ended early due to shark attacks and instrument failures, leading to reduced observation density downstream of Cape Hatteras (Fig. 2-2). This analysis uses observations from Gulf Stream glider missions completed through January 2020; summary mission statistics are included in Fig. 2-1.

The horizontal speed of the gliders through the water is approximately 0.25 m s^{-1}, but depth-average Gulf Stream speeds often exceed 1 m s^{-1}. The gliders are thus advected downstream while they steer perpendicular to the observed depth-average currents. Resulting trajectories over the ground are typically oriented at angles of 25°–40° to the left or right of the local flow while crossing the Gulf Stream (Fig. 2-1; Todd et al. 2016). Gliders are often commanded to loop upstream on the flanks of the Gulf Stream to achieve denser along-stream resolution.

Each glider carried a pumped Sea-Bird 41CP CTD to measure temperature, salin-

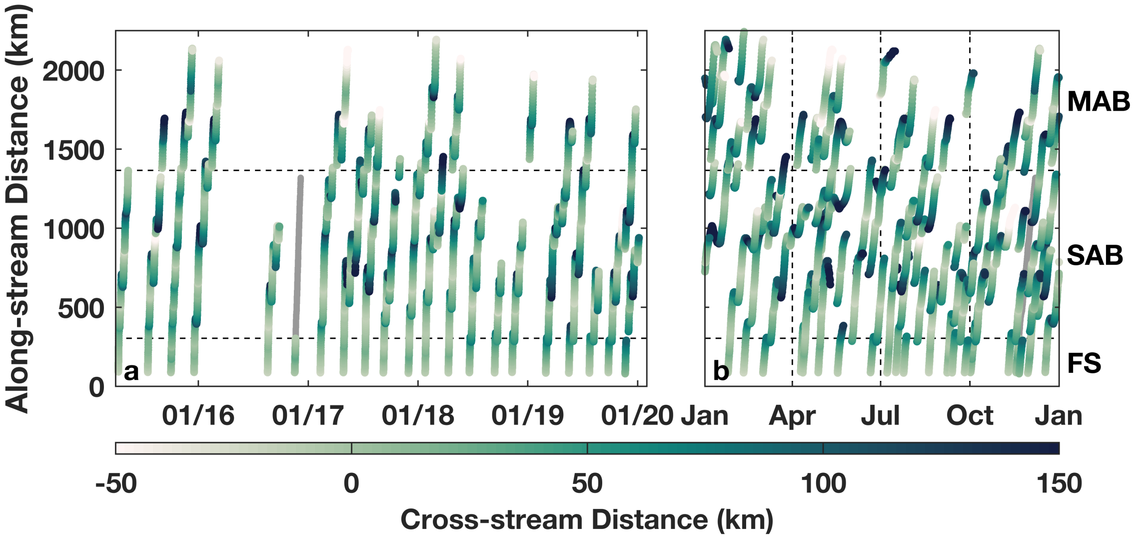

Figure 2-2: Spray glider sampling in the Gulf Stream as a function of along-stream distance from 25°N and time. (a) Sampling from Apr 2015 through Jan 2020. (b) All sampling since 2004 as a function of time of year instead of measurement date. Vertical and horizontal dashed lines delineate seasons and dynamical regions (FS, SAB, MAB), respectively. Points are colored by cross-stream position relative to where the 15°C isotherm is found at a depth of 200 m, except for part of one glider mission in late 2016 when the CTD failed (gray).

ity, and pressure. We estimate depth-average current velocities $\mathbf{v}_{\mathrm{DA}}$ based on the difference between dead-reckoned and GPS-measured glider displacements (Rudnick et al. 2018). For the 22 missions since July 2015, the gliders have also been equipped with 1-MHz Nortek acoustic Doppler dual current profilers (AD2CPs) and Seapoint chlorophyll fluorometers. Some gliders began carrying Sea-Bird 63 dissolved oxygen sensors in October 2018. Chlorophyll and oxygen measurements are not discussed further here. We estimate absolute horizontal velocity profiles by combining the velocity shear measured by the AD2CPs with estimates of depth-average currents and surface drift velocities using an inverse method (Todd et al. 2017). The AD2CPs also function as altimeters and are used to avoid collisions with the seafloor during the descending phase of each glider dive. Profiles at nominal vertical speeds of 0.1 m s^{-1} reach to maximum depths of 1000 m or to within a few meters of the seafloor when the bottom is shallower than a kilometer. All quantities are measured during the ascending phase of each glider dive. Cross-Gulf Stream transects usually have a

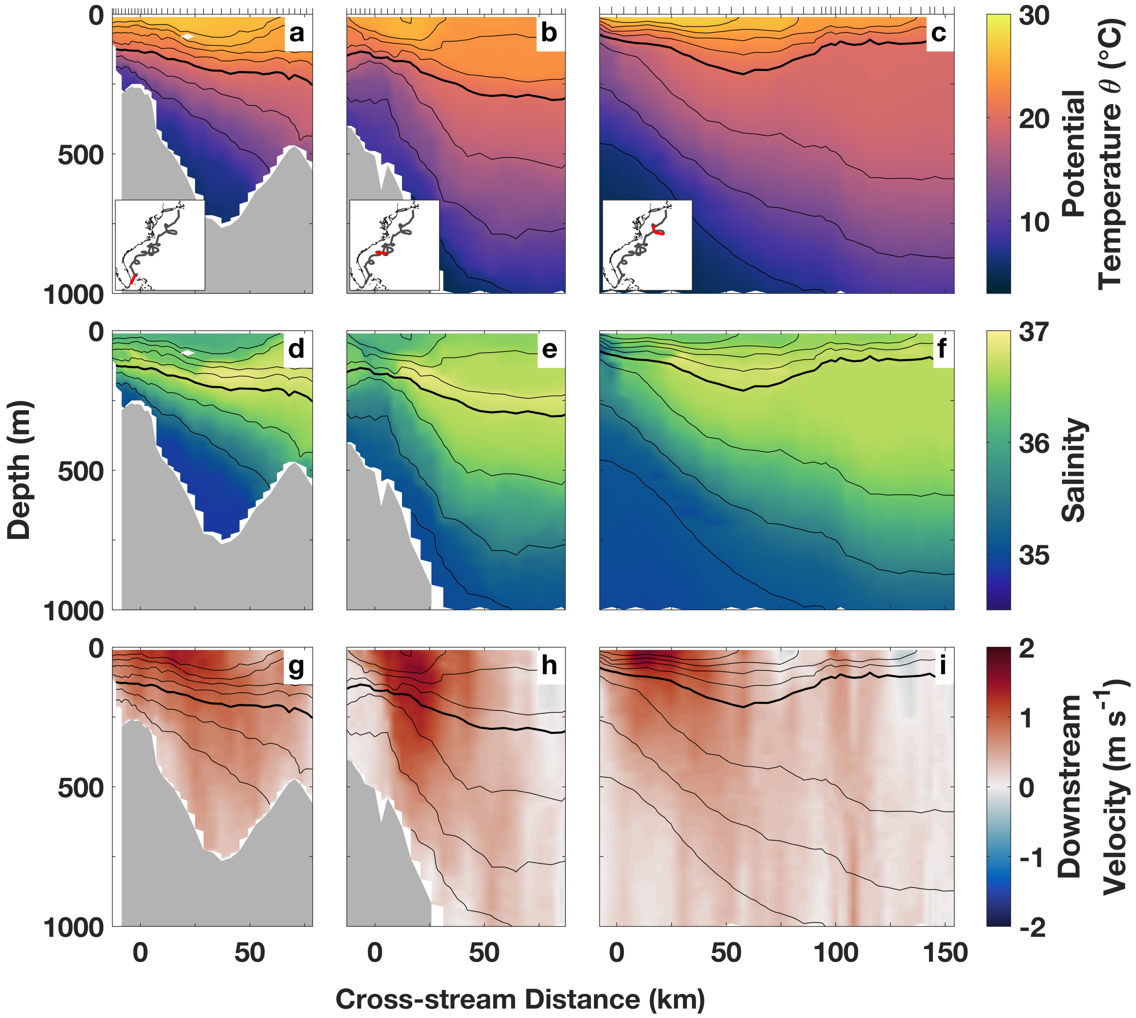

Figure 2-3: Example Spray glider transects across the Gulf Stream during spring 2019: (a)–(c) potential temperature θ, (d)–(f) salinity, and (g)–(i) downstream velocity (i.e., velocity parallel to the measured depth-average current). Black contours are isopycnals with a spacing of 0.5 kg m^{-3} and the 26.0 kg m^{-3} isopycnal bold. Tick marks on the upper axes indicate the locations of individual profiles. The bathymetry as measured by the glider's AD2CP is shaded gray. From left to right, transects are representative of the FS, SAB, and MAB dynamical regions. Inset maps in (a)–(c) show the location of each transect in red in relation to the complete mission trajectory (gray).

cross-stream resolution of 5 km or finer (e.g., Fig. 2-3).

Glider observations are automatically and manually quality-controlled using established postprocessing routines for Spray gliders (e.g., Rudnick et al. 2017, 2018). We ensure that accurate predive and postdive locations and times are available for each dive and adjust the heading records for each dive using heading-dependent compass calibrations and local magnetic variations. CTD profiles are examined visually and quality flags are assigned manually; usable data are then averaged into 10-m vertical bins for subsequent analyses. Raw AD2CP data are processed as described in Todd et al. (2017) to produce 10-m-resolution profiles of absolute horizontal velocity with two key changes that serve to admit more data into the velocity calculation. First, we increase the maximum velocity accepted as good from 0.5 to 5 m s^{-1} to avoid filtering out good data in regions of large shear (mainly around the thermocline). Second, we reduce the signal-to-noise ratio (SNR) below which measurements are excluded from 20 to 1. For two missions, loss of instruments before recovery led to no raw AD2CP data being available for quality control of individual samples; only the shear profiles processed on board the gliders and transmitted in near–real time via the Iridium satellite network are available for those missions.

The accuracy of the transport estimates that follow depends in part on the accuracy of individual velocity estimates. Velocity profiles are constrained by both the depth-average velocity estimates and estimates of surface velocity from glider drift during communications (Todd et al. 2017). Depth-average velocity estimates have root-mean-square errors (RMSEs) of about 0.01 m s^{-1} and insignificant bias (Rudnick et al. 2018). Surface velocity estimates have accuracies of about 0.05 m s^{-1} (Todd et al. 2017). To estimate additional errors in depth-dependent velocities derived from AD2CP measurements, we follow Todd et al. (2017) and consider the profiles of velocity variance for each glider mission with an AD2CP (Fig. 2-4a). A velocity variance profile in the ocean is expected to have high variance near the surface due to upper ocean variability and to generally decrease with depth. However, the glider-based variance profiles often exhibit a minimum at middepth. The increase in variance below this middepth minimum in the glider velocity solutions is attributed to random

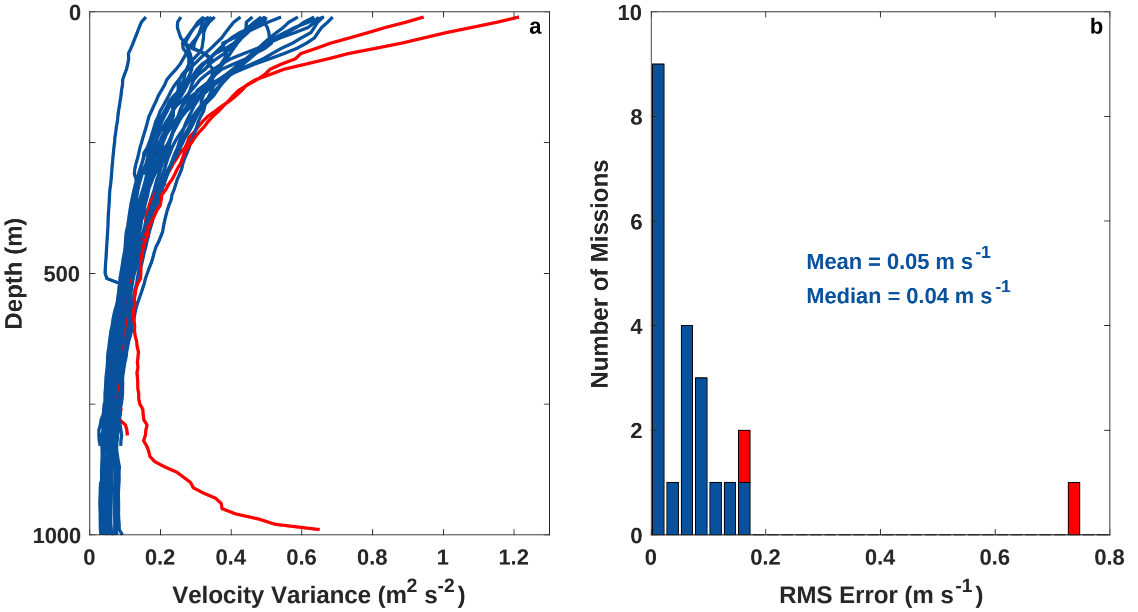

Figure 2-4: (a) Vertical profiles of velocity variance for the 22 Gulf Stream glider missions with AD2CPs from the surface to the maximum depth for which at least 40 dives contribute to the variance. Red indicates missions where raw data are not available due to instrument losses. (b) Histogram of the root-mean-square error (RMSE) in velocity profiles for all Gulf Stream missions shown in (a). The mean and median RMSEs for missions with raw data are shown. Color coding is as in (a).

errors (e.g., due to reduced acoustic scatterers at depth). We estimate the root-mean-square error associated with the depth-dependent velocity profiles from a mission as the square root of the difference between the minimum variance and the maximum variance below the depth of minimum variance. Here, the variance profiles taken into account extend down to the maximum depth sampled during at least 40 glider dives over the course of each mission. For 9 of 22 missions, minimum variance is at the bottom of the profile. The two updates to AD2CP processing since Todd et al. (2017) (i.e., reduction of SNR ratio and increase of maximum velocity accepted as good) admit more data into the estimate, thereby reducing profile-to-profile variability, especially at depth. Increases in velocity variance at depth and resulting estimates of root-mean-square errors in depth-dependent velocity are reduced from the 0.24 m s^{-1} estimate for a Gulf Stream mission in Todd et al. (2017) to less than 0.18 m s^{-1} for all missions with raw AD2CP data available (Fig. 2-4b, blue). The two missions without raw AD2CP data exhibit higher variance and consequently higher root-mean-square errors (Fig. 2-4, red). One mission had very low variance at the surface due to many shallow dives over the continental shelf. For missions with raw AD2CP data available, the mean error associated with the depth-dependent, AD2CP-derived velocity profiles is 0.05 m s^{-1} and the median is 0.04 m s^{-1}. Considering these various sources contributing depth-dependent and absolute errors, we will assume that 0.1 m s^{-1} is an appropriate typical value for the error in individual glider-based absolute velocity profiles in the transport estimates that follow.

For the five missions without AD2CPs, depth-dependent, cross-transect velocities are estimated from geostrophic shear referenced to the cross-track component of the depth-average current following Todd et al. (2011). We use an objective mapping routine with a 50-km Gaussian length scale (Bretherton et al. 1976) to filter signals with periods shorter than a day, such as internal waves and tides (Rudnick and Cole 2011; Todd et al. 2011), when estimating along-track density gradients at the original profile locations. Temperature and salinity for these transects are mapped similarly. We mask objectively mapped fields where the normalized mean square error of the objective map exceeds 0.1. Despite difficulties near the edges of transects due to the along-track scale of the mapping, comparisons of AD2CP-based and geostrophic velocity estimates for missions with AD2CPs give us confidence that transport estimates derived from geostrophic velocities are useful for analysis.

2.2.2 Line W observations

To supplement the glider observations, we use ship-based CTD and lowered ADCP (LADCP) measurements from 13 cruises along Line W. These observations help to constrain transport estimates in a region of reduced glider sampling downstream of Cape Hatteras (Fig. 2-2). Between November 1994 and May 2014, repeated cruises provided simultaneous full-depth observations of hydrographic properties and current velocities along Line W (Fig. 2-1; Toole et al. 2011; Andres et al. 2020). For our analysis, we require that the ship transects crossed the entire Gulf Stream and did not have large sampling gaps within the current. This leaves us with cruise data from

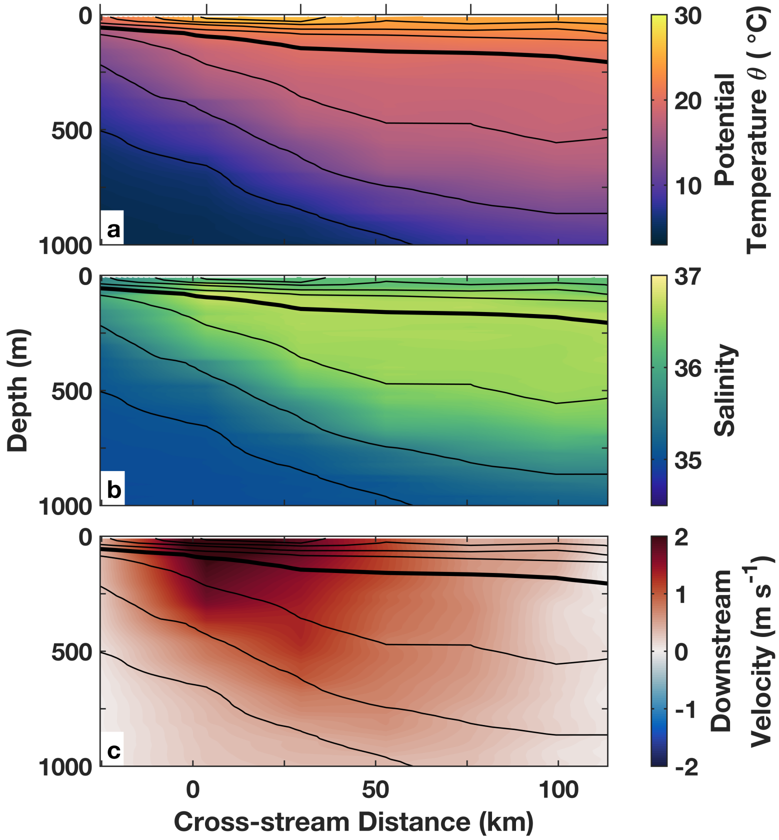

Figure 2-5: Example transects of (a) potential temperature θ, (b) salinity, and (c) downstream velocity in the upper 1000 m from Line W ship-based measurements in May 2013. Tick marks on the upper axes indicate the position of individual CTD/LADCP stations. Isopycnals are as in Fig. 2-3.

the following times: 2003 (November), 2004 (May and September), 2005 (April), 2006 (October), 2007 (April and October), 2008 (May), 2009 (September), 2010 (October), 2011 (July), 2012 (August), 2013 (May). The Line W transects are of lower horizontal resolution than the glider transects, with station spacing of about 30 km in the Gulf Stream (e.g., Fig. 2-5). In order to treat Line W transects in a manner analogous to the glider transects, we interpolate the Line W data in the upper kilometer to the glider depths and calculate the depth-average current as the mean LADCP-based velocity in the upper 1000 m. As in Andres et al. (2020), near-surface gaps in LADCP profiles are filled with the shallowest valid measurement. Toole et al. (2011) report uncertainties of 0.02–0.05 m s^{-1} in the LADCP velocities at Line W, comparable to the error estimates for glider-based velocities.

2.2.3 Sea surface height

Satellite-based observations of sea surface height (SSH) provide spatially broad context for the in situ observations from gliders and Line W. We use the absolute dynamic topography provided by the EU Copernicus Marine Environment Monitoring Service. Daily delayed-time products are available until 13 May 2019. Near-real-time products are used for more recent times.

2.3 Results and discussion

2.3.1 Transport estimates

Our goal is to characterize the time-mean spatial evolution of Gulf Stream volume transport above 1000 m along the U.S. East Coast using the observations from both Spray gliders and Line W. To estimate transport from this collection of cross–Gulf Stream transects we must overcome several challenges, including defining "Gulf Stream transport" and estimating the associated transport errors. In this section, we first describe how we identify cross–Gulf Stream transects (section 2.3.1.1), then we construct upper and lower bound estimates of Gulf Stream transport in order to characterize errors in transport estimates (section 2.3.1.2), and finally we discuss the along-stream evolution of the volume transport (section 2.3.1.3).

2.3.1.1 Transect identification and along-stream coordinate system

Our Gulf Stream transport estimates are based on estimates of transport through individual cross–Gulf Stream transects occupied by gliders throughout the domain or by a ship along Line W. Identifying discrete cross-Gulf Stream transects is the first step in our analysis. Operationally, a glider's cross-stream direction relative to the Gulf Stream is changed when the glider reaches the 100-m isobath or when depth-average currents reverse direction, allowing for navigation upstream relative to the Gulf Stream (e.g., looping glider tracks in Fig. 2-1). These piloting choices define initial endpoints for individual glider-based transects. For the shipboard observations

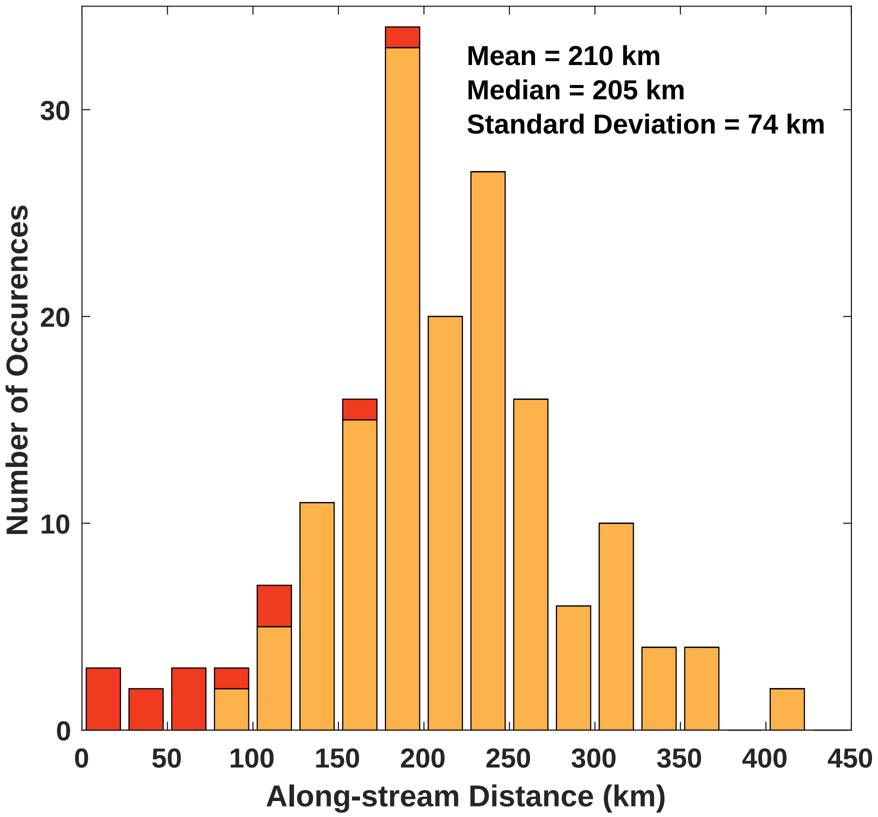

Figure 2-6: Histogram of the along-stream distances covered during all glider (orange) and Line W (red) transects that are used for transport calculations. The mean, median, and standard deviation of along-stream extent are given in the upper-right corner.

along Line W, initial transects comprise all profiles from a given cruise. To refine the individual transects from both platforms, we further require that each transect proceeds monotonically in the cross-stream direction defined by the local upper-1000-m depth-average current. The only exceptions are isolated midtransect glider dives that proceed in the opposite direction due to piloting mishaps. Transects are also visually inspected (in conjunction with contemporaneous SSH) to ensure that they cross the entirety of the Gulf Stream and to exclude adjacent non-Gulf Stream features.

Among the glider transects excluded from this analysis are those that only crossed part of the Florida Strait prior to receipt of Bahamian clearance and those south of New England that were cut short near the ends of the missions due to limits on mission endurance. Furthermore, one glider mission starting in November 2016 is excluded entirely due to a CTD failure before completion of a full Gulf Stream crossing. In total, 155 glider transects and 13 Line W transects are used for transport estimates. Of the glider transects, 142 have AD2CP-based velocity estimates and 13 only have geostrophic velocity estimates.

Following Todd et al. (2016), a local streamwise coordinate system is constructed for each glider and Line W transect with the cross-stream origin located where the 15°C isotherm is found at a depth of 200 m, a common definition of the Gulf Stream's North Wall (Fuglister and Voorhis 1965). The along-stream extent of each transect is computed as the sum of the along-stream displacements relative to the depth-average current during each dive in a transect. The typical along-stream extent of a glider-based cross–Gulf Stream transect is about 200 km (orange bars in Fig. 2-6). The along-stream extent of Line W transects is often much shorter (red bars in Fig. 2-6) because Line W is oriented approximately perpendicularly to the Gulf Stream in most cases. The mean along-stream extent across all transects is 210 km, the median is 205 km, and the standard deviation is 74 km.

We define an along-stream coordinate system based on the 40-cm SSH contour averaged over 16 calendar years that cover almost the entire observation period (1 January 2004–31 December 2019). The long-term mean position of the 40-cm SSH contour is treated as a representative streamline that traces the Gulf Stream continuously from Florida to beyond Cape Hatteras (Fig. 2-1). Other SSH contours that are frequently used to track the Gulf Stream [e.g., the 25-cm SSH contour in Lillibridge and Mariano (2013) and Andres (2016)] are not continuous over the entire glider sampling domain. The intersection of the 40-cm SSH contour with 25°N, a point in the Florida Strait close to the typical launch site for gliders, is taken as the origin of our along-stream coordinate system. Projecting the midpoint of a transect onto the along-stream coordinate system gives a measure of the approximate along-stream position of each Gulf Stream transect, though it should be reiterated that glider-based transects typically have along-stream extents of 200 km. The along-stream distances of other important geographic locations and transport measurement sites

(Fig. 2-1) are defined as the intersection with the along-stream coordinate system for lines (e.g., the Florida Cable, the PEGASUS line near 73°W, the *Oleander* line, and Line W) or the projection onto the along-stream coordinate system for points [e.g., the Charleston Bump (CB), a ridge and trough feature in the continental slope near 31°30′N, 79°W indicated as a yellow star in Fig. 2-1]. To distinguish the different geographical regions (FS, SAB, MAB), we project the northwestern-most tip of the Little Bahama Bank at the 500-m isobath (27°41′N, 79°14′W, orange square in Fig. 2-1) and "The Point" at Cape Hatteras (CH; 35°33′N, 74°48′W, orange triangle in Fig. 2-1) onto the along-stream coordinate system. The resulting along-stream distances of those two locations are 304 km and 1366 km, respectively. Transects with along-stream distances smaller than that of the Little Bahama Bank are considered Florida Strait transects (10 transects used in the transport calculations). Transects with along-stream distances larger than that of the Little Bahama Bank and smaller than that of The Point are considered SAB transects (111 transects). The rest are MAB transects (47 transects). The along-stream extent of glider transects creates ambiguity in their positioning, particularly in classification between geographic regions; for example, initial transects from Miami sometimes extend north of the Little Bahama Bank and capture flow of the Antilles Current that joins the Gulf Stream downstream of the Florida Strait, yet the midpoint of the transect is within the Florida Strait. The impact of this ambiguity is reduced by averaging transport estimates from many transects in section 2.3.1.3.

2.3.1.2 Gulf Stream transport calculations

The Gulf Stream volume transport T through any given cross-Gulf Stream transect is defined as the area integral of the velocity $v_\perp$ that is perpendicular to the transect

$$T = \iint_A v_\perp dA, \tag{2.1}$$

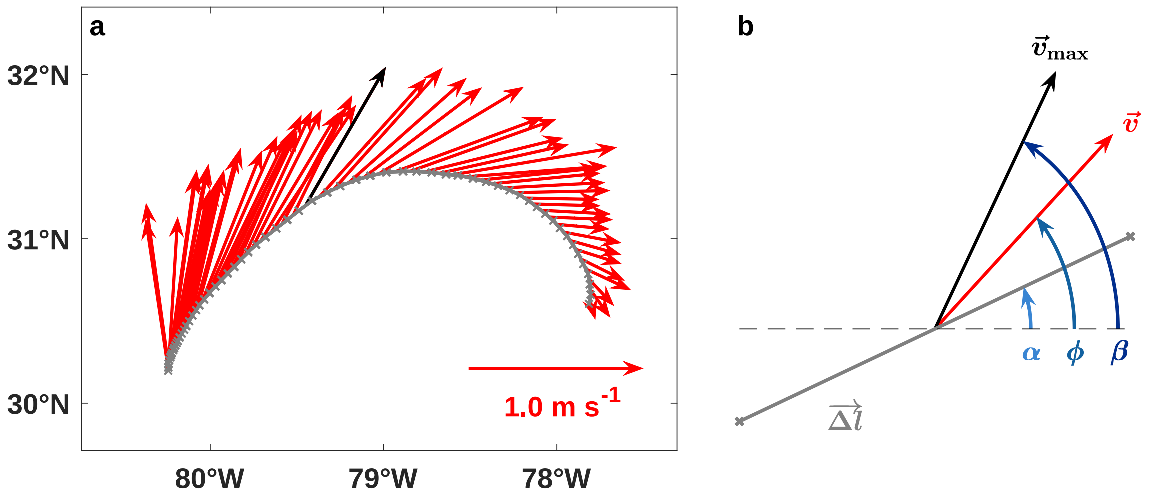

Figure 2-7: (a) Example transect from a mission near 31°N during July 2015. Gray line segments correspond to the glider displacements $\mathbf{\Delta l}$ during each dive with locations of GPS fixes denoted by crosses. Depth-average currents $\mathbf{v}_{\mathrm{DA}}$ for each dive are shown as red arrows. The dive with the maximum transport per unit distance for the entire transect $\mathbf{v}_{\mathrm{max}}$ is highlighted in black. A unit arrow is shown for scale in the lower-right corner. (b) Zoomed version of (a) showing only a single glider dive to highlight the vectors and angles used to calculate transport. The vector $\mathbf{v}$ represents the local current, α is the angle of the glider displacement, ϕ is the angle of the local depth-average current, and β is the angle corresponding to $\mathbf{v}_{\mathrm{max}}$. All angles are measured counterclockwise from east.

where the region A defines the Gulf Stream. For discrete sampling, T is estimated as

$$T = \sum_i \sum_j T_{ij}, \tag{2.2}$$

the sum of the transports T_{ij} through each measurement cell within the bounds of the Gulf Stream. Our coordinate system is such that T_{ij} is positive downstream for the Gulf Stream; we include only $T_{ij} > 0$ in our summation.

The fundamental challenge in estimating the transport of the Gulf Stream (or any other particular current) lies in defining the portion of the total transport through a transect that is to be included in the summation in Eq. (2.2) (see also Knauss

1969; Rossby et al. 2010). The Gulf Stream can exhibit substantial curvature in its path (e.g., Hansen 1970; Levine et al. 1986; Johns et al. 1989), while corotating eddies are frequently located along the edges of the current (Lee and Atkinson 1983; Glenn and Ebbesmeyer 1994). In several cases, the direction of the depth-average flow curves more than 90° over the span of a glider transect (e.g., Fig. 2-7a). These large curvatures are often encountered downstream of Cape Hatteras, as well as in the area around the Charleston Bump (e.g., Fig. 2-7a). The Charleston Bump has been shown to play a role in turning the Gulf Stream through bottom pressure torque (Gula et al. 2015). Curvature is a challenge because defining a single "downstream" direction becomes problematic for transects that are not oriented perpendicular to the Gulf Stream, whether due to platform advection as for gliders or meandering of the current relative to the fixed Line W location. Similarly, corotating eddies are a challenge because we need to decide which portion of the flow contributes to poleward transport or "throughput." To overcome these difficulties, we construct upper and lower bound estimates for the Gulf Stream transport through each transect.

For an upper bound estimate of volume transport, we aim to include the maximum possible transport, so we simply define

$$T_{ij,\text{upper}} = v_{\perp ij}\, \Delta l_i\, \Delta z, \tag{2.3}$$

where $v_{\perp ij} = |\mathbf{v}_{ij}| \sin(\phi_{ij} - \alpha_i)$ denotes the component of the measured velocity that is perpendicular to the local transect segment $\Delta\mathbf{l}_i$ (see Fig. 2-7b); Δl_i is the length of $\Delta\mathbf{l}_i$. The angles ϕ and α are measured counterclockwise from east to the local current direction $\mathbf{v}$ and the transect segment $\Delta\mathbf{l}$, respectively. $\Delta z = 10$ m is the vertical extent of each sampling bin. To compute transport as a function of density rather than depth, we linearly interpolate $v_\perp$ to isopycnal surfaces with a spacing of 0.05 kg m^{-3} and replace Δz with $\Delta\sigma = 0.05$ kg m^{-3} in Eq. (2.3). For the glider observations, $\Delta\mathbf{l}$ is the displacement between the GPS fixes recorded at the beginning and end of a dive. For Line W data, we calculate the displacement $\Delta\mathbf{l}$ from mid-points between the stations that serve as artificial predive/postdive locations. This upper bound is equivalent to cross-stream integration of all flow parallel to the local depth-average current for each profile (e.g., integrating Figs. 2-3g–i). All flow constituting a curved Gulf Stream is included (e.g., all transport in the direction of the red arrows in Fig. 2-7a), but flow as part of nearby eddies, including flow not in the same direction as the Gulf Stream, is also included when those eddies remain within selected transects.

For a lower bound estimate of volume transport, we seek to exclude the contributions due to adjacent eddies and flow in directions other than that of the Gulf Stream. We accomplish this by scaling each $T_{ij,\text{upper}}$ based on the angle between the local flow and a chosen representative orientation of the Gulf Stream for that transect. We define

$$T_{ij,\text{lower}} = T_{ij,\text{upper}} \cos(\phi_{ij} - \beta), \tag{2.4}$$

where β is the orientation of $\mathbf{v}_{\text{max}}$, the depth-average current for the profile with the maximum transport per unit along-track distance for a given transect (e.g., black arrow in Fig. 2-7). Transport per unit along-track distance is simply the depth-average speed $|\mathbf{v}_{\text{DA}}|$ times the profile depth H. For transects in which the depth-average current is strongest in shallow regions near the edges of the transect and the Gulf Stream is curved (e.g., Fig. 2-7a), this definition of $\mathbf{v}_{\text{max}}$ better captures the direction of the core of the Gulf Stream than choosing the direction of the maximum depth-average current to define β. We use this technique for our lower bound estimate since it guarantees a smaller total transport $[\cos(\phi_{ij} - \beta) \leq 1]$ than the upper bound, whereas attempting to compute transport in a streamwise coordinate system may lead to larger or smaller transport estimates when nonparallel flow exists (see Halkin and Rossby 1985). The lower bound at least partially excludes contributions from corotating eddies, since only transport into the direction of the Gulf Stream core (i.e., $\mathbf{v}_{\text{max}}$) is considered. Flow that is oriented more than 90° from $\mathbf{v}_{\text{max}}$ makes no contribution to the lower bound transport estimate.

Having estimated the T_{ij} for both our upper and lower bound transports, we next determine the limits of integration [area A in Eq. (2.1)]. We look for a 4-connected region (i.e., pixels share adjoining edges) of $T_{ij} > 0$ using edge-finding

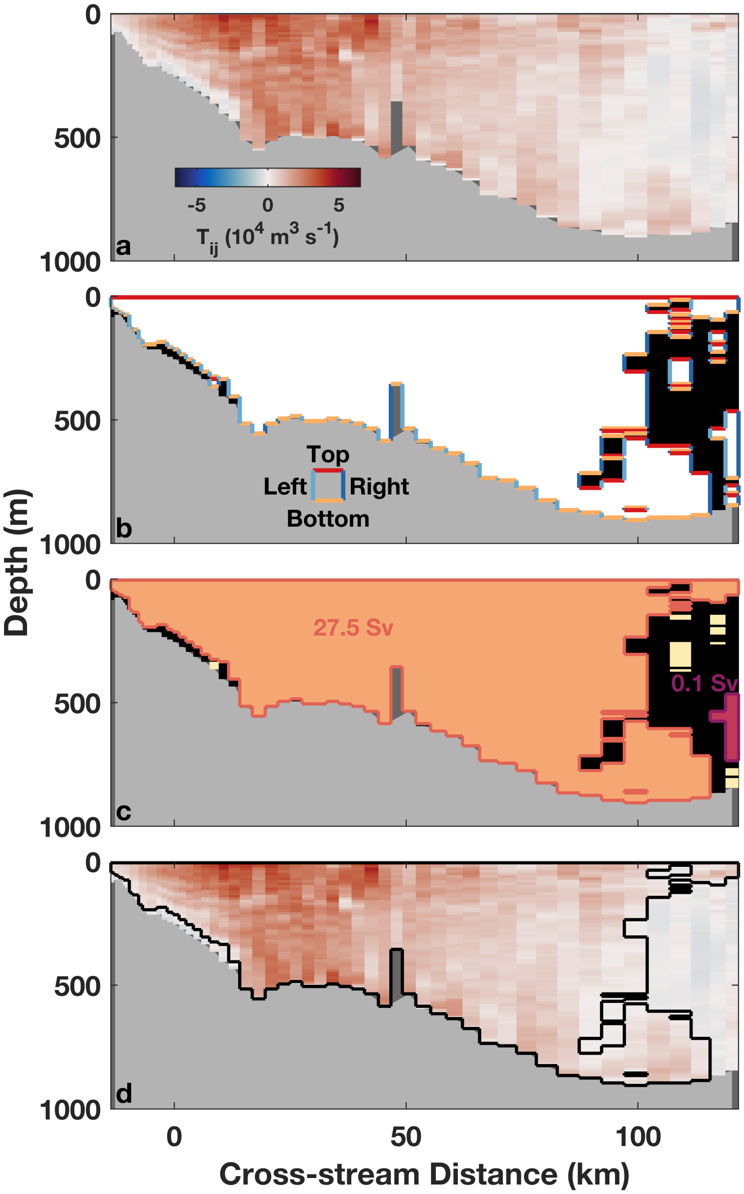

Figure 2-8: Step-by-step example illustrating the procedure for determining limits of integration for transport calculations in Eq. (2.1). The bathymetry as measured by the glider's AD2CP is shaded light gray. Dark gray indicates regions where there are no data. (a) $T_{ij,\text{lower}}$ for the transect shown in Fig 2-7a. (b) Binary matrix that has value 1 (white) when $T_{ij} > 0$ and 0 otherwise (black). Top/bottom/left/right edges of regions of positive T_{ij} are drawn in indicated colors. (c) Connected regions of positive T_{ij} and their correspondingly colored edges. The orange region with the largest transport is the Gulf Stream, the magenta region contains the second largest transport. Regions with smaller transports are shown in yellow. As in (b), black indicates regions where T_{ij} is negative. (d) T_{ij} as in (a) with the resulting integration boundary of the Gulf Stream in black.

methods adapted from image processing. Figure 2-8 shows a step-by-step example of the process by which we determine the integration limits. From the T_{ij} (Fig. 2-8a), we create a binary matrix that has value 1 when $T_{ij} > 0$ and 0 otherwise (Fig. 2-8b). Horizontal and vertical differences of this matrix allow for unambiguous identification of sampling cells (pixels) that are along the edges of connected regions; each pixel is labeled with a binary code describing whether it is a left, right, top, and/or bottom edge of, interior to, or exterior to a connected region of $T_{ij} > 0$ (Fig. 2-8b). We then trace and label edge pixels while requiring 4-connectivity (i.e., pixels have to be connected to their regions through at least one edge and not only a corner). Starting from an identified edge pixel, we determine the location of the next connected edge pixel based on the label of the current pixel. After completing a circuit along connected edges, we assign a unique label to the resulting connected region. The process is repeated starting from an uncategorized edge pixel until all pixels with $T_{ij} > 0$ are assigned to connected regions (Fig. 2-8c). The region with the largest transport within a transect is taken to be the Gulf Stream and its edge is the limit of integration for the Gulf Stream transport estimate (Fig. 2-8d).

Two example transects illustrate the effect of the upper and lower bound definitions on volume transport estimates (Fig. 2-9). For a transect with almost no curvature in the Florida Strait (Fig. 2-9a), the $T_{ij,\text{upper}}$ and $T_{ij,\text{lower}}$ are essentially the same (Figs. 2-9c,e) and the resulting upper and lower bound transport estimates of 36.8 and 36.4 Sv, respectively, are almost equal. On the other hand, for a transect with strong curvature near 31°N in the vicinity of the Charleston Bump (Fig. 2-9b), the two T_{ij} fields and the corresponding integration limits differ substantially (Figs. 2-9d,f), resulting in volume transport estimates that differ by about 15 Sv.

Upper and lower bound volume transport estimates are computed for each individual glider and Line W transect following the procedure above (circles and squares in Fig. 2-10). We use AD2CP-based velocities for the glider transport calculations when available (142 transects; filled circles) and geostrophic velocity estimates otherwise (13 transects; open circles). Line W transport estimates are based on velocities measured by LADCPs (13 transects; squares).

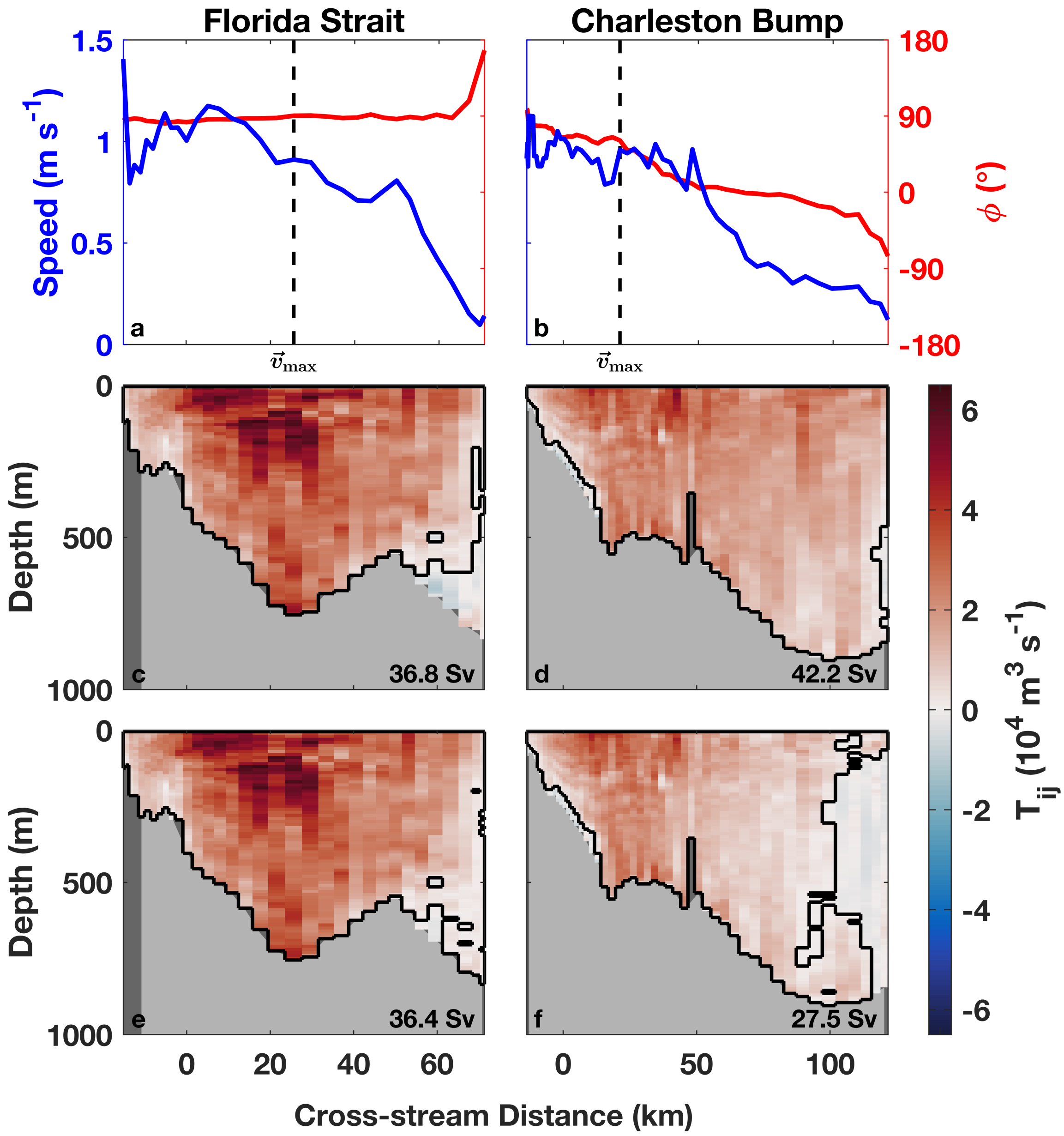

Figure 2-9: Two example transects across the Gulf Stream (left) from the Florida Strait and (right) in the vicinity of the Charleston Bump (same transect as shown in Figs. 2-7 and 2-8). (a),(b) Speed (blue) and direction clockwise from east (ϕ; red) of depth-average currents. The location of $\mathbf{v}_{\max}$ is indicated by dashed vertical black lines. (c),(d) Upper bound of the transport through each cell ($T_{ij,\text{upper}}$). (e),(f) Lower bound of the transport through each cell ($T_{ij,\text{lower}}$). In (c)–(f), the black line outlines the region of integration for transport calculations. Light gray indicates the bathymetry as measured by the glider's AD2CP, while regions without data are dark gray. Corresponding volume transport estimates are shown in the lower right of (c)–(f).

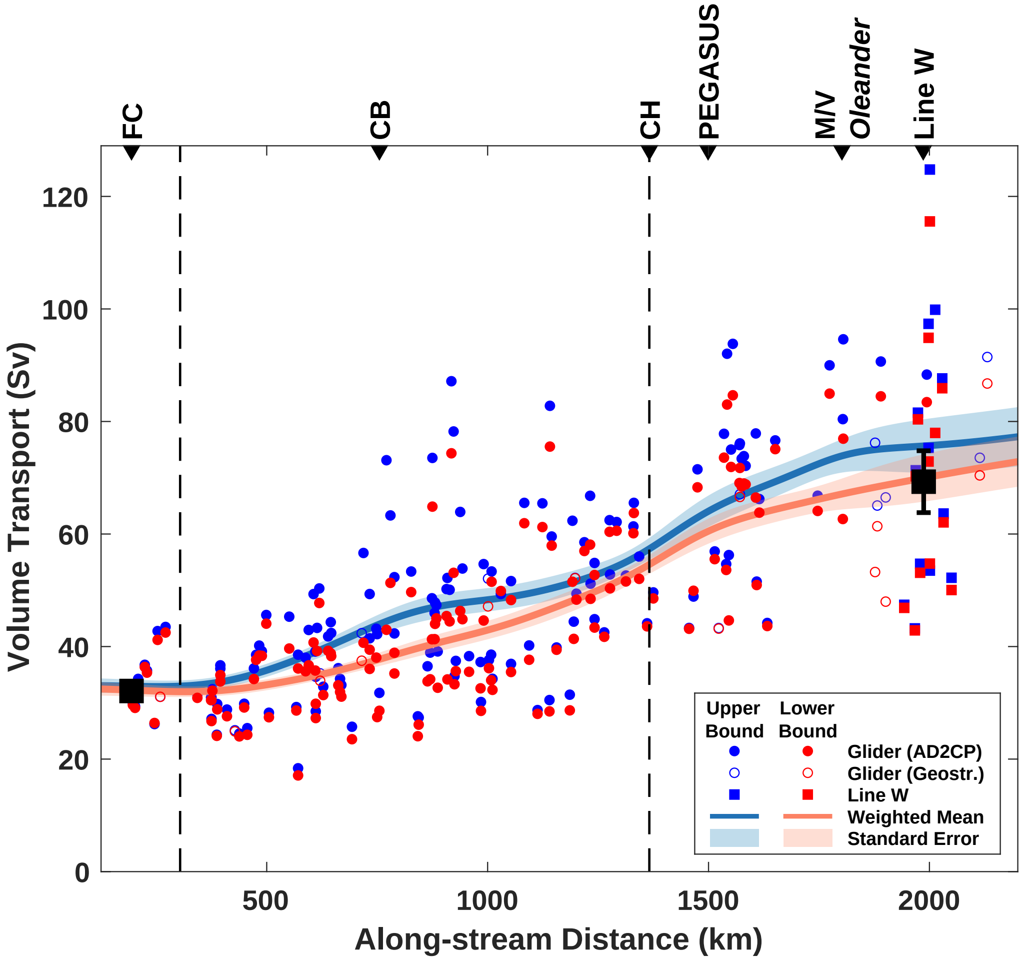

Figure 2-10: Gulf Stream volume transport estimates in the upper 1000 m as a function of along-stream distance from 25°N for both the upper and the lower bound (see legend in the lower right). Individual transport estimates (symbols) are from glider transects across the full width of the Gulf Stream (using either direct velocity measurements from AD2CPs or mapped geostrophic velocities) and from shipboard LADCP casts along Line W. A Gaussian-weighted running mean with 200-km scale (lines) and the bootstrapped standard error of the weighted mean (shading) are shown. Mean volume transport estimates from cable measurements as part of the Western Boundary Time Series in the Florida Strait (Meinen et al. 2010) and from Line W as calculated in Andres et al. (2020) are shown as black squares with whiskers indicating the standard error of the mean. The standard error of ±0.2 Sv from Meinen et al. (2010) is too small to be visible. Black triangles on the upper axis indicate the along-stream distances of important geographic locations and sustained transport measurement sites: Florida Cable (FC), Charleston Bump (CB), The Point at Cape Hatteras (CH), PEGASUS line near 73°W, *Oleander* line, and Line W. The dashed vertical lines distinguish the three different dynamical regions with boundaries as defined in the text: FS, SAB, MAB (from left to right).

To assess the effect of instrumental errors on our transport estimates, we propagate the 0.1 m s^{-1} errors on glider-based velocity profiles (see section 2.2.1) and the 0.05 m s^{-1} errors on Line W LADCP profiles (section 2.2.2) through the transport estimates for each transect. The resulting mean and standard deviation of errors is 0.4 ± 0.1 Sv for both types of estimates and both bounds. Although the uncertainty in LADCP velocity estimates is smaller than the uncertainty in glider-based AD2CP velocities, the larger station spacing results in similar transport errors. These instrumental errors are small compared to the magnitudes of the transports in question. Defining the Gulf Stream and its edges/integration bounds likely presents a larger source of uncertainty in transport estimates that is more difficult to quantify. Our construction of upper and lower bounds of transport estimates seeks to ameliorate this difficulty. Variability in transport on time scales shorter than the 5 days typically required to occupy a transect is not resolved. Glider-based measurements will underestimate Gulf Stream transport when the gliders did not reach the edge of the Gulf Stream, such as in cases for which the 100-m isobath defines the inshore edge for operational reasons. However, transport contributions on the shelf are minimal even for high current velocities due to the shallow depths. Assuming current velocities of 1 m s^{-1}, missing 10 km of Gulf Stream width in water shallower than 100 m would underestimate the transport by less than 1 Sv.

2.3.1.3 Along-stream evolution of volume transport

When volume transport is plotted as a function of the along-stream position for each transect, the well-known increase in volume transport between the Florida Strait and New England becomes apparent (circles and squares in Fig. 2-10). However, both upper and lower bound transport estimates exhibit significant variation between transects at similar along-stream positions. As Rossby et al. (2010) noted, interpreting transport variations between successive transects is difficult if the transects do not reach the physical boundaries of a basin or channel. This transect-to-transect variability at fixed along-stream positions, noted early on by Iselin (1940), is attributable to eddy activity, inherent Gulf Stream variability, and other variable forcing including hurricanes (e.g., Todd et al. 2018).

To estimate time-mean Gulf Stream transport as a function of along-stream distance, we smooth over the transect-to-transect variability using a running weighted mean with a Gaussian window that has a characteristic length scale of 200 km. This along-stream smoothing scale is chosen based on the typical along-stream extent of individual cross-Gulf Stream glider transects (Fig. 2-6), which sets a lower limit on the along-stream resolution of our transport estimates. This 200-km scale is consistent with previous estimates of typical length scales in the Gulf Stream from a satellite altimetry-assimilating model (Mellor and Ezer 1991). Along-stream length scale estimates purely based on observations are lacking since there are no continuous subsurface measurements with high enough spatial resolution. By applying the sliding window, we obtain upper- and lower-bound estimates of volume transport as a function of along-stream distance (lines in Fig. 2-10). The standard errors of the weighted means (shading in Fig. 2-10) are obtained by bootstrapping following Gatz and Smith (1995) and give an indication of how sensitive the time means are to any one transect. The bootstrapped errors are generally less than 5 Sv.

Glider-based volume transport estimates at key locations (Table 2.1) agree well with independent estimates at those locations. The upper and lower bound estimates of 32.9 ± 1.2 Sv and 32.3 ± 1.1 Sv, respectively, in the Florida Strait agree to within error bars with estimates from the Western Boundary Time Series; Meinen et al. (2010) estimated a long-term-mean transport of 32.1 ± 0.2 Sv from motionally-induced voltage differences in a submarine cable across the Florida Strait referenced to repeat ship-based observations (FC in Figs. 2-1 and 2-10). Our estimates for the Florida Strait include some transport contribution from the Antilles Current north of the Bahamas, which explains the slightly higher transport values compared to Meinen et al. (2010). Leaman et al. (1989) estimated a Gulf Stream transport of 86.8 Sv through the PEGASUS line near 73°W (maroon line in Fig. 2-1). Glider-based estimates of volume transport in the upper 1000 m at the same along-stream distance (about 1500 km) capture 70%–74% of the transport measured over the upper 2000 m by Leaman et al. (1989). Andres et al. (2020) used shipboard ADCP data to estimate

Table 2.1: Volume transport by water class at selected locations: Florida Cable (FC), Charleston Bump (CB), The Point at Cape Hatteras (CH), PEGASUS line near 73°W, *Oleander* line, and Line W. The total corresponds to the lines in Fig. 2-10. For each location and water class (see classifications in Fig. 2-13), the upper row shows the absolute transport (Sv) and the fraction of the total transport (%) for the upper bound. The lower row (italic) corresponds to the lower bound. The individual water class transports do not exactly sum up to the total because a few transects with multiprofile gaps in CTD data are excluded from the water class analysis.

	FC		**CB**		**CH**		**PEGASUS**		***Oleander***		**Line W**	
Total	32.9 ± 1.2		44.0 ± 1.8		57.3 ± 1.9		64.1 ± 2.8		73.8 ± 2.9		75.6 ± 4.7	
	32.3 ± 1.1		*37.7 ± 1.2*		*54.5 ± 1.7*		*60.5 ± 2.2*		*67.1 ± 2.7*		*69.9 ± 4.2*	
MABW	0.1 ± 0.0	0%	0.1 ± 0.0	0%	0.3 ± 0.1	0%	0.6 ± 0.2	1%	2.2 ± 0.4	3%	2.8 ± 0.4	4%
	0.1 ± 0.0	*0%*	*0.1 ± 0.0*	*0%*	*0.2 ± 0.1*	*0%*	*0.5 ± 0.2*	*1%*	*1.7 ± 0.3*	*3%*	*2.5 ± 0.4*	*4%*
SW	5.7 ± 0.6	17%	4.9 ± 0.4	11%	2.2 ± 0.5	4%	2.0 ± 0.7	3%	2.0 ± 0.6	3%	2.5 ± 0.6	3%
	5.6 ± 0.6	*17%*	*4.4 ± 0.4*	*12%*	*2.1 ± 0.5*	*4%*	*2.0 ± 0.6*	*3%*	*1.8 ± 0.5*	*3%*	*2.3 ± 0.6*	*3%*
TW	8.6 ± 0.7	26%	12.0 ± 0.8	28%	13.9 ± 0.9	25%	15.0 ± 1.1	24%	14.5 ± 1.2	20%	13.1 ± 1.2	17%
	8.4 ± 0.7	*26%*	*10.4 ± 0.5*	*28%*	*13.4 ± 0.9*	*25%*	*14.4 ± 1.1*	*24%*	*13.5 ± 1.2*	*20%*	*12.4 ± 1.2*	*18%*
EDW	12.4 ± 0.6	38%	18.1 ± 0.8	41%	25.1 ± 1.0	44%	28.5 ± 1.4	45%	34.3 ± 1.6	47%	38.4 ± 3.0	51%
	12.2 ± 0.6	*38%*	*15.4 ± 0.6*	*41%*	*23.7 ± 0.9*	*44%*	*26.6 ± 1.2*	*44%*	*30.7 ± 1.6*	*47%*	*35.2 ± 2.6*	*51%*
IW	3.0 ± 0.3	9%	4.7 ± 0.3	11%	7.1 ± 0.3	13%	8.4 ± 0.5	13%	10.2 ± 0.5	14%	10.4 ± 0.8	14%
	2.9 ± 0.2	*9%*	*3.9 ± 0.2*	*10%*	*6.7 ± 0.3*	*12%*	*7.8 ± 0.4*	*13%*	*9.2 ± 0.5*	*14%*	*9.6 ± 0.7*	*14%*
uLSW	0.0 ± 0.0	0%	1.0 ± 0.2	2%	6.9 ± 0.5	12%	8.1 ± 0.7	13%	9.1 ± 0.9	12%	7.6 ± 1.1	10%
	0.0 ± 0.0	*0%*	*0.7 ± 0.1*	*2%*	*6.6 ± 0.5*	*12%*	*7.8 ± 0.6*	*13%*	*8.4 ± 0.9*	*13%*	*7.2 ± 1.1*	*10%*
AAIW	2.9 ± 0.3	9%	2.9 ± 0.3	7%	1.2 ± 0.2	2%	1.0 ± 0.2	2%	0.6 ± 0.1	1%	0.5 ± 0.2	1%
	2.8 ± 0.3	*9%*	*2.5 ± 0.2*	*7%*	*1.2 ± 0.2*	*2%*	*1.0 ± 0.2*	*2%*	*0.6 ± 0.1*	*1%*	*0.5 ± 0.2*	*1%*

Gulf Stream transports of 60.6 Sv in the upper 600 m along the *Oleander* line, which is 82%–90% of our estimate of transport for the upper 1000 m (Table 2.1). Andres et al. (2020, their Table A1) estimated an upper-1000-m transport of 69.3 ± 5.5 Sv using only Line W observations, similar to our upper and lower bound transport estimates of 75.6 ± 4.7 Sv and 69.9 ± 4.2 Sv, respectively, from the combination of Line W and glider-based observations. However, Andres et al.'s estimates for individual Line W transects may differ from our estimates, in part because they computed transports in a cross-line coordinate system with a single downstream direction for each transect defined by the maximum near-surface velocity and included some profiles that we exclude based on the orientation of depth-average flow. Andres et al. (2020) also reported independent transport estimates from two moorings that observed the Gulf Stream at Line W between 2010 and 2014. Their mooring-based transport estimate of 78.2 Sv is slightly higher than our estimate but is based on construction of a time-mean Gulf Stream transect from which transport is computed. Overall, the comparison with independent estimates shows that gliders are well suited to measure transport in western boundary currents.

Volume transport increases relatively steadily between the northern end of the Florida Strait (along-stream distance of about 300 km) and Line W (along-stream distance of about 2000 km). Assuming linear growth and averaging the upper and lower bound slopes, transport in the upper kilometer increases by about 2.4 Sv every 100 km between those two locations. For comparison, Knauss (1969) estimated that full-depth transport increases at a rate of "7% over 100 km over a distance of 2000 km downstream of the Florida Straits."

Differences between the upper and lower bound transport estimates are largest offshore of South Carolina (along-stream distance of about 750 km), a region that is known for curvature and meanders caused by instabilities in the lee of the Charleston Bump (Gula et al. 2015; Zeng and He 2016). Downstream of Cape Hatteras (>1366 km), the errors on mean transports grow due to a combination of reduced sampling and high Gulf Stream variability. Nevertheless, it appears that differences between upper- and lower-bound transports are elevated in this area where the lack of a stabilizing

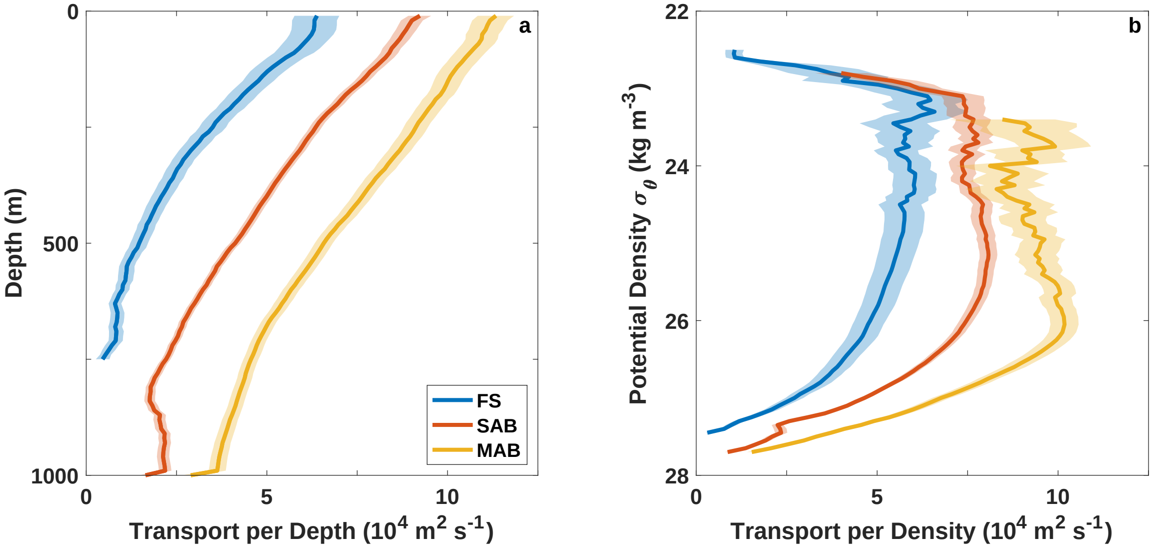

Figure 2-11: Vertical structure of volume transport in the FS, MAB, and SAB as a function of (a) depth and (b) potential density σ_θ. The shading indicates the respective standard error of the mean.

topographic slope allows for the formation of large meanders and eddies.

Following the procedure described in section 2.3.1.2 without integrating in depth, we estimate the vertical transport profiles for individual transects in both depth and density coordinates. To examine the Gulf Stream structure and transport in the different dynamical regions, we compute the mean of transport profiles within the FS, SAB, and MAB regions (Fig. 2-11). The transport in the upper 1000 m increases barotropically (i.e., uniformly throughout the water column) over the three different regions (Fig. 2-11a); transport is highest at the surface and decreases relatively linearly with depth. Near-surface waters become denser as the Gulf Stream flows northward and cools, so most of the transport occurs in denser water classes in the MAB (Fig. 2-11b). Our observations agree with Hogg (1992), who also observed a downstream barotropic transport increase and nearly constant baroclinic transport in direct velocity observations downstream of Cape Hatteras.

The along-stream increase in Gulf Stream transport must be due to a combination of deepening, acceleration, and/or broadening of the Gulf Stream. Many observational campaigns have shown that the Gulf Stream indeed reaches deeper as the seafloor deepens downstream of Cape Hatteras; it extends to the seafloor in waters greater than 4000 m deep (e.g., Hall and Bryden 1985; Johns et al. 1995; Andres et al. 2020). We capture the depth-related increase in transport as the Gulf Stream moves from the Florida Strait, over the Blake Plateau, and into deeper water at Cape Hatteras (Fig. 2-11), but since the gliders only sample the upper kilometer of the ocean, our analysis cannot fully address increases in transport due to the Gulf Stream reaching deeper than 1000 m. To address whether Gulf Stream speeds increase in the downstream direction, we compute a transport-weighted velocity ($\langle \mathbf{v} \rangle = \sum T_{ij} \mathbf{v}_{ij} / \sum T_{ij}$) using the individual upper- and lower-bound transport measurements T_{ij} as weights for all transects with Doppler current profiler data. We apply the Gaussian weighted mean and bootstrapping described in section 2.3.1.3 and then take the magnitude of the result as the transport-weighted speed (Fig. 2-12a). The time-average Gulf Stream speed is relatively constant along the U.S. East Coast, suggesting that the along-stream transport increase above 1000 m is due to an along-stream increase in Gulf Stream cross-sectional area. We note, however, that Andres et al. (2020) found a significant change in Gulf Stream speed between the *Oleander* line and Line W, which are separated by too short of a distance for such a difference to be resolved by our analysis. Unfortunately, directly estimating Gulf Stream cross-sectional area from the available observations is not possible since transects are oriented obliquely and the Gulf Stream curves and evolves along its path. However, we can estimate the Gulf Stream area by dividing our time-average transport estimate by the time-average speed estimate (Fig. 2-12b). This calculation provides a rough estimate of the along-stream increase in Gulf Stream cross-stream area; addressing these changes more accurately requires a numerical model that can be sampled orthogonal to the local flow. Nevertheless, it is clear that most of the along-stream transport increase in the Gulf Stream stems from broadening and deepening of the current, rather than from increasing current speeds.

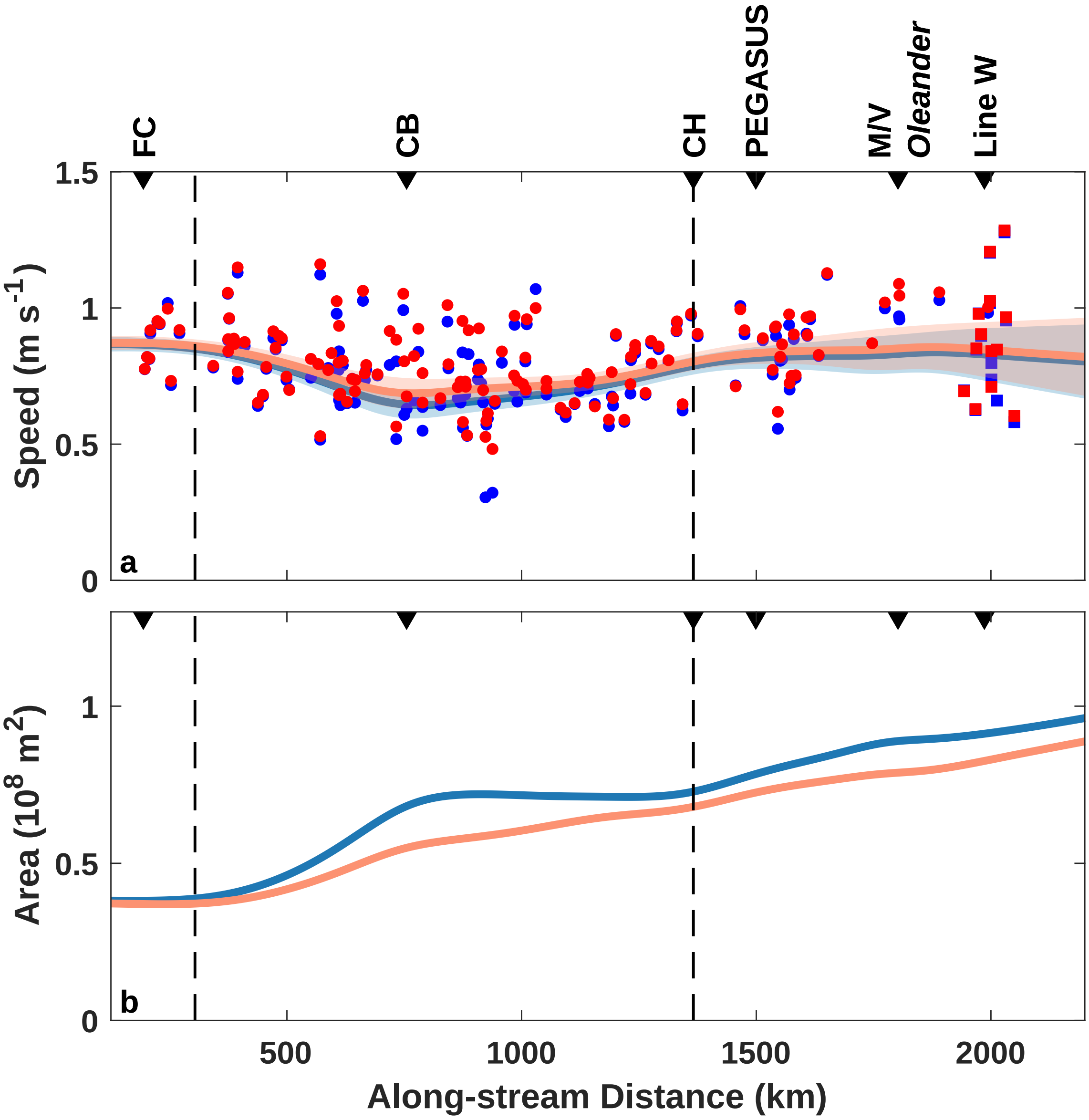

Figure 2-12: (a) Transport-weighted speed and (b) inferred Gulf Stream area above 1000 m as functions of along-stream distance. Colors, lines, symbols, vertical dashed lines, and location indicators as in Fig. 2-10. The shading is the standard error of the weighted mean velocity and assumes that all of the error in velocity is due to an error in speed and not direction.

Table 2.2: Potential temperature θ, salinity S, and potential density σ_θ of labeled water class box vertices in Fig. 2-13.

Vertex #	θ (° C)	S	σ_θ (kg m^{-3})
1	4.05	34.76	27.6
2	9.15	35.16	27.2
3	11.47	35.40	27.0
4	17.35	35.75	26.0

2.3.2 Water class contributions

With concurrent measurements of water properties and currents distributed along the Gulf Stream's path, the combined glider and Line W observations are uniquely suited to examine the characteristics of waters transported in the Gulf Stream, where they are entrained, and how they contribute to the Gulf Stream's time-mean increase in along-stream transport. We divide the total volume transport for each transect (Fig. 2-10) into multiple water classes based on potential temperature θ, salinity, and potential density σ_θ (Fig. 2-13, Table 2.2). These water classes are more broadly defined than typical for specific "water masses" so as to include all observed water properties in a manageable number of categories. Water classes are chosen to allow direct comparison between our results and those of Szuts and Meinen (2017) in the Florida Strait, but with additional divisions in θ–S space to account for the larger region and wider range of water properties in our observations. We distinguish the following water classes:

- high-salinity, near-surface Gulf Stream waters (SW; Szuts and Meinen 2017);
- warm, salty Gulf Stream thermocline waters (TW) including Salinity Maximum Water (Toole et al. 2011; Qu et al. 2013);
- Eighteen Degree Water (Worthington 1959; Talley and McCartney 1982) and related waters below the thermocline (EDW);
- fresher, near-surface waters from the Middle Atlantic Bight shelf and the Slope Sea (MABW), including the Ford Water (Ford et al. 1952);

- upper Labrador Sea Water (uLSW);
- Antarctic Intermediate Water (AAIW);
- and other intermediate waters (IW).

Surface waters (SW) are lighter than 24 kg m^{-3} and middepth waters (TW and EDW) are between 24 and 27 kg m^{-3} (Szuts and Meinen called these intermediate waters). We subdivide the middepth waters into TW and EDW based on the 26 kg m^{-3} isopycnal. MABW was not encountered in Szuts and Meinen's observations in the Florida Strait. We define MABW to be lighter than 27 kg m^{-3} and fresher than 35.75 except at potential densities greater than 26 kg m^{-3}, where we require it to be progressively fresher with increasing density in order to distinguish it from EDW (Fig. 2-13). Our definition of MABW includes a wide range of properties. At potential densities greater than 27.2 kg m^{-3}, two distinct modes are apparent in the θ–S distribution (Fig. 2-13), motivating our distinction between saltier uLSW and fresher AAIW. Following Pickart and Smethie (1993), we take uLSW to be denser than 27.4 kg m^{-3}. Based on where the two modes of the θ–S distribution merge (vertex 2 in Fig. 2-13), we define AAIW to be colder than 9.15 °C. Similar to the distinction between MABW and EDW, we also use a linear function in θ–S space to separate uLSW and AAIW based on the appearance of the two distinct modes. Details of the linear functions that are used to delineate water classes can be found in Table 2.2, which contains coordinates of the numbered vertices in Fig. 2-13. Remaining waters denser than 27 kg m^{-3} are then simply categorized as IW. Szuts and Meinen (2017) classified all waters denser than 27 kg m^{-3} as AAIW; uLSW was not encountered in their observations in the Florida Strait and they did not distinguish between IW and AAIW based on temperature.

For each cross-Gulf Stream transect, every transport element T_{ij} is assigned to a water class based on measured water properties. We then compute the upper and lower bounds of time-mean volume transport as a function of along-stream distance separately for each water class, following the method described in section 2.3.1. The results (Fig. 2-14a) elucidate the spatially dependent contributions of each water

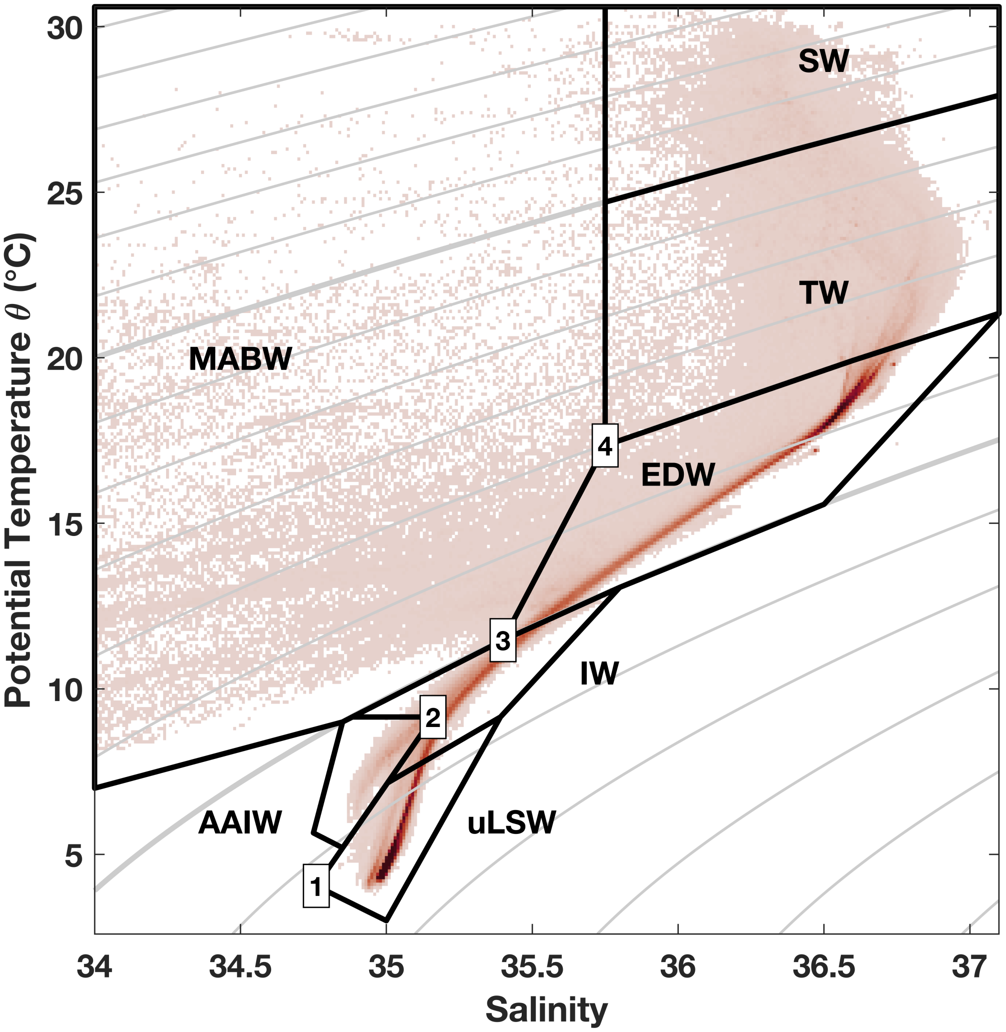

Figure 2-13: Joint probability density function for potential temperature θ and salinity using all available glider observations. Gray contours are isopycnals with a contour interval of 0.5 kg m^{-3} and the 24.0 and 27.0 kg m^{-3} isopycnals bold. Black regions delineate the following water classes: Gulf Stream surface water (SW); Gulf Stream thermocline waters (TW); Eighteen Degree Water and related subthermocline waters (EDW); upper Labrador Sea Water (uLSW); Antarctic Intermediate Water (AAIW); other intermediate waters (IW); and fresher waters that have been influenced by the Middle Atlantic Bight shelf waters (MABW). The MABW region extends to much lower salinities than shown to capture the freshest waters encountered. Coordinates of the numbered vertices used to delineate water classes are given in Table 2.2. Water class boundaries not including numbered vertices either follow isolines of potential density σ_θ, potential temperature θ, or salinity, or they are arbitrarily positioned outside of the range of observed water properties.

class to Gulf Stream volume transport. We also compute the fractional contribution of each water class to total transport (Fig. 2-14b). Since the upper and lower bound volume transport estimates by water class are similar, we only show the upper bound estimates in Fig. 2-14. Table 2.1 provides both upper and lower bound transport estimates at selected locations. The sum of transports in distinct water classes in Fig. 2-14a approximates the upper bound total transport (blue line in Fig. 2-10), but the two estimates do not agree exactly because five transects with multiprofile gaps in the CTD data had to be excluded from the water class analysis (see Table 2.1).

Most of the along-stream increase in Gulf Stream volume transport is due to entrainment of EDW and, to a slightly lesser extent, uLSW and IW (Fig. 2-14, Table 2.1). Transport of EDW increases by about 25 Sv between the Florida Strait and Line W. Entrainment of uLSW becomes more prominent near the Charleston Bump (along-stream distance of about 750 km). At Line W, uLSW contributes approxi-

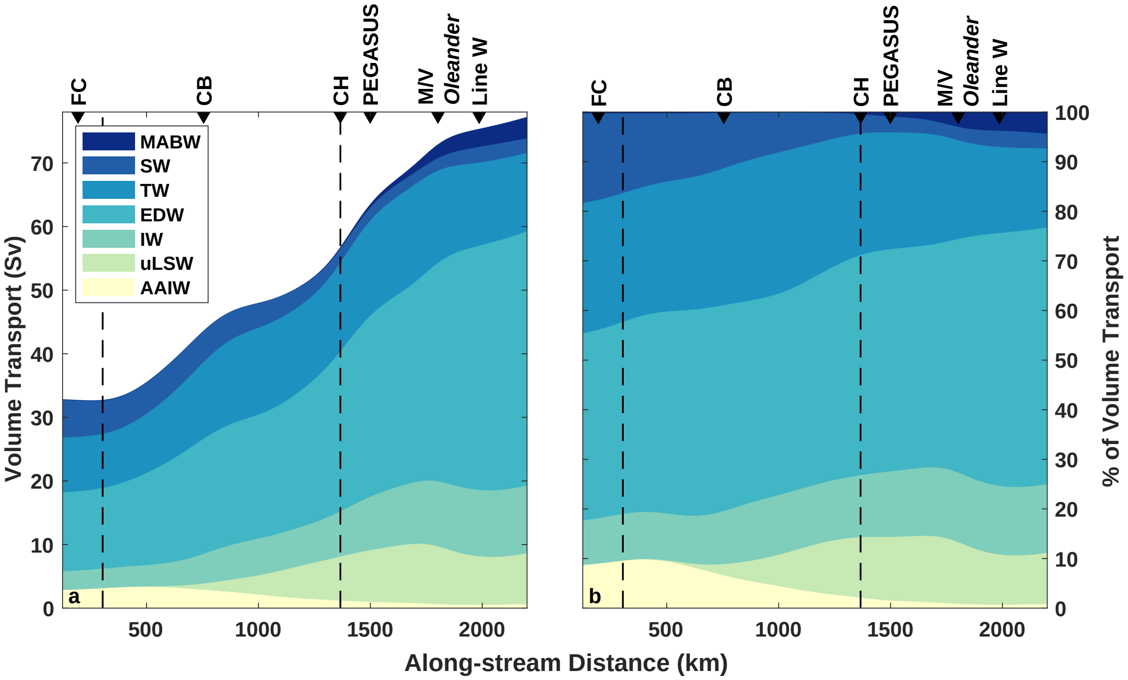

Figure 2-14: Along-stream evolution of Gulf Stream volume transport by water class (as defined in Fig. 2-13) using the upper bound transport estimates. (a) Stacked area plot of absolute volume transport for each water class. (b) Volume transport by water class as a fraction of the total transport. Vertical dashed lines and triangular tick marks on the upper axes are as in Fig. 2-10.

mately 7–8 Sv or about 10% of the total transport above 1000 m. While the fraction of EDW transported in the Gulf Stream increases, the relative transport contribution of uLSW also becomes more important downstream (Fig. 2-14b). It is interesting to note that the glider observations allow us to identify poleward-flowing uLSW in the Gulf Stream well south of Cape Hatteras, suggesting a process driving entrainment from the DWBC into the Gulf Stream south of Cape Hatteras. The transport of waters classified as IW increases by about a factor of 3 downstream in concert with increases in EDW and uLSW transport, as would be expected for these waters that lie on a mixing line between adjacent water classes.

As anticipated, MABW is only encountered north of Cape Hatteras (>1366 km, Fig. 2-14). It makes up only a small fraction of total Gulf Stream transport (3 Sv, 4% at Line W), but this is notably more than the typical < 1 Sv of transport encountered on the MAB shelf (Linder and Gawarkiewicz 1998; Lentz 2008; Todd 2020) due to mixing with Slope Sea and Gulf Stream waters during entrainment.

The absolute and fractional transport of AAIW within the Gulf Stream decreases downstream (Fig.2-14). The AAIW signature in θ–S space is eroded as the Gulf Stream flows northward from the Florida Strait, in part due to near-bottom mixing over the Blake Plateau (Todd 2017), but can be traced at least as far as Line W. Previous studies have identified AAIW at different locations in the Gulf Stream using its unique nutrient, oxygen, and silica signatures [e.g., Atkinson (1983) at 31°N and Tsuchiya (1989) at 60°N]. Combined with our observations, these studies suggest that AAIW is likely carried far downstream in the Gulf Stream but modified along the way.

The transport of waters classified as SW also decreases downstream (Fig. 2-14). The combination of heat loss to the atmosphere, which leads to cooling and reclassification as TW, and mixing with entrained MABW likely accounts for this decrease despite the increase in transport in the downstream direction at all depths (Fig. 2-11).

Our transport estimates by water class agree well with prior results from Szuts and Meinen (2017) in the Florida Strait. They estimated that 14% of the Florida Current transport comes from AAIW, similar to our estimate of 18% for the combination of

AAIW and IW. Szuts and Meinen observed a larger fraction of surface waters (27% vs our 17%). Consequently, the fraction of waters with properties last set in the North Atlantic (a combination of EDW and TW) is slightly lower in Szuts and Meinen than for the glider-based estimates presented here (55% vs our 64%).

2.4 Summary and conclusions

Using a combination of glider-based cross–Gulf Stream transects and shipboard observations along Line W, this analysis characterizes the time-mean along-stream evolution of Gulf Stream volume transport in the upper kilometer of the ocean. Using two different definitions of Gulf Stream transport, we provide both an upper and a lower bound for Gulf Stream transport in the different dynamical regimes along the U.S. East Coast (Fig. 2-10). Our analysis confirms the well-known along-stream increase in Gulf Stream volume transport, filling in the large spatial gaps between existing estimates of Gulf Stream transport. The transport estimates reported here are averages of the transport through individual transects; they are not directly comparable to estimates of transport through streamwise mean sections because of the variable width of the Gulf Stream. The concurrent hydrographic and velocity measurements used here additionally allow us to examine how waters of various properties contribute to the Gulf Stream's evolving flow along the U.S. East Coast. Subthermocline waters are the leading contributors to the Gulf Stream's added transport as it flows from the Florida Strait into the open North Atlantic (Fig. 2-14).

Recently detected changes in the behavior of the Gulf Stream (Andres 2016) and other western boundary currents (e.g., Beal and Elipot 2016; Yang et al. 2016), as well as the projected shifts in meridional overturning as a consequence of anthropogenic climate change (e.g., IPCC 2013, and references therein) highlight the importance of understanding the structure, dynamics, and variability of western boundary currents under climatological conditions for improving forecasts. Autonomous underwater gliders enable long-duration, high-resolution monitoring of the upper kilometer of western boundary currents (Davis et al. 2012; Rainville et al. 2013; Rudnick et al.

2013; Schaeffer and Roughan 2015; Schönau et al. 2015; Todd et al. 2016; Krug et al. 2017; Todd 2017). This study presents a first detailed look at the evolution of Gulf Stream transport along the U.S. East Coast, emphasizing the potential of underwater gliders to continuously monitor western boundary currents as the Global Ocean Observing System expands its coverage of ocean boundaries (Todd et al. 2019).

Details of the modification of water masses transported in the Gulf Stream remain to be investigated, particularly in the areas around the Charleston Bump, where near-bottom mixing is enhanced (Todd 2017), and near Cape Hatteras, where the Gulf Stream encounters the deep western boundary current (e.g., Andres et al. 2018). Frequent occurrences of upper Labrador Sea Water south of Cape Hatteras in the glider observations leave many open questions about the pathways of this intermediate water mass and their persistence. Realistic numerical simulations that capture observed Gulf Stream properties and provide water mass distributions below 1000-m depth will be beneficial to such future analyses.

Acknowlegdments. Many people were critical to the success of the Spray glider missions, including Patrick Deane, Larry George, Raymond Graham, Ben Hodges, and Breck Owens at WHOI and Jeff Sherman, Dan Rudnick, Ben Reineman, and Evan Randall-Goodwin of the Instrument Development Group at the Scripps Institution of Oceanography. The Physical Oceanography Division at NOAA's Atlantic Oceanographic and Meteorological Laboratory (AOML) and the University of Miami's Rosenstiel School of Marine and Atmospheric Science (RSMAS) provided laboratory space for glider preparation. The East Carolina University Coastal Studies Institute and North Carolina State University's Center for Marine Sciences and Technology (CMAST) provided support for glider recoveries. We thank Magdalena Andres, John Bane, Glenn Flierl, and John Toole for valuable discussions about Gulf Stream transport and for their thoughtful suggestions and comments on the manuscript. We gratefully acknowledge funding from the Office of Naval Research (N000141713040), the National Science Foundation (OCE-0220769, OCE-1633911, OCE-1923362), NOAA's Global Ocean Monitoring and Observing Program

(NA14OAR4320158, NA19OAR4320074), WHOI's Oceans and Climate Change Institute, Eastman Chemical Company, and the W. Van Alan Clark, Jr. Chair for Excellence in Oceanography at WHOI (awarded to Breck Owens).

Data Availability Statement. Spray glider observations in the Gulf Stream are available from `http://spraydata.ucsd.edu` and should be cited using the following DOI: 10.21238/S8SPRAY2675 (Todd and Owens 2016). Line W shipboard hydrographic data are accessible from the Line W project website (`https://scienceweb.whoi.edu/linew/index.php`). The daily delayed-time (SEALEVEL_GLO_PHY_L4_REP_OBSERVATIONS_008_047) and near-real-time (SEALEVEL_GLO_PHY_L4_NRT_OBSERVATIONS_008_046) absolute dynamic topography products used in this study are provided by the EU Copernicus Marine Environmental Monitoring Service. Colormaps are from Thyng et al. (2016).

Chapter 3

Mechanisms affecting the transport and modification of Antarctic Intermediate Water within the Gulf Stream

Abstract

Three-dimensional mean fields of the upper 1000 m of the Gulf Stream based on observations from Spray underwater gliders show Antarctic Intermediate Water (AAIW) entering the Gulf Stream through the Florida Strait. As the Gulf Stream flows poleward, the low salinity signature of AAIW is eroded away in potential temperature–salinity (θ–S) space until disappearing around the area of the Charleston Bump, an underwater bathymetric feature on the central Blake Plateau in the South Atlantic Bight. Using a Reynolds-averaged advection-diffusion model, the salt fluxes through the boundaries of three different control volumes are estimated to gain a better understanding of the mechanisms contributing to the erosion of AAIW in the Gulf Stream. They reveal that both lateral stirring and vertical mixing likely play important roles. Previous observations have shown that upper Labrador Sea Water (the shallowest water mass transported by the Deep Western Boundary Current which is found in a similar density range as AAIW, but is saltier) is entrained into the Gulf Stream much further south than originally thought. Here, we show that variable flow (e.g., due to the highly variable Antilles Current) allows uLSW to cross isobaths and reach the relatively shallow Blake Plateau, where it is entrained into the Gulf Stream and contributes to the erosion of AAIW. In the future, combining these observations with numerical simulations will shine more light on the persistence of uLSW pathways and allow for the estimation of vertical turbulent diffusive fluxes within the Gulf Stream using the outlined analysis.

3.1 Introduction

The Gulf Stream is a strong western boundary current in the North Atlantic that plays an important role in the redistribution of different water masses, heat, salt, and carbon in the global climate system. As part of the upper limb of the Atlantic Meridional Overturning Circulation (AMOC), it carries warm, salty water masses from the tropics to higher latitudes. On its way northward, the water mass composition of the Gulf Stream changes (e.g., Chapter 2, hereinafter referred to as Heiderich and Todd 2020). Among the water masses advected and modified within the Gulf Stream are two intermediate water masses that are found at middepths in the ocean: Antarctic Intermediate Water (AAIW) and upper Labrador Sea Water (uLSW). AAIW and uLSW are formed remotely at high southern and northern latitudes, respectively, and enter the Gulf Stream at disparate locations. AAIW is eroded as the Gulf Stream flows poleward, while uLSW and other shallower subthermocline waters become entrained (Heiderich and Todd 2020). Here we focus on the erosion of AAIW, aiming to understand how this water mass is modified within the Gulf Stream system. As we show below, one of the processes contributing to the erosion is lateral mixing with uLSW and related waters. These related waters are also salty, but slightly less dense than uLSW and were classified more generally as "intermediate waters" (IW) in Heiderich and Todd (2020).

After flowing through the channel of the Florida Strait, the Gulf Stream enters the South Atlantic Bight where it continues to flow over the relatively shallow ($\lesssim$1000 m) outer continental shelf region called the Blake Plateau. In this region, the Gulf Stream encounters the Charleston Bump, a bathymetric ridge and trough feature near 31.5°N (black star in Fig. 3-1a), before it leaves the continental margin at Cape Hatteras, North Carolina, veers off into the deep ocean and heads towards Europe. Using a set of underwater glider observations, Heiderich and Todd (2020) estimated a joint probability density function of potential temperature θ and salinity S that exhibits two distinct tails representing AAIW and uLSW. In the Gulf Stream, AAIW appears as relatively fresh water at potential temperatures of about 6–9 °C and potential

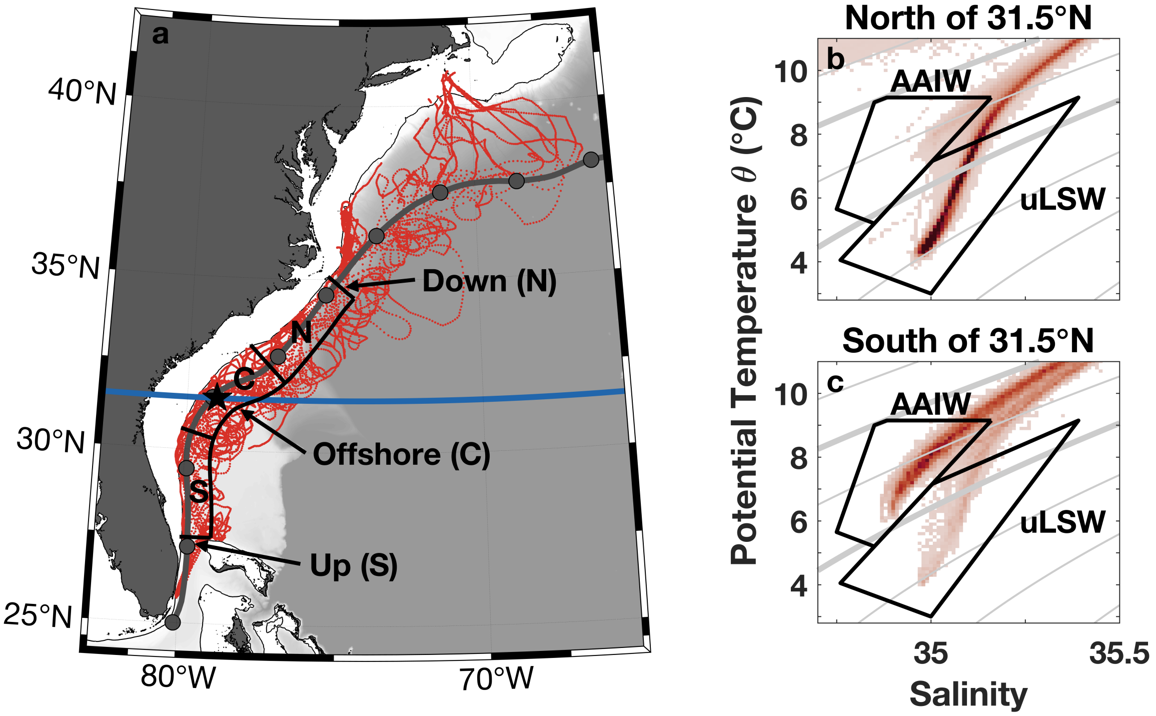

Figure 3-1: (a) Map of the locations of all glider profiles entering the mean fields (red dots). The thick black lines delineate the lateral sides of three control volumes: a southern one (S), a central one (C), and a northern one (N). The upstream boundary of the southern control volume, offshore boundary of the central control volume, and downstream boundary of the northern control volume are annotated with arrows. The thin black lines are the 100-m isobath. The black star indicates the location of the Charleston Bump. The latitude of 31.5°N is shown as a blue line. (b) Joint probability density function of potential temperature θ and salinity S of all glider observations north of 31.5°N. The black outlines delineate two water masses, Antarctic Intermediate Water (AAIW) and upper Labrador Sea Water (uLSW) as defined in Heiderich and Todd (2020). (c) Same as (b), but for all observations south of 31.5°N.

densities between 27.1 and 27.5 kg m^{-3} (see the black outline in Figs. 3-1b,c that follows the water class definitions in Heiderich and Todd (2020)). uLSW is found in a similar potential density range (>27.4 kg m^{-3}), but is notably saltier than AAIW (also indicated with a black outline in Fig. 3-1b,c). The less dense extension of the uLSW tail (i.e., any water in the upper-right corner of the θ–S diagrams that is outside of the black outlines) is what Heiderich and Todd (2020) classified as IW. θ–S diagrams computed analogously to Heiderich and Todd (2020) using more glider observations north and south of the latitude of the Charleston Bump (blue line in Fig. 3-1a) clearly show the downstream modification of AAIW. South of 31.5°N, both the AAIW and uLSW tails are clearly visible with AAIW being more frequently observed (Fig. 3-1c). North of 31.5°N, the low salinity signature of AAIW fades and its distinct tail in the θ–S diagram is eroded, while the uLSW tail dominates (Fig. 3-1b). The disappearance of AAIW in θ–S space suggests that any interactions with other water masses ultimately lead to mixing.

AAIW enters the Gulf Stream through the Florida Strait (Szuts and Meinen 2017), where it contributes around 3 Sv or 9% of total Gulf Stream transport and constitutes the deepest layer (Heiderich and Todd 2020). Its low salinity, low nutrient, and low oxygen signature can be identified over the Blake Plateau up to at least 31°N (Atkinson 1983). Farther north, the low salinity signature of AAIW and thus its contribution to total Gulf Stream transport fades (Heiderich and Todd 2020), but its high silica content is still detectable much further downstream in the Gulf Stream and its extension (also known as the North Atlantic Current) to around 60°N (Tsuchiya 1989).

uLSW is the shallowest component of Labrador Sea Water (LSW) and typically found at depths of 750 m to 1160 m at Line W, a former mooring line near 68°W that also served as a repeat transect for shipboard observations (Toole et al. 2017). LSW is formed through deep convection in the Labrador Sea and carried southward in the Deep Western Boundary Current (DWBC). The DWBC is a deep limb of the AMOC that carries cold water masses from the tail of the Grand Banks of Newfoundland equatorward (Pickart and Watts 1990). These cold water masses are collectively called North Atlantic Deep Water (NADW) and include both LSW and denser Overflow Waters below. Near Cape Hatteras, the DWBC crosses underneath the Gulf Stream. This crossover and the associated pathways of deep and intermediate waters have been the subject of a variety of observational and modeling studies (e.g., Talley and McCartney 1982; Hogg and Stommel 1985; Pickart and Watts 1993; Spall 1996a; Bower and Hunt 2000a,b). Most of these studies suggest that the deeper layers of the DWBC are able to pass by Cape Hatteras and continue to flow equatorward as a subsurface-intensified flow along the continental slope of the western boundary, while the shallower layers become entrained into the Gulf Stream and are therefore diverted into the abyssal interior. However, there is observational evidence that the shallower layers of the DWBC (namely uLSW) can also pass by Cape Hatteras without much mixing with other water masses (e.g., Rhein et al. 2015; Andres et al. 2018). Heiderich and Todd (2020) detected uLSW in the Gulf Stream just north of the Florida Strait, implying that at least some of it is able to continue to flow along the continental margin south of Cape Hatteras. In order to become entrained in the Gulf Stream this far south, uLSW subsequently has to cross isobaths and move up onto the relatively shallow Blake Plateau. Since uLSW and AAIW are found at similar depths and densities, the influx of salty uLSW into the Gulf Stream contributes to the erosion of AAIW.

A variety of processes occurring on the Blake Plateau may contribute to the poleward erosion of the distinct AAIW signature, including topographically controlled processes, lateral processes (e.g., eddy stirring or along-isopycnal mixing), and vertical mixing. Topographic effects are both vertical (e.g., mixing) and horizontal (e.g., eddy formation, transport, steering; Gula et al. 2019) and likely play an important role, since AAIW encounters the Charleston Bump as it flows northward over the Blake Plateau. This area is well-known for elevated near-bottom mixing and large internal waves in the lee of the Bump. Estimates of energy extraction in this region exceed 4000 J m^{-2} and are related to the conversion of kinetic energy from the Gulf Stream into potential energy in thick bottom mixed layers (Todd 2017). Moreover, lateral mixing with saltier uLSW on the offshore side of the Gulf Stream may also lead to the erosion of AAIW. That uLSW is found in the Gulf Stream far upstream of Cape Hatteras (Heiderich and Todd 2020) indicates that this water mass is able to cross isobaths (and thus f/H contours) and suggests that dynamical features like eddies or other variable flows may play a role.

In this chapter, we characterize how AAIW is modified within the Gulf Stream using observations collected by Spray underwater gliders. Motivated by our observation of the erosion of AAIW near the Charleston Bump, we set up control volumes and use salinity as a passive tracer in a time-averaged, Reynolds-decomposed advection-diffusion equation to investigate whether AAIW is eroded through vertical mixing or through lateral processes (e.g., through mixing with the saltier uLSW offshore). Details of the glider observations can be found in section 3.2.1 and the temporal averaging algorithm used to construct the three-dimensional mean fields is outlined in section 3.2.2. Section 3.2.3 briefly summarizes how an along-stream coordinate system is constructed from sea surface height data. In section 3.3.1, we discuss the spatial distribution of AAIW and uLSW in our mean fields and in section 3.3.2 we investigate the processes leading to the erosion of AAIW. Our findings and their implications are summarized in section 3.4.

3.2 Observations and methods

3.2.1 Spray glider observations

In this analysis, we use observations of hydrography and water velocity that were collected between July 2015 and June 2020 using Spray autonomous underwater gliders (Sherman et al. 2001; Rudnick et al. 2016). Over the course of 31 missions, gliders have surveyed the Gulf Stream along the U.S. Eastern Seaboard as part of an ongoing sampling program since 2015 (details in Heiderich and Todd 2020; Todd 2021) and near Cape Hatteras, North Carolina as part of the "Processes Driving Exchange at Cape Hatteras" (PEACH) project during 2017–2019 (details in Todd 2020). All gliders were equipped with pumped Sea-Bird Scientific 41CP CTDs, returning 22,330 profiles of temperature and salinity. All gliders also carried 1-MHz Nortek acoustic Doppler dual current profilers (AD2CPs; Todd et al. 2017), which provide 20,525 profiles of absolute velocity. Observations used here have been gridded to uniform 10-m vertical resolution. For the Gulf Stream missions, most of the profiles either cover the upper 1000 m of the ocean or extend to within a few meters above the seafloor in shallower areas. For most PEACH missions, maximum profile depth was 500 m (Todd 2020).

3.2.2 Temporal averaging algorithm

In the analyses below, we consider both mean values and covariances (eddy fluxes) of properties observed by the gliders. To do so, we make use of the temporal averaging algorithm developed by Todd (2021) that produces temporal averages of observed quantities on a $0.1^\circ \times 0.1^\circ \times 10$-m grid (latitude × longitude × depth increment) that spans the Gulf Stream region along the U.S. East Coast. The reader is referred to Todd (2021) for full details, but, in brief, the averaging algorithm, denoted by $\langle\cdot\rangle$, determines the time-averaged value at a particular grid point via weighted least-squares fitting of a plane to observations at the depth of the grid point. The weight function is a two-dimensional Gaussian with anisotropic and inhomogeneous length scales to account for both the mean flow and variable sampling density. The same set of glider observations used in Todd (2021) are used here, so the parameters determining the weight function here are identical to those in Todd (2021). Deviations from mean quantities, denoted by $\cdot'$, are determined by interpolating the mean fields to the observation locations and differencing. Products of these deviations are then passed to the averaging algorithm to estimate covariances and eddy fluxes. For two missions, the loss of raw data for postprocessing leads to noisy velocity profiles which are only used to compute the mean velocity $\langle\mathbf{v}\rangle$, but not $\mathbf{v}'$. For illustrative purposes, we interpolate all of the three-dimensional mean fields (including products of deviations) to isopycnals of potential density at $\sigma_\theta = 0.025$ kg m^{-3} intervals and denote those fields as $\langle\cdot\rangle_\sigma$.

The temporal averaging algorithm computes a local average and is not designed to ensure volume conservation, which is needed to construct a control volume in section 3.3.2. Here, we give a brief summary of how we ensure volume conservation in the mean fields. For more details, see appendix 3.A. We assume that the mean fields describe an A-grid (Arakawa and Lamb 1977) in the horizontal: the quantities at four grid point corners enclose a grid cell. In the vertical, each grid cell has an extent of 10 m, with the observations centered in depth. In order to calculate the flux through a face, the quantities at the two grid points enclosing the face in this layer are averaged and multiplied with the area of the face and an outward pointing normal vector. Horizontal non-divergence in each grid cell is ensured by adjusting the mean velocities using least squares such that the net horizontal transport into each cell is zero. Adjustments are generally small (almost always less than 0.1 m s^{-1} and often even smaller, see Appendix 3.A). We ensure non-divergence only in the horizontal rather than in three dimensions since the time-mean Gulf Stream is in geostrophic balance to first order, and the mean flow should thus be horizontally nondivergent. Moreover, the glider observations do not provide usable estimates of the vertical velocity, so we cannot ensure three-dimensional non-divergence. Note that we cannot ensure volume conservation for fields that describe deviations from the mean (the $\cdot'$ fields).

3.2.3 Sea surface height (SSH) and the along-stream coordinate system

We use the gridded satellite-based sea surface height (SSH) products from the EU Copernicus Marine Environment Monitoring Service to create an along-stream coordinate system for the Gulf Stream that provides a continuous streamline along the entire U.S. East Coast. The daily delayed-time absolute dynamic topography products are used when available (until 7 March 2020) and near-real-time products otherwise. Analogous to Heiderich and Todd (2020), we choose the along-stream-coordinate to be distance along the time-mean 40-cm SSH contour during the time period of the glider observations (1 July 2015–30 June 2020) and choose 25°N as the origin of this along-stream coordinate system (dark gray line with dots in Fig. 3-1).

3.3 Results and discussion

3.3.1 Distributions of AAIW and uLSW

An example glider transect from May 2019 that cuts obliquely across the Florida Strait and continues eastward north of the Bahamas (red line in Fig. 3-2b,c) reveals two different water masses at intermediate depths on either side of the Bahamas (Fig. 3-2a): AAIW flows with the Gulf Stream through the Florida Strait and has much lower salinities (about 34.9) than the water to the east of the Little Bahama Bank, which has salinities near 35.3 in the same density range. These saltier waters further offshore include both uLSW and other slightly less dense intermediate waters (IW). The mean salinity field interpolated to the 27.25 kg m^{-3} isopycnal illustrates the strong along-isopycnal salinity gradient between AAIW in the Gulf Stream and uLSW on the southern Blake Plateau just offshore of the Gulf Stream (Fig. 3-2b). The low salinity signature of AAIW can be traced from the Florida Strait to approximately the location of the Charleston Bump. The signal fades farther north, as expected from the erosion of its distinct tail in the θ–S diagram (Fig. 3-1b). To better visualize

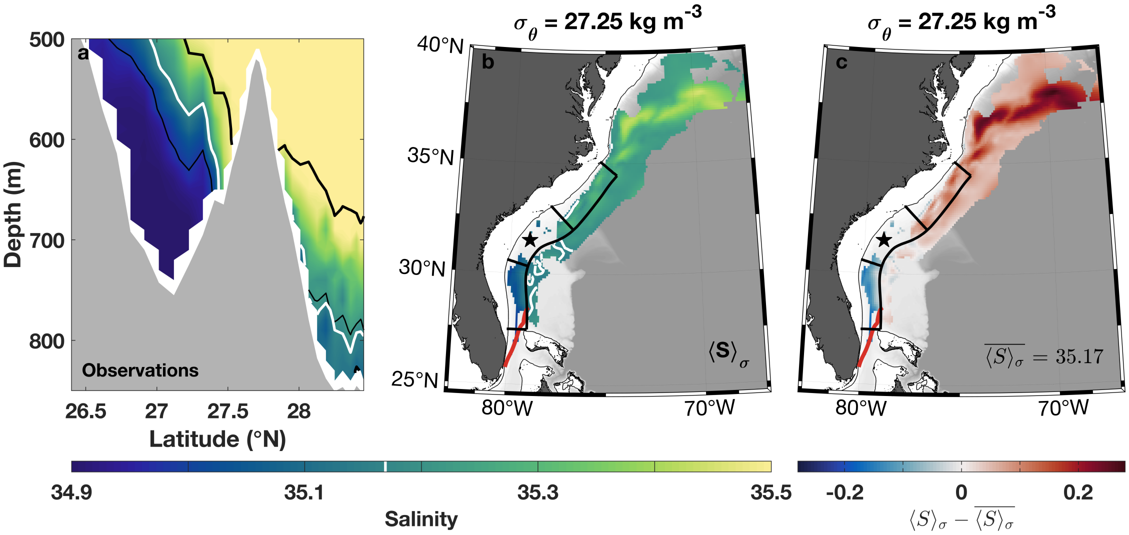

Figure 3-2: (a) Salinity observations below 500 m from a glider transect from May 2019 along the red line in panel (b). Waters with salinities above 35.5 all have the same yellow color. The thick black lines indicate the 27 and 27.5 kg m^{-3} isopycnals and the thin black line is the 27.25 kg m^{-3} isopycnal used in (b) and (c). The area-averaged salinity $\overline{\langle S \rangle_\sigma}$ (for the area of all three control volumes combined) on the 27.25 kg m^{-3} isopycnal is 35.17; it is shown as a white isohaline. (b) Map of salinity in the three-dimensional mean field interpolated to the 27.25 kg m^{-3} isopycnal ($\langle S_\sigma \rangle$). The 35.17 isohaline is white as in (a). (c) Along-isopycnal salinity difference on the 27.25 kg m^{-3} isopycnal (i.e., mean salinity on this isopycnal $\langle S \rangle_\sigma$ as in (b) minus area-averaged salinity in all three control volumes combined on this isopycnal ($\overline{\langle S \rangle_\sigma}$ = 35.17)). In (b) and (c), the thin and thick black lines and the star are as in Fig. 3-1(a).

this along-isopycnal salinity difference, we calculate area-averaged salinity on each isopycnal $\overline{\langle S\rangle_\sigma} = \sum A_{ij}\langle S\rangle_{\sigma,ij} / \sum A_{ij}$ (where A_{ij} is the horizontal area of each grid cell and i and j are latitude and longitude indices; shown as blue line in Fig. 3-3) and subtract it from the time-mean salinity on isopycnals $\langle S\rangle_\sigma$. Since uLSW is more frequently observed by the gliders (Fig. 3-3), it dominates the area-average. On the 27.25 kg m^{-3} isopycnal, area-averaged salinity $\overline{\langle S\rangle_\sigma}$ is 35.17 (white lines in Fig. 3-2a,b), closer to the typical salinity of uLSW. Consequently, AAIW is characterized by a negative isopycnal salinity anomaly ($\langle S\rangle_\sigma - \overline{\langle S\rangle_\sigma}$), while uLSW has a slightly positive anomaly.

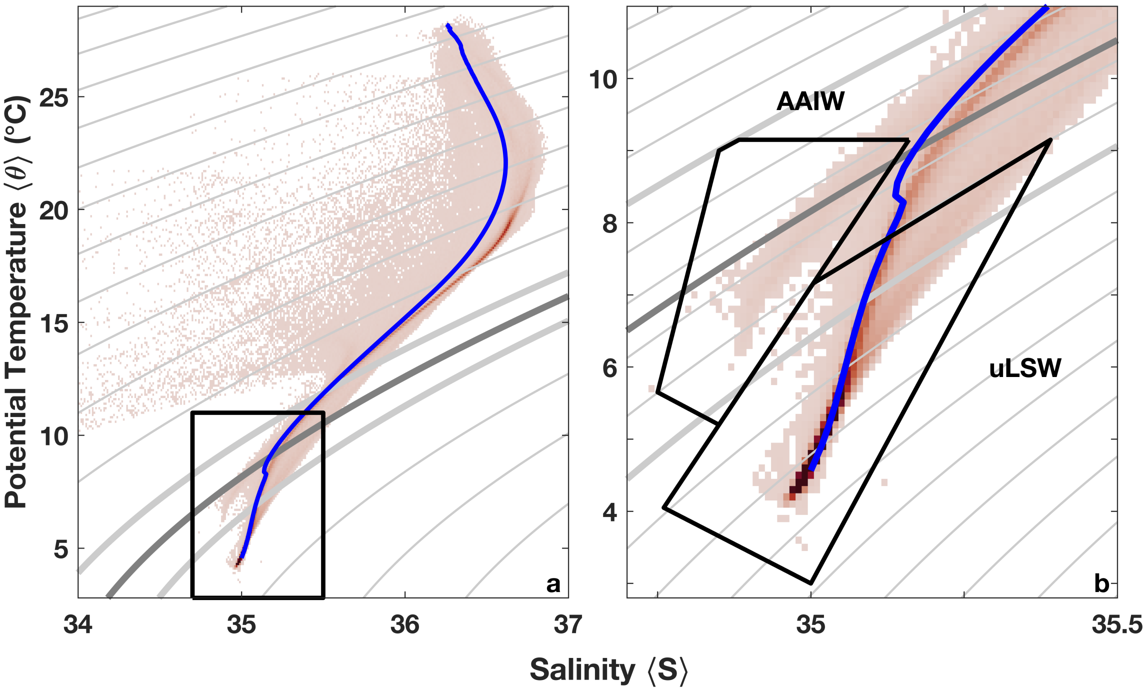

Figure 3-3: (a) Joint probability density function of potential temperature $\langle\theta\rangle$ and salinity $\langle S\rangle$ in the three-dimensional mean Gulf Stream fields. The blue line indicates the area-averaged salinity on each isopycnal $\overline{\langle S\rangle_\sigma}$. The gray lines are isopycnals with 0.5 kg m^{-3} spacing. Additionally, the $\sigma_\theta = 27$ and 27.5 kg m^{-3} contour lines are highlighted in bold, and the 27.25 kg m^{-3} isopycnal is indicated as a darker gray bold line. The black rectangle indicates the area that is shown in larger in panel (b). (b) The black outlines delineate Antarctic Intermediate Water (AAIW) and upper Labrador Sea Water (uLSW) as in Fig. 3-1. The isopycnal spacing is 0.1 kg m^{-3} and the same isopycnals are highlighted in bold as in panel (a).

3.3.2 Erosion of AAIW

3.3.2.1 A Reynolds-averaged advection-diffusion model

The AAIW signature fades as the Gulf Stream flows northward; this erosion in θ–S space suggests mixing with other water masses. The low salinity signature of AAIW can either be eroded through lateral stirring and subsequent mixing with the saltier water offshore (uLSW and the related, less dense IW) or through vertical mixing with shallower salty waters. Due to the shallow bathymetry of the Blake Plateau, mixing with denser salty waters below is only possible once the Gulf Stream reaches Cape Hatteras and thus not a major contributor to the observed erosion further upstream. To understand the processes contributing to the erosion and to investigate the relative importance of lateral and vertical mixing, we treat salinity as a tracer that evolves according to an advection-diffusion model. The advection-diffusion equation for a parcel of water with salinity S is given by:

$$\frac{\partial S}{\partial t} + \mathbf{v} \cdot \nabla S = \nabla \cdot (\kappa \nabla S). \tag{3.1}$$

Here, κ is a diffusivity representing unresolved processes that are treated as diffusive. κ is expected to vastly exceed the molecular diffusivity, which we neglect here. We partition the velocity $\mathbf{v}$ and salinity S into time-mean (denoted by $\langle \cdot \rangle$ and defined by the least squares averaging operation in Todd (2021)) and fluctuating (denoted by $\cdot'$ and calculated by subtracting the mean fields from the observations) components: $\mathbf{v} = \langle \mathbf{v} \rangle + \mathbf{v}'$ and $S = \langle S \rangle + S'$. Reynolds-averaging of Eq. (3.1) using the mean and turbulent components results in:

$$\underbrace{\langle \mathbf{v} \rangle \cdot \nabla \langle S \rangle}_{\text{① mean advection}} + \underbrace{\langle \mathbf{v}' \cdot \nabla S' \rangle}_{\text{② eddy advection}} = \underbrace{\nabla \cdot (\kappa \nabla \langle S \rangle)}_{\text{③ diffusion}}. \tag{3.2}$$

If we then consider Eq. (3.2) within a control volume, we can apply the divergence theorem to derive an equation for the net salt flux into the control volume, which must be zero in the time-mean. For the diffusion term ③, the divergence theorem in vector form gives us: $\iiint_V \nabla \cdot \kappa \nabla \langle S \rangle \, dV = \oiint_A \kappa \nabla \langle S \rangle \cdot \hat{\mathbf{n}} \, dA$. Additionally, we can use an identity of the divergence theorem for the advection terms. For the mean advection ①, we obtain $\iiint_V \langle \mathbf{v} \rangle \cdot \nabla \langle S \rangle \, dV = \oiint_A \langle \mathbf{v} \rangle \langle S \rangle \cdot \hat{\mathbf{n}} \, dA - \iiint_V \langle S \rangle \nabla \cdot \langle \mathbf{v} \rangle \, dV$. For a control volume that is fixed in time, we can interchange the order of integration and thus similarly write the eddy advection ② as $\iiint_V \langle \mathbf{v}' \cdot \nabla S' \rangle \, dV = \oiint_A \langle \mathbf{v}' S' \rangle \cdot \hat{\mathbf{n}} \, dA - \iiint_V \langle S' \nabla \cdot \mathbf{v}' \rangle \, dV$. Using the divergence theorem, rearranging, and assuming continuity so that the volume integral terms vanish, gives:

$$0 = - \underbrace{\oiint_A \langle \mathbf{v} \rangle \langle S \rangle \cdot \hat{\mathbf{n}} \, dA}_{\text{① mean advective flux divergence}} - \underbrace{\oiint_A \langle \mathbf{v}' S' \rangle \cdot \hat{\mathbf{n}} \, dA}_{\text{② eddy advective flux divergence}} + \underbrace{\oiint_A \kappa \nabla \langle S \rangle \cdot \hat{\mathbf{n}} \, dA.}_{\text{③ diffusive flux divergence}} \tag{3.3}$$

In our definition, the normal vectors $\hat{\mathbf{n}}$ point out of the control volume. For a control volume with faces oriented either purely horizontally or purely vertically, we can split Eq. (3.3) into horizontal and vertical components as:

$$\begin{aligned} 0 = & - \underbrace{\iint_{A_L} \langle \mathbf{v}_H \rangle \langle S \rangle \cdot \hat{\mathbf{n}}_H \, dA_L}_{\text{(1a) lateral mean advective flux divergence}} - \underbrace{\iint_{A_H} \langle w \rangle \langle S \rangle \cdot \hat{\mathbf{n}}_V \, dA_H}_{\text{(1b) vertical mean advective flux divergence}} \\ & - \underbrace{\iint_{A_L} \langle \mathbf{v}_H{}' S' \rangle \cdot \hat{\mathbf{n}}_H \, dA_L}_{\text{(2a) lateral eddy advective flux divergence}} - \underbrace{\iint_{A_H} \langle w' S' \rangle \cdot \hat{\mathbf{n}}_V \, dA_H}_{\text{(2b) vertical eddy advective flux divergence}} \\ & + \underbrace{\iint_{A_L} \kappa_H \nabla_H \langle S \rangle \cdot \hat{\mathbf{n}}_H \, dA_L}_{\text{(3a) lateral diffusive flux divergence}} + \underbrace{\iint_{A_H} \kappa_V \frac{\partial \langle S \rangle}{\partial z} \cdot \hat{\mathbf{n}}_V \, dA_H.}_{\text{(3b) vertical diffusive flux divergence}} \end{aligned} \tag{3.4}$$

Horizontal faces (i.e., top and bottom) are denoted as A_H. The lateral faces (i.e., east, west, south, north) are denoted as A_L and have a vertical orientation. We consider vertical and horizontal fluxes rather than isopycnal and diapycnal fluxes because the glider observations only provide estimates of the horizontal velocity components $\mathbf{v}_H$. Therefore, we can only estimate some of the fluxes. If we assume that the mean vertical velocity $\langle w \rangle$ is small, then (1b) vanishes. Vertical velocity fluctuations w' may be larger, especially in the area of the Charleston Bump where large internal wave activity has been observed (see Todd 2017). Since we lack usable estimates of w', we assume that all vertical eddy advective fluxes (2b) can be parameterized as downgradient diffusion in the form of (3b), thereby treating κ_V as a vertical eddy diffusivity that applies over all applicable vertical and temporal scales and eliminating (2b) from further consideration. Since we directly evaluate lateral eddy fluxes through the Reynolds decomposition, the lateral diffusive flux (3a) is due only to unresolved processes and is assumed to be negligibly small. We are left with three terms that we can evaluate using the glider observations ((1a), (2a), and (3b) to within the unknown κ):

$$0 = -\underbrace{\iint_{A_L} \langle \mathbf{v}_H \rangle \langle S \rangle \cdot \hat{\mathbf{n}}_H \, dA_L}_{\text{(1a) lateral mean advective flux divergence}} - \underbrace{\iint_{A_L} \langle \mathbf{v}_H{}' S' \rangle \cdot \hat{\mathbf{n}}_H \, dA_L}_{\text{(2a) lateral eddy advective flux divergence}} + \underbrace{\iint_{A_H} \kappa_V \frac{\partial \langle S \rangle}{\partial z} \cdot \hat{\mathbf{n}}_V \, dA_H}_{\text{(3b) vertical diffusive flux divergence}}. \tag{3.5}$$

By applying the temporal averaging algorithm to the glider observations, we obtain both the mean and fluctuating components of velocity and salinity, so that we can estimate the lateral mean and eddy advection through the sides of a control volume [terms (1a) and (2a) in Eq. (3.5)]. Furthermore, we can construct the vertical mean salinity gradient $\frac{\partial \langle S \rangle}{\partial z}$ at the top and bottom of a control volume [part of the vertical diffusion term (3b) in Eq. (3.5)]. If the terms that we cannot evaluate really are negligible, one could back out the vertical diffusivity κ_V.

3.3.2.2 Construction of control volumes

We construct a set of control volumes consisting of whole grid cells, meaning that the lateral faces are all vertically oriented (i.e., east, west, north, south) and the top and bottom faces are purely horizontal (Fig. 3-4). Whole grid cells are needed to compute fluxes because this is how volume is conserved in our three-dimensional mean fields (see section 3.2.2). Included grid cells are chosen to most closely follow

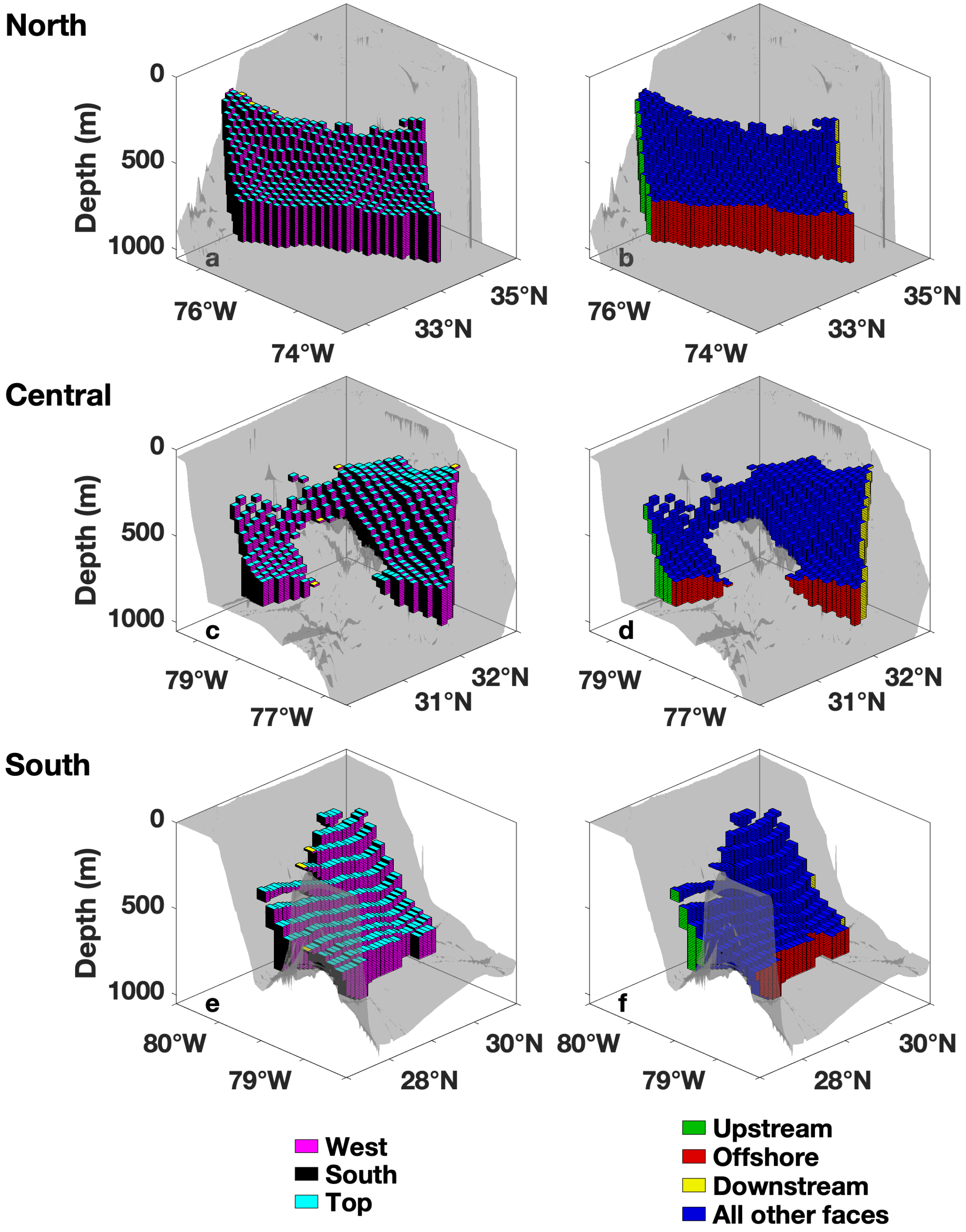

Figure 3-4: Three-dimensional views of the three control volumes: (a–b) the northern control volume, (c–d) the central control volume, and (e–f) the southern control volume. The transparent gray shading indicates the bathymetry in the region. In (a,c,e), the faces are colored based on their geographic orientation, and in (b,d,f) the upstream, downstream, and offshore faces are highlighted (see legend).

a nominal smooth control volume defined by isopycnals of mean potential density σ_θ (bold isopycnals in Figs. 3-1b–c and 3-2a) and along-stream and cross-stream distances in the SSH-based coordinate system (black lines in Fig. 3-1a). Additionally, grid cells are only considered when they have good data at all four corners in a depth layer. Our control volumes enclose the AAIW in the Gulf Stream south of Cape Hatteras. We use the $\sigma_\theta = 27$ kg m^{-3} and $\sigma_\theta = 27.5$ kg m^{-3} isopycnals to define the top and bottom faces of our control volumes, respectively, because they bound both AAIW and uLSW. In the Gulf Stream upstream (southwest) of Cape Hatteras, the top isopycnal shoals to about 160 m along the inshore edge, but 75 km offshore of the 40-cm SSH contour it can reach depths of about 740 m. Over the same region, the bottom isopycnal deepens from about 460 m to about 980 m in the offshore direction.

We define three control volumes along the mean path of the Gulf Stream (black outlines in Fig. 3-1) that describe dynamically different regions. For all three control volumes, the offshore boundary is 75 km from the 40-cm SSH contour (dark gray line with dots in Fig. 3-1) and the inshore boundary is defined by the region where the mean is well-estimated based on the metrics in Todd (2021). Each volume extends for 340 km along the 40-cm SSH contour. The southern control volume captures the region just north of the Florida Strait, where the Gulf Stream is still a relatively straight jet. The upstream boundary of this control volume is defined as an along-stream distance of 280 km and the downstream boundary at an along-stream distance of 620 km. The central control volume encloses the area of the Charleston Bump (along-stream distances of 620 to 920 km), where internal lee waves and near-bottom mixing are particularly strong (Todd 2017). In the chosen density range, the Charleston Bump represents a major barrier that nearly divides the control volume into distinct volumes (Fig. 3-4c,d). The northern control volume covers the remaining area just south of Cape Hatteras (along-stream distances of 960 to 1300 km).

We identify the upstream, downstream, and offshore boundaries of each control volume (Fig. 3-4b,d,f) by tracing the outside grid points of the grid cell columns that have data anywhere in the vertical. The grid points closest to the corners of the nominal control volumes mark the transitions between the upstream, offshore, downstream, and inshore boundaries. Faces at all depth that fall onto this outline are considered part of the respective boundaries, which closely resemble the nominal boundaries in Fig. 3-1, except where the seafloor intersects with the nominal boundary (in particular around the Bahamas and on the inshore boundary). This definition allows us to examine the fluxes through the outermost faces, excluding any flow coming in through the faces that are following the top and bottom isopycnals.

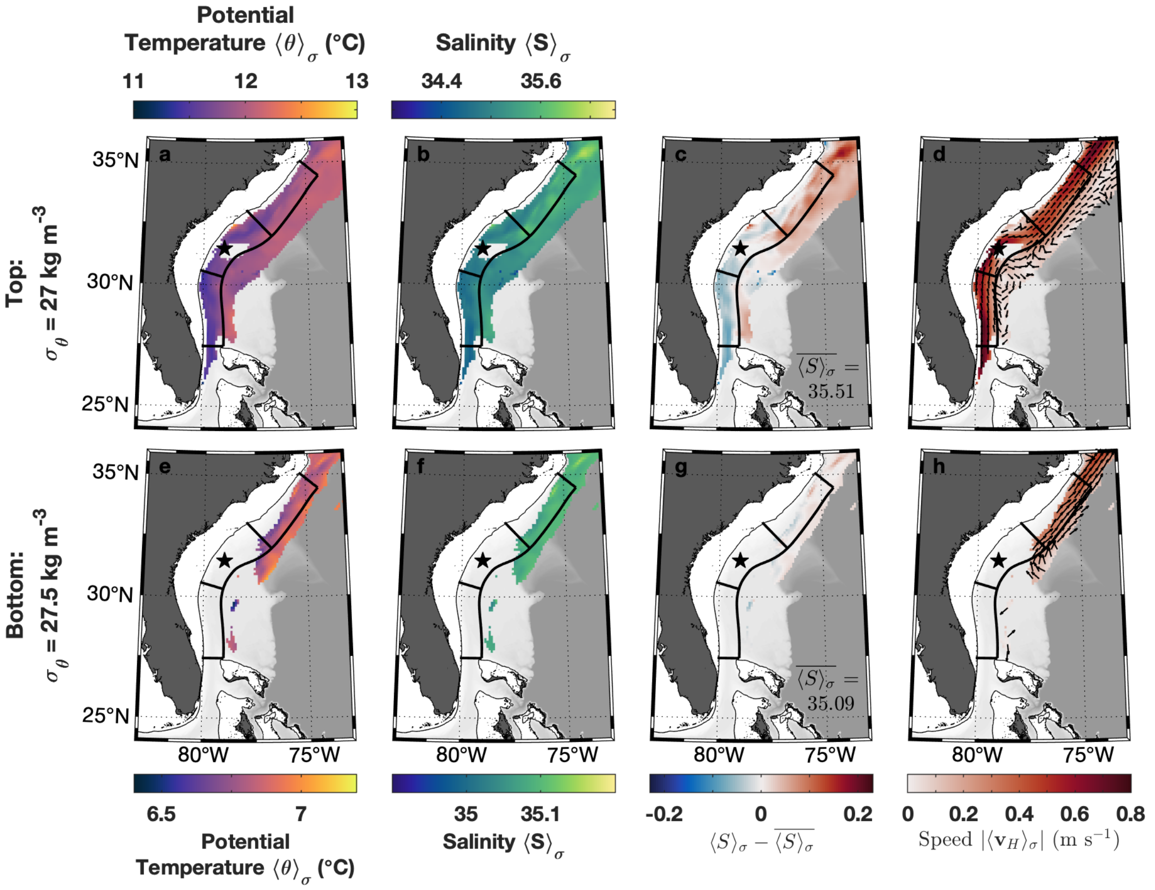

Figure 3-5: Maps of different properties in the three-dimensional mean fields interpolated to the (top row) top isopycnal ($\sigma_\theta = 27.0$ kg m^{-3}) and (bottom row) bottom isopycnal of the control volumes ($\sigma_\theta = 27.5$ kg m^{-3}): (a,e) Potential temperature $\langle\theta\rangle_\sigma$, (b,f) salinity $\langle S\rangle_\sigma$, (c,g) along-isopycnal salinity difference (i.e., mean salinity on this isopycnal $\langle S\rangle_\sigma$ as in (b,f) minus area-averaged salinity on this isopycnal ($\overline{\langle S\rangle_\sigma}$; value given in the bottom right corner of the panel) and (d,h) horizontal water velocity $\langle\mathbf{v}_H\rangle_\sigma$ with the color indicating the speed and black arrows the direction. In all panels, the thin and thick black lines and the star are as in Fig. 3-1a.

3.3.2.3 Properties on the periphery of the control volumes

Mean properties interpolated to the nominal smooth isopycnal and lateral boundaries of the control volumes provide a clean representation of the water types entering the control volume. The distributions of mean properties interpolated to the two isopycnals defining the top and bottom of the control volume (27 kg m^{-3} and 27.5 kg m^{-3}) show that our choice of control volume encloses AAIW entirely. The lateral temperature and salinity differences are quite small on the top isopycnal (Fig. 3-5a,b), especially compared to the salinity difference along the 27.25 kg m^{-3} isopycnal (Fig. 3-3 and Fig. 3-2b,c). Thus, we mostly see what Heiderich and Todd (2020) classified as more indistint intermediate waters (IW) on the top isopycnal. However, when plotting the isopycnal salinity anomaly $\langle S\rangle_\sigma - \overline{\langle S\rangle_\sigma}$ as in Fig. 3-2c, the fresher AAIW tongue still appears as a negative signal at the very top of the control volume (Fig. 3-5c), while saltier waters appear offshore and downstream of the Charleston Bump. Previous studies have shown that the Gulf Stream reaches the bottom over the Blake Plateau (Pratt 1963; Todd 2017). Similarly, we observe Gulf Stream velocities exceeding 0.7 m s^{-1} at the depths of our control volumes (Fig. 3-5d). Velocities outside of the control volumes where uLSW is found are much smaller and the flow direction deviates from the main Gulf Stream path. Just north of the Bahamas, a westward mean flow joins the Gulf Stream, a first indication that uLSW may be entrained in this region as expected based on the analysis of Heiderich and Todd (2020). South of the Charleston Bump, the bottom isopycnal face of the control volumes intersects the bathymetry; only the deeper-reaching uLSW can be detected outside of the Gulf Stream (Fig. 3-5e–h). Properties interpolated to the centroid of the top and bottom faces of the actual control volumes are very similar in most places, except where the bottom isopycnal intersects the bathymetry and the bottom faces are therefore at lower densities (not shown).

Mean potential temperature $\langle\theta\rangle$ and mean salinity $\langle S\rangle$ along the lateral faces of the control volumes show typical Gulf Stream features, including a subsurface salinity maximum (Fig. 3-6a–f). Since our normal vectors point outward from the control

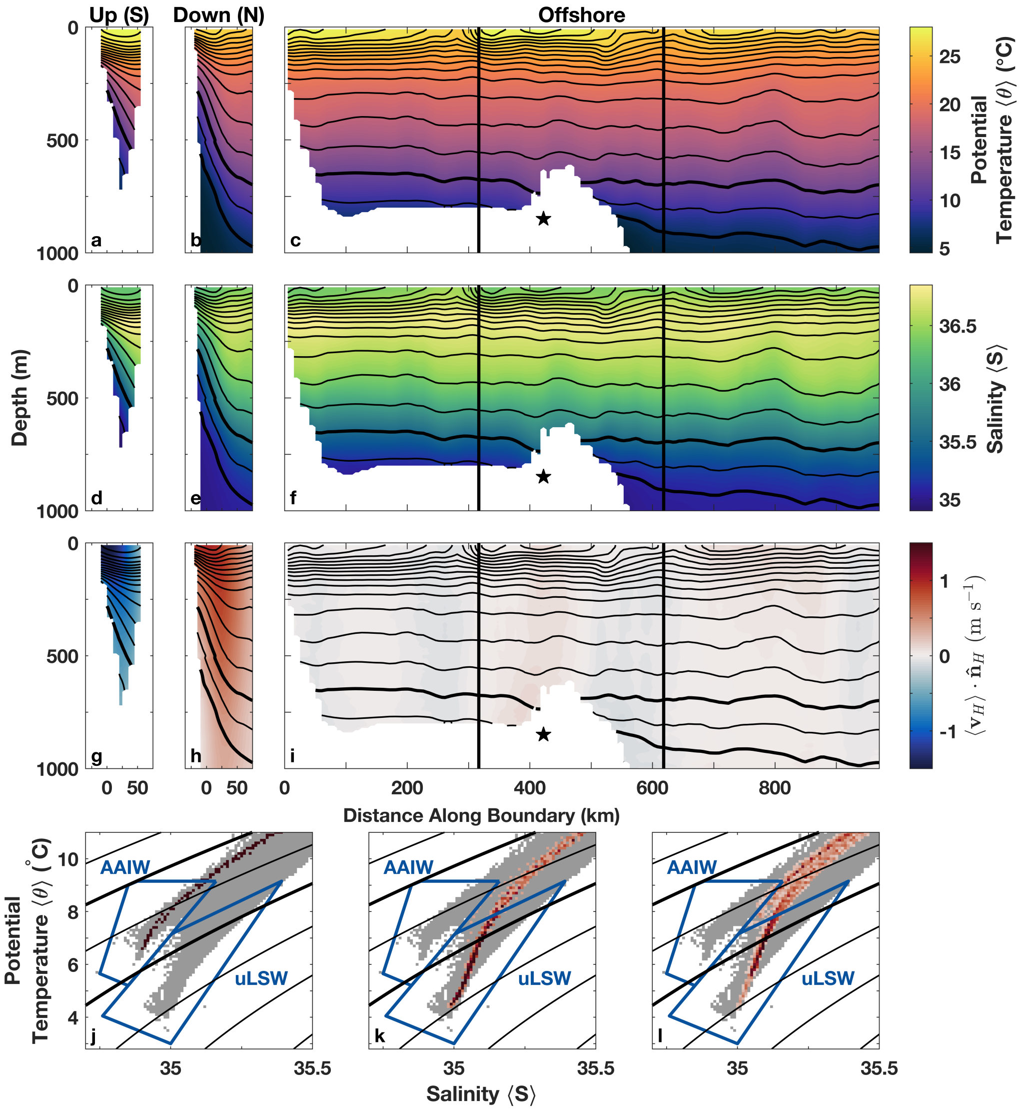

Figure 3-6: Several properties of the three-dimensional mean fields interpolated to the nominal smooth lateral boundaries of different control volumes: the upstream boundary of the southern control volume (left column), the downstream boundary of the northern control volume (middle column), and the offshore boundaries of all three control volumes (right column). The vertical black lines for the offshore boundary delineate the three different control volumes (from south, to central, to north with increasing distance along the boundary) and the black star indicates the Charleston Bump. (a–c) Potential temperature $\langle \theta \rangle$, (d–f) salinity $\langle S \rangle$, and (g–i) water velocity $\langle \mathbf{v}_H \rangle$ normal to the lateral boundaries. (j–l) Joint probability density functions of potential temperature $\langle \theta \rangle$ and salinity $\langle S \rangle$ of the water properties along the three lateral boundaries, similar to Fig. 3-3. The blue outlines delineate Antarctic Intermediate Water (AAIW) and upper Labrador Sea Water (uLSW) as in Fig. 3-1. In all panels, thin black lines indicate isopycnals with 0.5 kg m^{-3} spacing with the top and bottom isopycnals of the control volumes ($\sigma_\theta = 27$ and 27.5 kg m^{-3}) highlighted in bold.

volume, the flow normal to the upstream side of the control volumes is negative (water is flowing northward or into the control volume) and the flow on the downstream side is positive (flowing out of the control volume). The upstream boundary for the southern control volume and the downstream boundary of the northern control volume are shown as examples in Fig. 3-6g,h. Since the nominal smooth offshore boundaries of the control volumes are approximately parallel to the axis of the Gulf Stream, the mean flow through them is generally weak (Fig. 3-6i). In the mean, water is slowly flowing out of the control volume around the Charleston Bump area and just south of Cape Hatteras and into the control volume everywhere else, again suggesting that uLSW enters the Gulf Stream just north of the Bahamas. Joint probability density functions of potential temperature $\langle\theta\rangle$ and salinity $\langle S\rangle$ along the lateral boundaries of our control volumes show that our choice of the control volume clearly separates the two water masses; the AAIW tail is apparent on the upstream side, but the offshore and downstream sides are dominated by uLSW and the related IW (Fig. 3-6j–l). Thus, water entering through the offshore side may be a combination of uLSW and IW that then mixes with AAIW and leads to its erosion.

3.3.2.4 Fluxes into and out of the control volumes

Evaluating terms (1a) and (2a) in Eq. (3.5) allows us to consider whether lateral or vertical mixing dominates the erosion of AAIW. If lateral eddy stirring between AAIW and saltier uLSW offshore dominated the erosion of AAIW, then the lateral mean salt advection (1a) would be balanced by the lateral eddy salt advection (2a). If these two terms do not balance, vertical processes must be important. The totals of the lateral flux terms integrated over the entirety of each control volume are listed in Table 3.1 and shown schematically in Fig. 3-7. We compute both the net lateral flux into/out of the control volumes and the fluxes through the upstream, downstream, and offshore boundaries as defined in Fig. 3-4b,d,f. The areas corresponding to the different boundaries and the volume transport through them are also given in Table 3.1. As for the properties in section 3.3.2.3, lateral fluxes are interpolated to the nominal smooth lateral boundaries for illustration purposes only (Fig. 3-8). Note that Fig. 3-

Table 3.1: Lateral fluxes and related properties corresponding to the faces of the southern, central, and northern control volumes. The reader is referred to the text for explanations of the various terms shown. The fluxes through the upstream, downstream, and offshore boundaries do not add up to the net, so the residual (i.e. fluxes through inshore faces and faces following the top and bottom isopycnals) is given in the right column. † The net transport into each control volume is zero to numerical precision by construction.

	Net	**Upstream**	**Downstream**	**Offshore**	**Residual**
Southern control volume ($S_0 = 35.20$)					
Area (m^2)	4×10^8	6×10^6	2×10^7	5×10^7	3×10^8
Transport (m^3 s^{-1})	– †	-3×10^6	5×10^6	-1×10^6	-7×10^5
$\iint_{A_L} \langle \mathbf{v}_H \rangle \langle S \rangle \cdot \hat{\mathbf{n}}_H \, dA_L$ (m^3 psu s^{-1})	-2×10^4	-1×10^8	2×10^8	-4×10^7	-2×10^7
$\iint_{A_L} \langle \mathbf{v}_H \rangle \langle S - S_0 \rangle \cdot \hat{\mathbf{n}}_H \, dA_L$ (m^3 psu s^{-1})	-2×10^4	-3×10^4	2×10^5	-1×10^5	-5×10^4
$\iint_{A_L} \langle \mathbf{v}_H{}' S' \rangle \cdot \hat{\mathbf{n}}_H \, dA_L$ (m^3 psu s^{-1})	-5×10^5	-1×10^4	-2×10^3	-7×10^4	-4×10^5
$\iint_{A_L} \nabla_H \langle S \rangle \cdot \hat{\mathbf{n}}_H \, dA_L$ (psu m)	5×10^1	-4×10^0	-2×10^0	2×10^2	-1×10^2
κ_H^* (m^2 s^{-1})		-4×10^3	-1×10^3	4×10^2	
Central control volume ($S_0 = 35.31$)					
Area (m^2)	4×10^8	2×10^7	3×10^7	4×10^7	3×10^8
Transport (m^3 s^{-1})	– †	-4×10^6	7×10^6	-5×10^5	-2×10^6
$\iint_{A_L} \langle \mathbf{v}_H \rangle \langle S \rangle \cdot \hat{\mathbf{n}}_H \, dA_L$ (m^3 psu s^{-1})	5×10^5	-2×10^8	2×10^8	-2×10^7	-6×10^7
$\iint_{A_L} \langle \mathbf{v}_H \rangle \langle S - S_0 \rangle \cdot \hat{\mathbf{n}}_H \, dA_L$ (m^3 psu s^{-1})	5×10^5	2×10^5	3×10^4	-4×10^2	3×10^5
$\iint_{A_L} \langle \mathbf{v}_H{}' S' \rangle \cdot \hat{\mathbf{n}}_H \, dA_L$ (m^3 psu s^{-1})	9×10^5	-5×10^3	-2×10^5	5×10^4	1×10^6
$\iint_{A_L} \nabla_H \langle S \rangle \cdot \hat{\mathbf{n}}_H \, dA_L$ (psu m)	6×10^2	-2×10^1	-3×10^0	1×10^2	5×10^2
κ_H^* (m^2 s^{-1})		-3×10^2	-6×10^4	-4×10^2	
Northern control volume ($S_0 = 35.28$)					
Area (m^2)	6×10^8	3×10^7	3×10^7	1×10^8	5×10^8
Transport (m^3 s^{-1})	– †	-7×10^6	9×10^6	5×10^5	-2×10^6
$\iint_{A_L} \langle \mathbf{v}_H \rangle \langle S \rangle \cdot \hat{\mathbf{n}}_H \, dA_L$ (m^3 psu s^{-1})	2×10^6	-2×10^8	3×10^8	2×10^7	-8×10^7
$\iint_{A_L} \langle \mathbf{v}_H \rangle \langle S - S_0 \rangle \cdot \hat{\mathbf{n}}_H \, dA_L$ (m^3 psu s^{-1})	2×10^6	-3×10^5	5×10^4	2×10^4	3×10^6
$\iint_{A_L} \langle \mathbf{v}_H{}' S' \rangle \cdot \hat{\mathbf{n}}_H \, dA_L$ (m^3 psu s^{-1})	9×10^5	3×10^5	-3×10^4	-5×10^4	7×10^5
$\iint_{A_L} \nabla_H \langle S \rangle \cdot \hat{\mathbf{n}}_H \, dA_L$ (psu m)	9×10^2	2×10^1	2×10^1	3×10^2	5×10^2
κ_H^* (m^2 s^{-1})		-2×10^4	2×10^3	1×10^2	

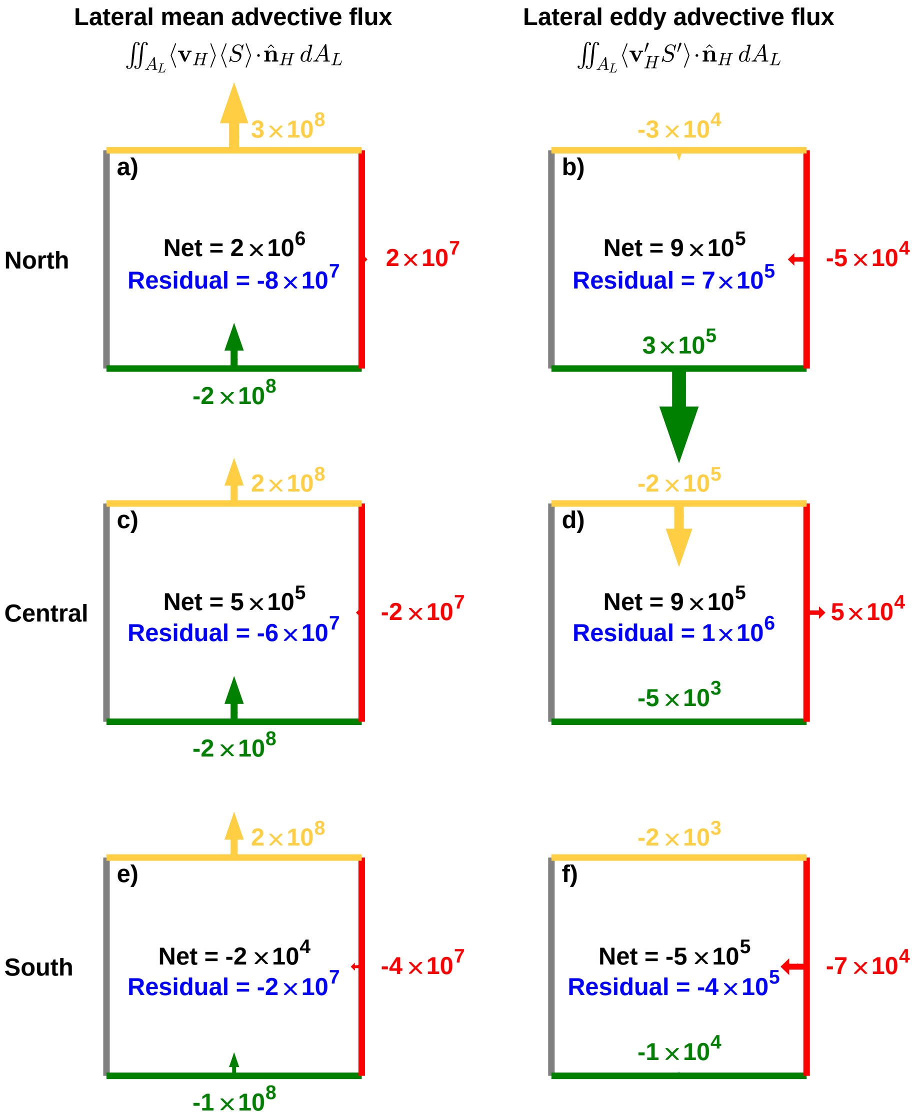

Figure 3-7: Simplified schematic showing the lateral fluxes into/out of the three control volumes: the southern control volume (left column), the central volume (middle column), and the northern control volume (right column). (a–c) Lateral mean advective flux $\iint_{A_L} \langle \mathbf{v}_H \rangle \langle S \rangle \cdot \hat{\mathbf{n}}_H \, dA_L$ (all numbers in m^3 psu s^{-1}), and (d–f) lateral eddy advective flux $\iint_{A_L} \langle \mathbf{v}'_H S' \rangle \cdot \hat{\mathbf{n}}_H \, dA_L$ (all numbers in m^3 psu s^{-1}). The net lateral fluxes integrated around all lateral faces are shown in black in the centers of the control volumes. The colors are as in Fig. 3-4b,d,f: the fluxes through the upstream boundaries are shown in green, the downstream boundaries/fluxes in yellow, the offshore boundaries/fluxes in red, and the residual fluxes through the remaining lateral faces are blue. The arrows show whether a flux is into or out of a control volume (i.e., negative or positive, respectively) and its relative size compared to the other fluxes. The scale for the arrows is the same for (a–c). (d–f) uses a different scale for the arrows, since the fluxes are smaller. In some cases, the fluxes are so small that the arrows are not visible.

8 does not show the fluxes that are integrated to arrive at the values in Table 3.1 and Fig. 3-7. Instead, fluxes are integrated over the lateral faces shown in Fig. 3-4 to ensure non-divergence by incorporating whole grid cells; these fluxes are more difficult to display because the direction of the normal vectors frequently changes along the boundary because the faces are purely east-west/north-south oriented. Since the totals also include fluxes through the inshore boundary of the control volumes (which are assumed small due to proximity to bathymetry) and any lateral faces along the top and bottom isopycnal-following boundaries or the bottom where the bathymetry is shallower than the bottom isopycnal (lateral blue faces in Figure 3-4b,d,f), the residuals are relatively large (Table 3.1). Table 3.1 lists all values for completeness, but the following discussion focuses on key values with clear interpretations.

Negative values of $\iint_{A_L} \langle \mathbf{v}_H \rangle \langle S \rangle \cdot \hat{\mathbf{n}}_H \, dA_L$ [term Ⓐ1a in Eq. (3.5)] indicate that the mean flow fluxes salt into the control volumes since the normal vectors point out of the control volumes (indicated in blue in Fig. 3-8), whereas positive values imply that salt is fluxed out (red in Fig. 3-8). The southernmost control volume is gaining a small amount of salt due to the mean flow, whereas the other two are both losing salt (Fig. 3-7a–c). The net lateral mean advective salt flux $\iint_{A_L} \langle \mathbf{v}_H \rangle \langle S \rangle \cdot \hat{\mathbf{n}}_H \, dA_L$ is smaller than the lateral mean advective salt flux through the individual boundaries by at least an order of magnitude for all the different control volumes because the terms are dominated by the velocity field (e.g., the panels a,d,e in Fig. 3-8 strongly resemble Fig. 3-6g–i between the thick black isopycnals). Consequently, $\langle \mathbf{v}_H \rangle \langle S \rangle \cdot \hat{\mathbf{n}}_H$ through the upstream and downstream boundaries of each control volume is much larger than for the corresponding offshore boundaries (Fig. 3-7a–c) due to the Gulf Stream-following control volume. As already expected from the mean velocity field (Fig. 3-6i), the mean flow fluxes salt into the control volumes through the offshore boundary in several locations, though those fluxes are small (Fig. 3-8e). Most notable is the influx of salt along the entire offshore side of the southern control volume (also see Fig. 3-7a), indicating that upper Labrador Sea Water is entrained into the Gulf Stream north of the Bahamas. The residual mean advective fluxes are of comparable magnitude to the fluxes through the upstream/downstream/offshore sides, indicating

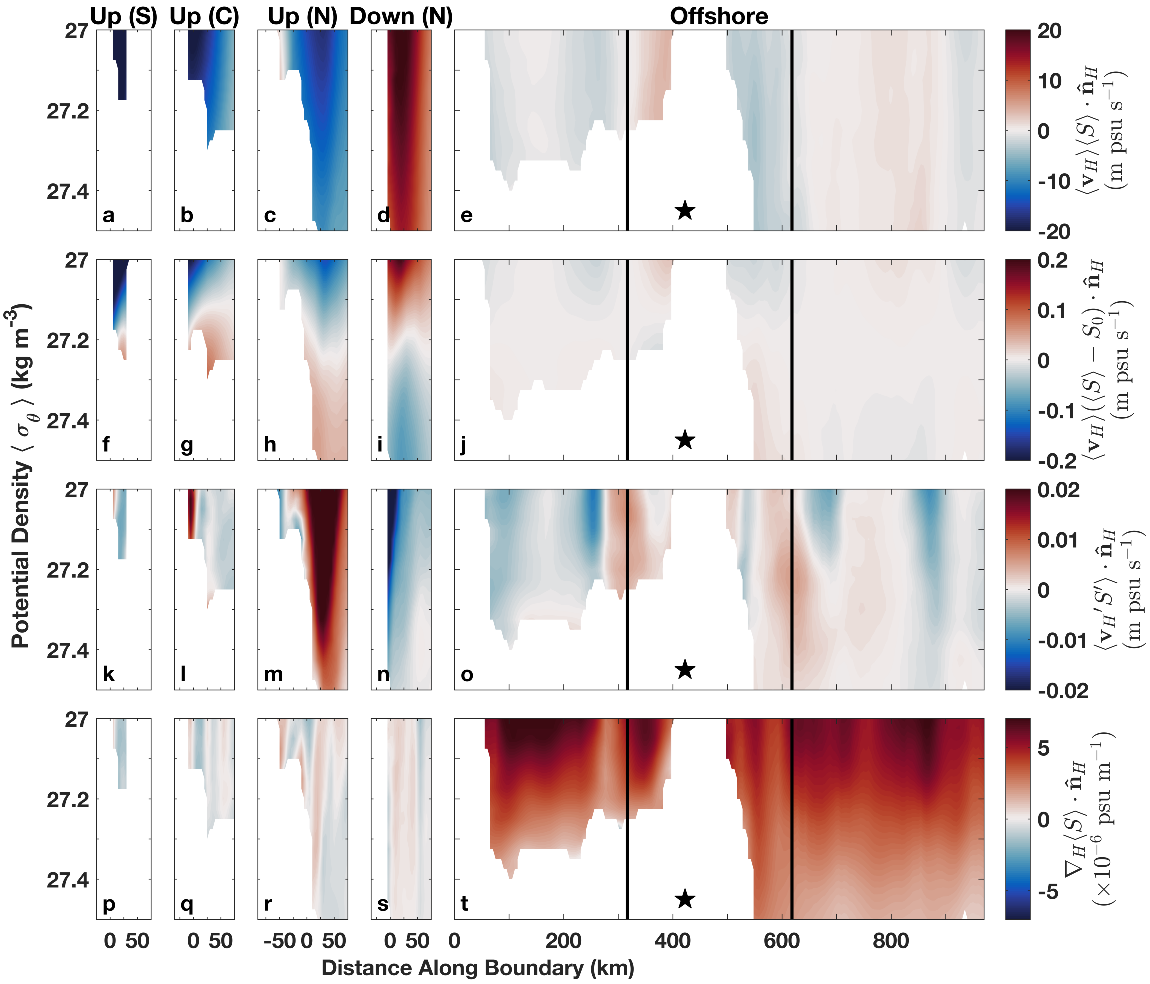

Figure 3-8: Fluxes and related properties interpolated to the nominal smooth lateral boundaries of different control volumes: the upstream boundary of the southern control volume (a,f,k,p), the upstream boundary of the central control volume (b,g,l,q), the upstream boundary of the northern control volume (c,h,m,r), the downstream boundary of the northern control volume (d,i,n,s), and the offshore boundaries of all three control volumes (e,j,o,t). The vertical black lines for the offshore boundary delineate the three different control volumes (from south, to central, to north with increasing distance along the boundary) and the black star indicates the Charleston Bump as in Fig. 3-6. All fluxes are normal to the respective boundaries, with the normal vectors pointing out of the control volumes. In all panels, the vertical coordinate is potential density σ_θ and the fluxes are only shown between the top and bottom isopycnals of the control volumes ($\sigma_\theta = 27$ and 27.5 kg m^{-3}). (a–e) Lateral mean advective flux $\langle \mathbf{v}_H \rangle \langle S \rangle \cdot \hat{\mathbf{n}}_H$, (f–j) lateral mean advective flux after subtracting a constant salinity S_0 that is the volume average in the respective control volume ($\langle \mathbf{v}_H \rangle (\langle S \rangle - S_0) \cdot \hat{\mathbf{n}}_H$), (k–o), lateral eddy advective flux $\langle \mathbf{v}'_H S' \rangle \cdot \hat{\mathbf{n}}_H$, and (p–t) the horizontal salinity gradient ($\nabla_H \langle S \rangle \cdot \hat{\mathbf{n}}_H$).

that the fluxes through the lateral faces tracing the top and bottom isopycnals, inshore side and/or bottom (where the bottom isopycnal intersects with the bathymetry) are not negligible.

To highlight the relative salinity of water flowing through each boundary and reduce the impact of the mean flow, we subtract the volume-averaged salinity in each control volume ($S_0 = \sum V_{ijk} S_{ijk} / \sum V_{ijk}$ where V is the volume and ijk are the latitude/longitude/depth indices of the grid cells that are considered to be inside of the respective control volume; see Table 3.1 for values) from the time-mean salinity $\langle S \rangle$. S_0 is lowest (35.20) in the southern control volume, and highest (35.31) in the central control volume, which has the highest proportion of shallower, inshore grid cells with higher salinities due to its shape around the Charleston Bump. Subtracting a constant volume-averaged salinity does not change the net salt flux since volume is conserved. Positive values of $\iint_{A_L} \langle \mathbf{v}_H \rangle \left(\langle S \rangle - S_0 \right) \cdot \hat{\mathbf{n}}_H \, dA_L$ indicate that the mean flow brings in waters that are fresher than the volume-average or removes waters that are saltier (red in Fig. 3-8f–j). Negative values indicate that the mean flow introduces saltier than average waters into the control volume or transports fresher waters out (blue in Fig. 3-8f–j). In the southern control volume, there is saltier than average water going out through the downstream end, nearly balancing the saltier than average water coming in through the offshore side (both are $\mathcal{O}(10^5)$ m^3 psu s^{-1}). There is however a small ($\mathcal{O}(10^4)$ m^3 psu s^{-1}) flux relative to the mean salinity through the upstream faces. We know that the AAIW coming in through the upstream end is characterized by its low salinity signature, yet the vertical salinity structure dominates when a volume-averaged salinity is subtracted (Fig. 3-8f–j). Thus, we only see less salty than average water entering the control volume in the densest layers at the bottom of the upstream end of the southern control volume (Fig. 3-8f), leading to a small negative flux when integrated along the whole upstream boundary. At the upstream and downstream boundaries of all three control volumes, the deeper waters are less salty than the volume average for the respective control volume (Fig. 3-8f–i), even at the downstream boundary of the northern control volume (Fig. 3-8i). Note the opposite signs compared to the upstream boundaries (Fig. 3-8f–h) due to the opposite direction of the normal vector. We do not show the downstream boundaries for the southern and central control volumes because they are very similar to the upstream boundaries of the central and northern control volumes, respectively. The main differences are oppositely directed normal vectors and that they are referenced to a slightly different volume-averaged salinity because they belong to different control volumes.

The imbalance in the lateral mean advective flux (as is the case for all three control volumes) must be balanced by the other terms, either the lateral eddy advection (2a) or the vertical diffusion (3b) (or noise/error in our estimates, see section 3.3.2.6). If lateral mixing dominated the erosion of AAIW, then the imbalance in the lateral mean salt advection would be balanced by the lateral eddy salt advection $\iint_{A_L} \langle \mathbf{v}_H{}' S' \rangle \cdot \hat{\mathbf{n}}_H \, dA_L$. The net lateral eddy salt fluxes for each of the three control volumes (Fig. 3-7d–e) are of the same sign and of comparable magnitude to the net lateral mean advective fluxes and thus do not balance them. Due to the outward pointing normal vectors, positive values of $\iint_{A_L} \langle \mathbf{v}_H{}' S' \rangle \cdot \hat{\mathbf{n}}_H \, dA_L$ indicate that the fluctuating flow removes salt from the control volume, either by bringing in fresher than average waters or by removing saltier water. In contrast, negative values imply that the fluctuating flow brings salt into the control volume, either by bringing in saltier waters or by removing fresher waters. The net effect of the eddies is a salt flux into the southern control volume, and out of the central and northern control volumes (Fig. 3-7d–f).

As for the mean advective flux, the eddy advective flux $\iint_{A_L} \langle \mathbf{v}_H{}' S' \rangle \cdot \hat{\mathbf{n}}_H \, dA_L$ is negative on the offshore side of the southern control volume (Fig. 3-8o and Fig. 3-7a) and thus has a sign consistent with a variable current bringing saltier water (i.e., uLSW and related waters) into the control volume. Time varying flow is a potential mechanism that can enable uLSW to cross isobaths in order to reach the southern Blake Plateau and become entrained into the Gulf Stream. This variable current north of the Bahamas may be related to the subsurface-intensified Antilles current, a western boundary current which flows northward and northwestward offshore of the Bahamas before joining the Gulf Stream. The Antilles Current reaches to about 1000 m depth with highest velocities around 400 m depth and is known to be highly variable in transport (Meinen et al. 2019). As the Antilles Current reaches similar depths as uLSW and opposes its general direction, their interaction might lead to some of the uLSW being entrained into the Gulf Stream. It explains why Heiderich and Todd's (2020) water class transports show uLSW getting entrained into the Gulf Stream just north of the Florida Strait, much further south than previously observed (see Chapter 2).

While variable flow also brings saltier water into the central and northern control volumes in several locations along the offshore boundaries (Fig. 3-8o), it is fluxed out in other areas, leading to small salt fluxes out of these two control volumes when integrating over the entire offshore boundary (Fig. 3-7e,f). The negative lateral eddy flux through the upstream end of the southern control volume likely reflects variability in the flow through the Florida Strait with stronger northward flow correlating with saltier waters and weaker flow being relatively fresher. Such variability in the Florida Strait may be related to Loop Current variability farther upstream and eddies within the Florida Strait (Fratantoni et al. 1998; Meinen et al. 2010; Androulidakis et al. 2020).

At the downstream end of the northern control volume $\iint_{A_L} \langle \mathbf{v}_H{}' S' \rangle \cdot \hat{\mathbf{n}}_H \, dA_L$ is negative as well (Fig. 3-8n and Fig. 3-7f). This is where the Gulf Stream crosses over the DWBC carrying uLSW, so a variable influx of salty water is to be expected in this area. Similarly, the Gulf Stream is meandering and highly variable downstream of the Charleston Bump (Bane and Brooks 1979), which is why the eddy salt fluxes on the upstream boundary of the northern control volume are large (Fig. 3-7f and Fig. 3-8m). For all three control volumes, the residuals of $\iint_{A_L} \langle \mathbf{v}_H{}' S' \rangle \cdot \hat{\mathbf{n}}_H \, dA_L$ have the same magnitude as the net fluxes, suggesting that the horizontal eddy fluxes through the lateral faces tracing the the top and bottom isopycnals (or the bottom where the ocean is shallower than the bottom isopycnal) as well as the inshore boundary are important contributors to the net lateral eddy fluxes.

Since the net lateral eddy salt flux and net mean advective salt fluxes are of the same sign in each of the three control volumes, vertical salt fluxes must play an important role in balancing the salt budget and eroding the θ–S signature of AAIW. Although we do not measure these processes directly, we can verify whether the

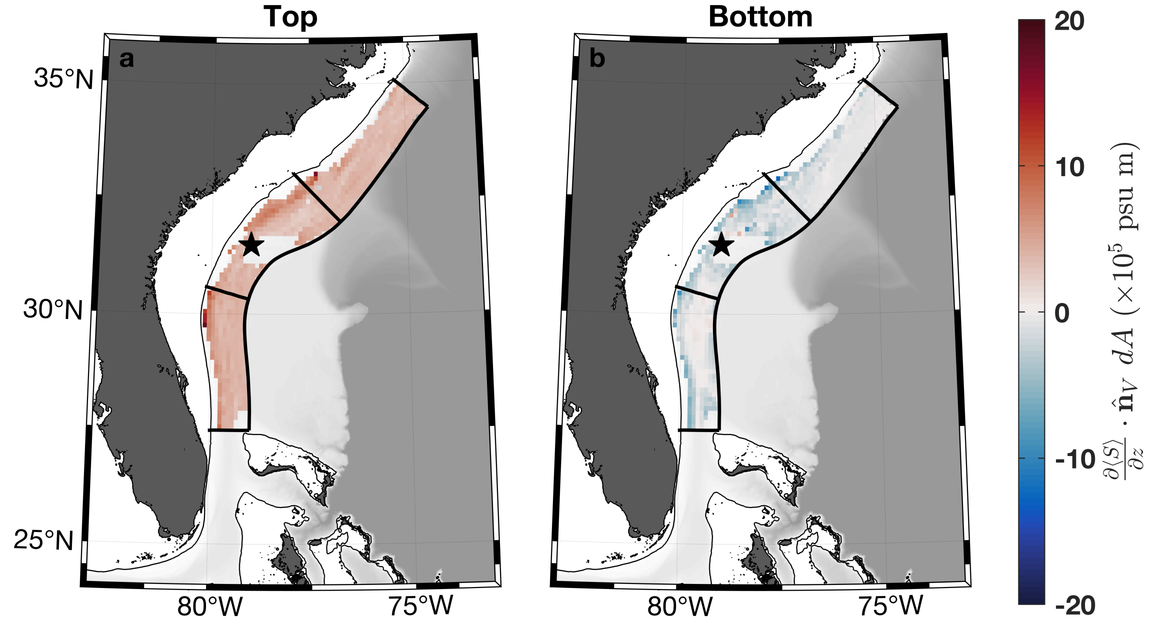

Figure 3-9: Vertical mean salinity gradient in the normal direction of the control volume multiplied with the area of the corresponding face ($\frac{\partial \langle S \rangle}{\partial z} \cdot \hat{\mathbf{n}} \; dA$) on the (a) top and (b) bottom faces of the three control volumes. The thin and thick black lines and the star are as in Fig. 3-1(a).

vertical salinity gradient has the correct sign to allow a downgradient vertical eddy flux to balance the net lateral salt fluxes. We estimate the vertical salinity gradient $\frac{\partial \langle S \rangle}{dz}$ by first differencing $\langle S \rangle$ at the grid points, so that the gradient is directly given at the faces of the control volume. The outermost values are repeated on the top and bottom faces of the water column. The gradient at the four corners of each face is then interpolated to the centroid of the face. Assuming an unknown, but constant, vertical eddy diffusivity κ_V in Eq. (3.5) for each top or bottom face, we compute $\iint_{A_H} \frac{\partial \langle S \rangle}{dz} \cdot \hat{\mathbf{n}}_V \, dA_H$ for each face (Fig. 3-9).

This quantity is positive everywhere on the top faces, meaning that saltier water is found above all of the control volumes. Thus, vertical mixing with the waters above would lead to an additional salt flux into all of the control volumes. For the central and northern control volumes, this is the correct sign to balance the net lateral salt fluxes of salt out of the control volumes. However, for the southern control volume,

$\iint_{A_H} \frac{\partial \langle S \rangle}{dz} \cdot \hat{\mathbf{n}}_V \, dA_H$ on the top faces does not have the correct sign to balance the lateral mean and eddy salt fluxes into the volume. On the bottom faces, $\iint_{A_H} \frac{\partial \langle S \rangle}{dz} \cdot \hat{\mathbf{n}}_V \, dA_H$ is much smaller and often negative (i.e., waters below are fresher), so it either has little effect or fluxes salt out. For the southern control volume, the net lateral fluxes as well as the vertical mixing through the top faces all add salt to the control volume and thus do not balance.

Where $\iint_{A_H} \frac{\partial \langle S \rangle}{dz} \cdot \hat{\mathbf{n}}_V \, dA_H$ is of the correct sign to balance the lateral fluxes (i.e., in the central and northern control volumes), Eq. (3.5) allows us to estimate an isotropic κ_V. The resulting estimates, however, are much larger ($\mathcal{O}(10^{-2})$ m^2 s^{-1}) than should reasonably be expected. For comparison, typical directly observed vertical diffusivities are $\mathcal{O}(10^{-5})$ m^2 s^{-1} (Talley et al. 2011). Global-averaged diapycnal diffusivity above 1000-m depth from a large collection of microstructure profiles is $\mathcal{O}(10^{-5})$ m^2 s^{-1} (Waterhouse et al. 2014). Even Munk's (1966) estimate of a globally averaged vertical eddy diffusivity that accounts for the observed average global density structure is smaller than these estimates ($\mathcal{O}(10^{-4})$ m^2 s^{-1}). Bottom boundaries are regions with rough topography that are known for strong vertical mixing, but observation-based estimates of vertical diffusivities in these areas are also smaller ($\mathcal{O}(10^{-4}$ to $10^{-5})$ m^2 s^{-1}) than our estimates (e.g., Polzin et al. 1997; Kunze et al. 2006; Waterhouse et al. 2014). In the southern control volume, application of Eq. (3.5) would yield a nonphysical negative value of κ_V. These inconsistencies indicate that other terms in Eq. (3.4) that we cannot evaluate and uncertainties in our estimates likely play an important role and cannot be neglected. See section 3.3.2.6 for more information on this and the limitations of this study.

3.3.2.5 Estimates of horizontal diffusivity κ_H^*

Since we measure the lateral eddy fluxes, we can also estimate what a bulk horizontal eddy diffusivity κ_H^* would have to be if these fluxes were parameterized as an eddy diffusive flux. We equate the lateral eddy advective flux divergence (2a) with a lateral eddy diffusive flux divergence and assume that κ_H^* is isotropic in a control volume:

$$\iint_{A_L} \langle \mathbf{v}' S' \rangle \cdot \hat{\mathbf{n}}_H \, dA_L = -\kappa_H^* \iint_{A_L} \nabla_H \langle S \rangle \cdot \hat{\mathbf{n}}_H \, dA_L. \tag{3.6}$$

Note that this is not the same as equating (2a) and (3a) since the scales of interest are different. (3a) represents lateral fluxes at scales smaller than the $\mathcal{O}(10)$-km scale resolved by our observations, with κ_H being a horizontal diffusivity appropriate for those smaller scales. On the other hand, we take κ_H^* to be an eddy diffusivity appropriate to the mesoscale and larger features resolved by the glider observations. The horizontal gradient of salinity is calculated by centered differencing, so that it is given at the location of the grid points. As for the vertical gradient, the outermost gradient value is repeated on the next outer face. For each face, only the component of the horizontal salinity gradient that is normal to it is taken into account. We do not compute κ_H^* locally, but rather obtain a bulk estimate for each upstream, downstream, and offshore boundary.

Estimates of κ_H^* for the different control volumes and their boundaries, as well as the corresponding integrated horizontal salinity gradient $\iint_{A_L} \nabla_H \langle S \rangle \cdot \hat{\mathbf{n}}_H \, dA_L$ are given in Table 3.1. Most of our estimates of κ_H^* have magnitudes of 10^2 to 10^4 m^2 s^{-1} and are thus of similar order as canonical estimates for horizontal eddy diffusivity (e.g., Talley et al. 2011; Cole et al. 2015). The estimates of large-scale horizontal diffusivities in the Gulf Stream presented in Klymak et al. (2016) are based on observations downstream of Cape Hatteras and of comparable magnitude as well ($\mathcal{O}(10^2)$ m^2 s^{-1}). In some cases, our estimates of κ_H^* are negative, indicating that parameterizing the lateral eddy fluxes as downgradient diffusion relative to the time-mean salinity is not ideal.

At a given depth, mean salinity $\langle S \rangle$ typically increases offshore, so that the horizontal salinity gradient $\nabla_H \langle S \rangle$ is directed offshore (Fig. 3-10 and Fig. 3-8t). Stirring of this mean field would tend to result in a shoreward salt flux (i.e., into the control volume). However, our estimated lateral eddy fluxes $\langle {v_H}' S' \rangle$ often have a large cross-stream component directed offshore (Fig. 3-11) and are thus directed up the mean

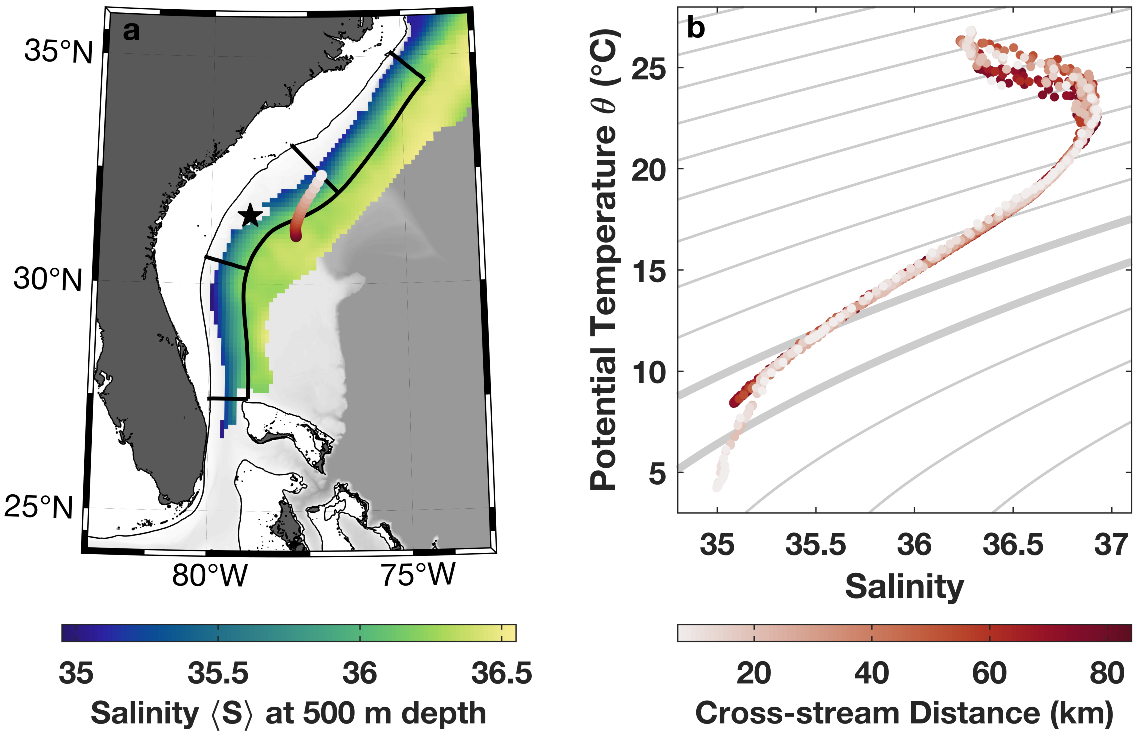

Figure 3-10: (a) Mean salinity $\langle S\rangle$ at 500 m depth. The thin and thick black lines and the star are as in Fig. 3-1. (b) Potential temperature-salinity (θ–S) diagram of glider observations collected along a transect shown in red in (a). The gray lines are isopycnals with 0.5 kg m^{-3} spacing and the $\sigma_\theta = 27$ and 27.5 kg m^{-3} contour lines highlighted in bold. In both (a) and (b), the different shades of red correspond to the cross-stream distance of the observations.

salinity gradient in many locations (i.e., they would "reinforce" the mean gradient). These large cross-stream salt fluxes are mostly found in areas that are known for high variability and large Gulf Stream meanders: in the lee of the Charleston Bump (Bane and Brooks 1979) and near Cape Hatteras where the Gulf Stream encounters the DWBC. The cross-stream salt fluxes are much larger inside of our control volumes than along their boundaries, but for the offshore sides of the central and northern control volumes, they are still mostly directed up the mean salinity gradient (Fig. 3-8o and Fig. 3-11), resulting in non-physical negative horizontal diffusivities when they are parameterized as a downgradient diffusion relative to the time-mean salinity. Although the salinity increases offshore in the mean, this gradient can temporarily be

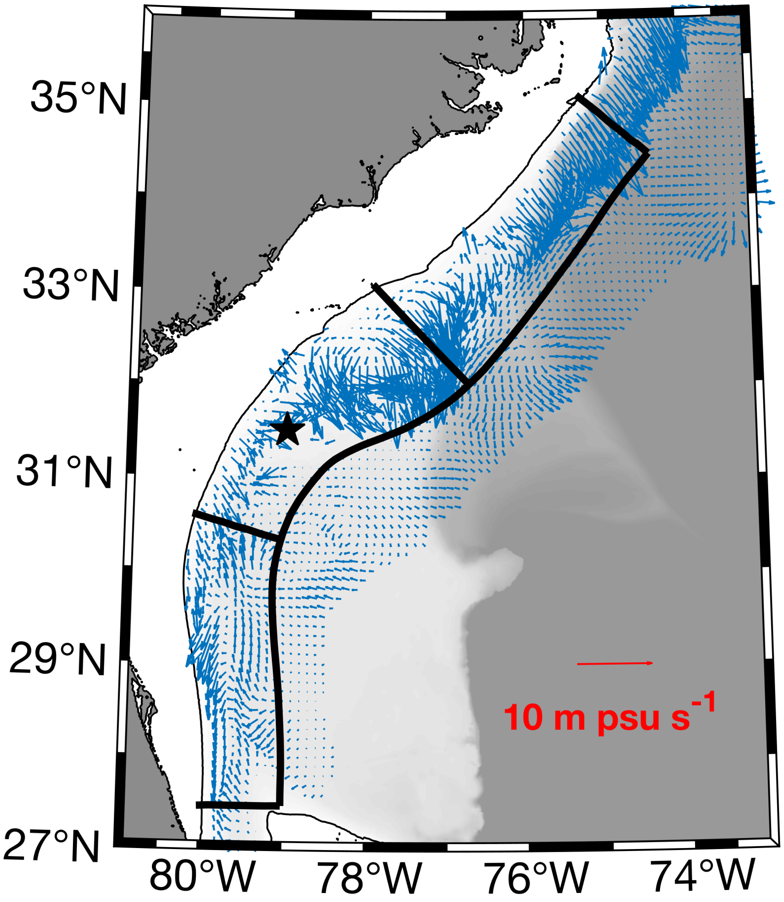

Figure 3-11: Lateral eddy salt advection $\langle \mathbf{v}_H{}'S' \rangle$ vertically integrated within the top and bottom isopycnals bordering the control volumes. The thin and thick black lines and the star are as in Fig. 3-1(a). An arrow for scale is shown in red in the bottom right.

reversed, as shown in an example transect where the saltier uLSW tail in the potential temperature-salinity (θ–S) plot was found inshore of AAIW (Fig. 3-10b). In these instances, offshore eddy fluxes would be directed down the temporary gradient as expected.

Observations of upgradient heat and momentum eddy fluxes in the Gulf Stream upstream of Cape Hatteras were reported as early as the 1960s (e.g., Webster 1961, 1965; Oort 1964). Many follow-up studies confirmed these results by revisiting the original Webster data set (Schmitz and Niiler 1969), analyzing independent in situ and satellite observations (e.g., Brooks and Niiler 1977; Bane et al. 1981; Brooks and Bane 1983; Hood and Bane 1983; Lee et al. 1981, 1991), and modeling (Gula et al. 2015). Most of the observations of upgradient fluxes are in the areas upstream and downstream of the Charleston Bump and near Cape Hatteras, but also in the Florida Strait. These are the locations where we also observe strong upgradient fluxes in our control volumes (Fig. 3-11), albeit at deeper depths than many previous observations. Rossby (1987) explains how meandering of the Gulf Stream front can lead to upgradient eddy fluxes in an Eulerian framework and thus should not be treated as a diffusive process.

3.3.2.6 Limitations

As we already alluded to at the end of section 3.3.2.4, we cannot back out sensible estimates of vertical diffusivity κ_V because some of the terms in Eq. (3.4) that we cannot evaluate using the glider observations likely play an important role and there are uncertainties in our estimates.

The lateral mean and eddy advective salt fluxes are much better constrained than the vertical terms, since the glider's AD2CPs directly measure horizontal velocities. The glider-based three-dimensional fields capture the Gulf Stream and its associated horizontal velocities quite well: The mean fields show typical Gulf Stream features and our estimates of the lateral eddy salt fluxes have a spatial structure that resembles that of heat and momentum fluxes from independent observations (see section 3.3.2.5). Moreover, estimates of mean and eddy kinetic energy (MKE and EKE) based on the same three-dimensional fields as used here compare well with independent satellite-based estimates of MKE and EKE (Todd 2021). Nevertheless, there are of course uncertainties in our lateral flux estimates. Measurement errors of the glider instruments are small: Heiderich and Todd (2020) estimate random errors of 0.1 m s^{-1} for individual glider AD2CP-based absolute velocity profiles and Sea-Bird Scientific report a conductivity accuracy of ± 0.0003 S m^{-1} corresponding to ± 0.0035 psu for their 41 CP CTD with a typical conductivity stability of 0.0003 S m^{-1} $month^{-1}$ or 0.0011 psu per year. Propagating the velocity error estimate from Heiderich and Todd

(2020) through the weighted least-squares scheme used to produce the mean fields results in random error estimates of less than 0.02 m s^{-1} for $\langle u \rangle$ and $\langle v \rangle$ in areas that are well sampled (Todd 2021). As in Todd (2021), areas with random errors larger than this threshold or that are not well sampled otherwise (e.g., due to seasonal bias) are masked in the mean $\langle \cdot \rangle$ and prime $\cdot'$ fields used here. Random errors for the mean salinity fields will be even smaller since CTD measurements are more accurate. In the following, we will assume random errors of $\sigma_{\langle v \rangle} = 0.02$ m s^{-1} for the mean velocity and random errors of $\sigma_{\langle S \rangle} = 0.001$ psu for salinity, and that salinity and velocity are independent (which they should be since they are measured by two different instruments). Following standard error propagation and assuming typical mean salinities of 36 psu and typical current speeds of 0.1 m s^{-1} to 1 m s^{-1}, the random errors for the mean lateral advective fluxes will be $\frac{\sigma_{\langle v \rangle \langle S \rangle}}{\langle v \rangle \langle S \rangle} = \sqrt{\left(\frac{\sigma_{\langle S \rangle}}{\langle S \rangle}\right)^2 + \left(\frac{\sigma_{\langle v \rangle}}{\langle v \rangle}\right)^2} \approx 10^{-1} - 10^{-2}$, or a few percent of the mean values. Due to the large amount of observations entering the mean fields, the random errors are small. However, these estimates do not take into account any bias in the sampling in both space and time, which is likely much larger and more difficult to quantify. As mentioned previously, we attempt to minimize these biases through masking.

Gliders mostly capture mesoscale processes and thus any processes at scales smaller than a few tens of kilometers (i.e., the submesoscale and below) are not resolved or are contaminated by high-frequency variability (see Rudnick and Cole 2011). We assume that these processes can be parameterized as a diffusive flux divergence [term (3a) in Eq. (3.4)] that is negligible, which might not be the case. It is therefore important to keep in mind that our lateral flux estimates are scale dependent. Here, we are interested in the large-scale processes that lead to the erosion of AAIW in the Gulf Stream. Despite the unresolved smaller scale processes, we can still estimate larger-scale lateral mean and eddy advective fluxes. Since they clearly do not balance in any of the control volumes, we can still conclude that vertical processes must play an important role in the erosion for larger scales, even though smaller scale horizontal processes may also contribute to the overall salt balance.

Residual lateral fluxes are comparable to both the mean and eddy fluxes through the vertical sides of the control volumes. A likely contributor to this is mean and varying flow through the vertical faces of control volume cells that follow the sloping top and bottom time-mean isopycnals (lateral blue faces in Fig. 3-4b,d,f). In general, we expect flow to be along isopycnals and thus to have a vertical component when flowing parallel to a gradient in isopycnal depth (e.g., across a front). Consequently, lateral flux into (out of) a particular cell would tend to be canceled by vertical flux out of (into) the same cell. However, we are unable to measure these vertical advective fluxes. In principle, evaluation of Eq. (3.3) in density coordinates would alleviate this problem, but it is not feasible to construct mean fields in density coordinates due to the time-varying position of isopycnals relative to fixed bathymetry.

Since we do not have usable estimates of vertical velocities w, the contribution of vertical processes to the erosion of AAIW is much harder to assess. In particular, where isopycnals become steep within the core of the Gulf Stream, any vertical component of along-isopycnal flow may be significant. As for the lateral salt fluxes (see section 3.3.2.5), instantaneous meandering of isopycnals with respect to the top and bottom of our control volumes (which are defined based on mean isopycnals) may create fluxes that should not be parameterized as a downgradient diffusion. This may be particularly important for the vertical eddy advective fluxes $\langle w'S' \rangle$ [term (2b) in Eq. (3.4)] that we have assumed can be parameterized as a diffusive flux in the opposite direction of the time-mean vertical salinity gradient in section 3.3.2.1. Since our control volumes are far away from the surface Ekman layer and the Gulf Stream is largely geostrophic, the assumption that mean vertical velocities are small and the vertical mean advective fluxes $\langle w \rangle \langle S \rangle$ [term (1b) in Eq. (3.4)] are negligible is probably reasonable.

3.4 Summary

Using three-dimensional fields constructed from Spray underwater glider observations, we estimate lateral mean and eddy salt fluxes into three control volumes to understand the mechanisms that lead to the erosion of Antarctic Intermediate Water in the Gulf

Stream. AAIW enters the Gulf Stream through the Florida Strait and its salinity signature in potential temperature–salinity (θ–S) space is observed to be eroded away as it flows northward in the Gulf Stream (Fig. 3-1b,c). The low salinity signature of AAIW disappears around the Charleston Bump (Fig. 3-2), an underwater ridge and trough feature that is known as an area of enhanced bottom mixing and internal wave activity (Todd 2017).

Both lateral stirring and vertical mixing likely play a role in supplying the saltier water with which AAIW ultimately mixes. In all three control volumes, the net lateral mean and eddy advective fluxes are of the same sign (either adding or removing salt to the control volume, see Fig. 3-7), indicating that vertical processes must play an important role in the erosion, though they cannot be quantified based on the glider observations. In the central control volume where the low salinity signature of AAIW fades near the Charleston Bump, we see an outward flux of salt through lateral advection which must be balanced by a vertical salt flux down across the top of the control volume, likely through mixing with the saltier water above. Just north of the Bahamas, saltier upper Labrador Sea Water and related waters are able to flow up onto the relatively shallow Blake Plateau and become entrained in the Gulf Stream, where they subsequently mix with AAIW (Fig. 3-8o and Fig. 3-7f). Variable flow (e.g., eddies which are possibly associated with the Antilles Current), allows uLSW to cross isobaths, but the exact pathways remain unclear. This mechanism explains why Heiderich and Todd (2020) found entrainment of uLSW just north of the Florida Strait in their water class transports. The entrainment occurs much farther south of Cape Hatteras than previously reported.

We had hoped to obtain an estimate of the vertical diffusivity κ_V for the Gulf Stream through this analysis, but since some of the terms that play an important role in Eq. (3.4) cannot be evaluated from the glider data and noise/errors in our estimates may be significant, we cannot back out κ_V in a meaningful way. Neverless, the three-dimensional fields at least provide large-scale estimates of the lateral advective salt fluxes in the Gulf Stream. Unlike observational platforms, numerical simulations, particularly those constrained to match observations, can be used to evaluate these terms and provide estimates of vertical diffusivity in the Gulf Stream using the analysis outlined here. Moreover, modeling studies may elucidate the persistence of uLSW pathways, the fate of the DWBC below the glider sampling depth, and the processes governing the evolution of the benthic front between AAIW and uLSW just north of the Bahamas.

3.A Appendix

The temporal averaging scheme of Todd (2021) is applied at each individual grid point and thus is not designed to enforce nondivergence in the mean flow field $\langle \mathbf{v} \rangle = (\langle u \rangle, \langle v \rangle)$. Here we adjust the mean flow fields so that there is zero net horizontal volume flux in each of the M grid cells, each of which is defined by four corner grid points at a particular depth. We seek a set of horizontal velocity adjustments

$$\Delta \mathbf{v} = \left(\begin{array}{c} \Delta u_1 \\ \vdots \\ \Delta u_N \\ \hline \Delta v_1 \\ \vdots \\ \Delta v_N \end{array} \right), \tag{3.7}$$

where N is the total number of grid points with mean velocity estimates at a particular depth.

We construct an $M \times N$ operator $\mathbf{G}$ that computes the net horizontal volume flux into each grid cell. The horizontal volume flux T_{ij} into the cell spanning $[x_i, x_{i+1}] \times [y_i, y_{i+1}]$ is

$$\begin{aligned} T_{ij} \quad = \quad & -\frac{1}{2}(u_{i,j} + u_{i+1,j})(y_{i+1,j} - y_{i,j})\Delta z \\ & +\frac{1}{2}(u_{i,j+1} + u_{i+1,j+1})(y_{i+1,j+1} - y_{i,j+1})\Delta z \\ & -\frac{1}{2}(v_{i,j} + v_{i,j+1})(x_{i,j+1})(x_{i,j+1} - x_{i,j})\Delta z \\ & +\frac{1}{2}(v_{i+1,j} + v_{i+1,j+1})(x_{i+1,j+1} - x_{i+1,j})\Delta z, \end{aligned} \tag{3.8}$$

where Δz =10 m is the vertical extent of each cell and we have omitted the angle brackets around each mean velocity component for clarity. Rearranging to collect coefficients on each velocity component estimate,

$$T_{ij} = \frac{\Delta z}{2} \left(\begin{array}{c} -\Delta y_j \\ -\Delta y_j \\ \Delta y_{j+1} \\ \Delta y_{j+1} \\ \hline -\Delta x_i \\ -\Delta x_i \\ \Delta x_{i+1} \\ \Delta x_{i+1} \end{array} \right)^T \left(\begin{array}{c} u_{i,j} \\ u_{i+1,j} \\ u_{i,j+1} \\ u_{i+1,j+1} \\ \hline v_{i,j} \\ v_{i,j+1} \\ v_{i+1,j} \\ v_{i+1,j+1} \end{array} \right), \tag{3.9}$$

where $\Delta x_i = x_{i,j+1} - x_{i,j}$ and $\Delta y_j = y_{i+1,j} - y_{i,j}$. We define a single index $k = N_y(j-1)+i$ with N_y the number of grid points in latitude, and construct the elements of $\mathbf{G}$ such that

$$\mathbf{G} \left(\begin{array}{c} u_1 \\ \vdots \\ u_N \\ \hline v_1 \\ \vdots \\ v_N \end{array} \right) = \left(\begin{array}{c} T_1 \\ \vdots \\ T_M \end{array} \right). \tag{3.10}$$

To find adjustments $\Delta\mathbf{v}$ such that there is no net horizontal flux into each grid cell, we use constrained least squares. We seek to minimize the size of the velocity adjustments $\Delta\mathbf{v}^T\Delta\mathbf{v}$ while enforcing that $\mathbf{G}\Delta\mathbf{v}$, the net flux into each cell due to the velocity adjustments, exactly cancels $\mathbf{G}\langle\mathbf{v}\rangle$, the net flux into each cell due to the estimated mean velocity field. Using the method of Lagrange multipliers, we construct a cost function $\mathcal{L}$ as

$$\mathcal{L} = \Delta\mathbf{v}^T\Delta\mathbf{v} + \lambda^T(\mathbf{G}\Delta\mathbf{v} + \mathbf{G}\langle\mathbf{v}\rangle). \tag{3.11}$$

Following standard methods, the least-squares solution for $\Delta\mathbf{v}$ is

$$\Delta\mathbf{v} = -\mathbf{G}^T(\mathbf{G}\mathbf{G}^T)^{-1}\mathbf{G}\langle\mathbf{v}\rangle. \tag{3.12}$$

These adjustments to the mean flow field are generally small. Over the full three-dimensional grid, 50% of adjustments have magnitude less than 0.025 m s^{-1}, 81% have magnitude less than 0.05 m s^{-1}, and 98% have magnitude less than 0.1 m s^{-1}.

Throughout the main text, $\langle\mathbf{v}\rangle$ represents the end result of averaging individual velocity estimates using the $\langle\cdot\rangle$ operation as in Todd (2021) and then adding the velocity adjustments $\Delta\mathbf{v}$ derived here.

Chapter 4

Comparing Gulf Stream transport estimates from underwater gliders and satellite altimetry

Abstract

Observations from underwater gliders are compared with a gridded satellite altimetry product to investigate how well satellite-based estimates of cross-stream sea surface height differences ΔSSH capture the observed variability in Gulf Stream transport. For the entire U.S. East Coast, about 50% of the variability in transport is captured, most of which can be attributed to large-scale spatial variability, suggesting a barotropic increase in transport as has been previously observed. The gridded product fails to fully capture the transport variability in individual subregions like the Florida Strait, the South Atlantic Bight, or the Middle Atlantic Bight and local short-term transport fluctuations due to resolution issues. At the surface, ΔSSH compares more favorably with transport estimates based on geostrophic velocities than with transport estimates that are based on velocities that are directly measured by acoustic Doppler current profilers (AD2CPs) on the gliders. Generally, correlations between ΔSSH and transport per unit depth are higher further away from the surface where ageostrophic effects become less prominent. Consequently, correlations between ΔSSH and transport integrated from the surface increase with depth because ageostrophic effects contribute a smaller fraction of the transport. The variability in water class transport is best captured by altimetry for water classes that are located below the thermocline (i.e., Eighteen Degree Water, upper Labrador Sea Water, and other intermediate waters). Since gridded satellite altimetry fails to capture almost half of the variance in Gulf Stream transport (and even more at small spatial scales), it cannot replace in situ observational platforms, though there may be the potential for creating an SSH-based metric to track large-scale changes in Gulf Stream transport along the entire U.S. East Coast.

4.1 Introduction

As a strong, narrow western boundary current in the subtropical North Atlantic and a principal contributor to the upper limb of the Atlantic Meridional Overturning Circulation, the Gulf Stream transports large amounts of water and heat poleward (Wunsch 2005; Cunningham et al. 2007). The Stream moves warm and salty waters from the tropics through the Florida Strait and along the U.S. East Coast veering into the open ocean near Cape Hatteras, North Carolina, and flowing towards Europe. On its way to higher latitudes, the Gulf Stream travels through distinct regions that are governed by different dynamics affecting its structure and transport. In most of the Florida Strait (FS), the Gulf Stream is confined to a channel and is thus a comparatively straight meridional jet. As the Stream continues to flow over the continental slope in the South Atlantic Bight (SAB), it remains bathymetrically stabilized, but becomes a freely meandering jet once it detaches from the continental slope near Cape Hatteras and enters the Middle Atlantic Bight (MAB). It has long been established that Gulf Stream transport increases in the along-stream direction (e.g., Knauss 1969; Leaman et al. 1989); it approximately doubles between the Florida Strait and the Middle Atlantic Bight due to the entrainment of subthermocline waters including Eighteen Degree Water and upper Labrador Sea Water (Heiderich and Todd 2020). See Chapter 2 for more details on Gulf Stream transport and water properties.

Monitoring of energetic ocean currents like the Gulf Stream over different time and spatial scales requires a variety of observational platforms. Long-term time series of Gulf Stream transport exist in only two portions of the the Gulf Stream: from an undersea cable as part of the Western Boundary Time Series in the Florida Strait (Baringer and Larsen 2001; Shoosmith et al. 2005; Meinen et al. 2010) and from vessel-mounted ADCP measurements taken along the CMV *Oleander* line (Flagg et al. 2006; Andres et al. 2020). A large field program routinely surveying the U.S. East Coast with autonomous underwater gliders since 2015 returns contemporaneous subsurface measurements of hydrography and velocity (Todd 2017, 2021; Heiderich and Todd 2020). In combination with earlier pilot glider missions (Todd et al. 2016), it allows us to estimate Gulf Stream transport from 185 cross–Gulf Stream transects. However, only two gliders typically survey the Gulf Stream at any given time, and they are often separated by several hundred kilometers. The gliders move slowly with the current, taking several months to sample the Gulf Stream between the Florida Strait and Cape Cod. Thus, they do not provide synoptic broad-scale coverage of the Gulf Stream. The Gulf Stream exhibits substantial variability in its position and strength at timescales from several weeks (e.g. Gawarkiewicz et al. 2012) to years (e.g., Rossby and Benway 2000; Meinen et al. 2010; Andres 2016). Shorter term variability on time scales of days to weeks is also significant (e.g., Schott et al. 1988; Volkov et al. 2020); for example transient reductions in Gulf Stream transport have been observed after the passing of hurricanes (Ezer et al. 2017; Todd et al. 2018). In contrast to in situ measurement systems, satellites are able to frequently sample the Gulf Stream over much broader spatial scales. They have provided reliable, relatively continuous, gap-free altimetry measurements as part of the Global Ocean Observing System since 1991 (Fu and Cazenave 2001; Fu and Ubelmann 2014).

Satellite-based estimates of sea surface height (SSH) are directly related to ocean surface currents through geostrophy. Strong western boundary currents like the Gulf Stream are, to first order, in geostrophic balance in the cross-stream direction such that the surface velocity is associated with a cross-stream gradient in sea surface height. If fluctuations in the surface geostrophic velocity are correlated with fluctuations in velocity throughout the entire water column, then the potential exists to relate the satellite-based sea level differences across the Gulf Stream to volume transports. In the Florida Strait, Volkov et al. (2020) found that satellite-derived estimates of Florida Current transport captured about 60% of the variability observed in concurrent estimates derived from motion-induced voltage differences in an undersea cable (southern red line in Fig. 4-1a). Despite the lower temporal resolution compared to the cable measurements, satellite altimetry reproduced the seasonal, intra-seasonal, and inter-annual variability in Gulf Stream transport through the Florida Strait reasonably well; even capturing large short-term transport fluctuations due to hurricanes (Volkov et al. 2020). Tide gauges and bottom pressure recorders (BPRs) can also be

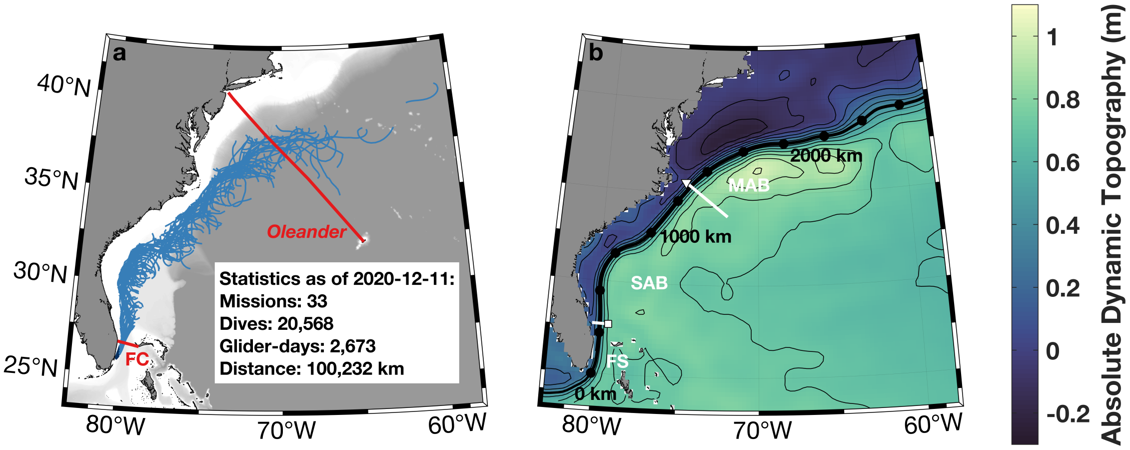

Statistics as of 2020-12-11:
Missions: 33
Dives: 20,568
Glider-days: 2,673
Distance: 100,232 km

Figure 4-1: (a) Map of all glider transects across the Gulf Stream (blue). In the Florida Strait, glider dives for which no absolute dynamic topography estimates from satellite altimetry exist are highlighted in dark blue. The red lines indicate the locations of other sustained Gulf Stream sampling programs: the Florida cable (FC) and the CMV *Oleander* line. Statistics for the underwater glider missions including all dives (not only the ones used for transport calculations) are shown in the box in the lower right. (b) Absolute dynamic topography (ADT) from satellite altimetry averaged over the years spanning the glider observations (1 January 2004–31 December 2020), using delayed-time data when available (until 7 March 2020) and near-real-time data otherwise. Mean ADT contours with 10-cm intervals are also shown in black with the 40-cm contour emphasized in bold. Black dots every 250 km along the 40-cm SSH contour indicate an along-stream coordinate system originating at 25°N. The white lines separate three different dynamical regions of the Gulf Stream: the Florida Strait (FS), the South Atlantic Bight (SAB), and Middle Atlantic Bight (MAB). "The Point" offshore of Cape Hatteras is indicated as a white triangle, and the northwestern edge of Little Bahama Bank at the 500-m isobath as a white square.

used to infer transport from sea level/pressure differences across the Florida Strait using geostrophy (e.g., Maul et al. 1985; Schott and Zantopp 1985); this was especially useful before the era of altimetric satellite observations. Several studies using tide gauges and BPRs confirm that sea level changes across the Florida Strait are representative of changes in transport to a certain extent, typically accounting for about 55%–60% of the variance in transport for time scales ranging from a couple of days to a year (Maul et al. 1990; Meinen et al. 2021).

Farther downstream in the Middle Atlantic Bight, acoustic Doppler current profilers (ADCPs) mounted on the container vessel CMV *Oleander* have provided weekly transects of upper ocean velocity along a line between New York and Bermuda since 1992 (northern red line in Fig. 4-1a; Flagg et al. 2006; Andres et al. 2020). Altimetry-based surface geostrophic velocities from the TOPEX/Poseidon-Jason-1 tandem missions show reasonable agreement with the CMV *Oleander* velocities (Stammer and Theiss 2004). For the Gulf Stream portion of the CMV *Oleander* line, upper ocean variability is also captured well. Worst et al. (2014) estimate correlation coefficients of 0.88 between altimeter-based and ADCP-based transport per unit depth near the surface (i.e., 77% of the variance is explained). However, Worst et al. (2014) note that the correlation coefficients are sensitive to the endpoints chosen for the flux estimates.

As these previous studies have shown, fluctuations in sea level differences represent fluctuations in Gulf Stream transport fairly well over various time scales at two different locations. However, ageostophic effects like centrifugal accelerations due to curved flow and wind-driven Ekman transport near the surface also play an important role, leading to considerable deviations from geostrophy. Here, we assess how well satellite-altimetry-based estimates of sea surface height capture the variability in Gulf Stream transport observed by underwater gliders. The large glider data set allows us to compare transport estimates and SSH along the entire U.S. East Coast. In particular, we consider the correlation between fluctuations in cross-stream sea surface height difference ΔSSH and variations in Gulf Stream transport for full depth transport, for transport per unit depth at the surface and as a function of depth, in different geographic regions, and for different water classes. Moreover, we assess whether altimetry primarily captures spatial or temporal variability. The glider observations and satellite altimetry products used in this analysis are described in sections 4.2.1 and 4.2.2. Section 4.2.3 briefly summarizes how we estimate Gulf Stream transport from glider observations, and section 4.2.4 explains how we estimate the sea level difference ΔSSH along a glider transect. In section 4.3, we investigate the correlation between glider-based Gulf Stream transport estimates and satellite-based ΔSSH, while section 4.4 reviews our findings and their significance.

4.2 Observations and methods

4.2.1 Glider observations

We use concurrent observations of hydrography and velocity from a field program that has been routinely surveying the Gulf Stream along the U.S. East Coast since 2015 using autonomous underwater gliders (Todd 2017, 2021; Heiderich and Todd 2020). Additionally, we have hydrographic data from four glider missions that sampled the Gulf Stream in the MAB between 2004 and 2009 (Todd and Owens 2016). Spray gliders (Sherman et al. 2001; Rudnick et al. 2016) are typically deployed near Miami, FL, and piloted back and forth across the Gulf Stream until they reach the shelfbreak south of Cape Cod, Massachusetts, approximately 120 days later. The gliders are advected downstream while they sample the upper kilometer of the ocean in a sawtooth fashion (or to within a few meters above the bottom where the ocean is less deep), resulting in approximately 10 oblique crossings of the current per mission. All gliders carried pumped Sea-Bird 41CP CTDs to collect observations of temperature, salinity, and pressure. Since July 2015, gliders have also been equipped with 1-MHz Nortek acoustic Doppler dual current profilers (AD2CPs; Todd et al. 2017) providing estimates of absolute velocity. All observations are binned to a uniform vertical grid with 10-m resolution. The data set, continuing field program, sampling process, quality control, postprocessing, and accuracy of velocity estimates are described in detail in Heiderich and Todd (2020). Compared to Heiderich and Todd (2020), we include data from six additional missions completed between February and December 2020, resulting in a total of 225 Gulf Stream crossings from 33 glider missions being available for this analysis (see Fig. 4-1a for mission statistics). In addition to using the direct velocity estimates from AD2CPs when available, we estimate geostrophic velocities for all transects by objectively mapping the along-track density gradient to the profile locations, deriving the thermal wind velocity profile, and referencing it to the cross-track component of the depth-average current as in Heiderich and Todd (2020).

4.2.2 Satellite altimetry observations of sea surface height

The satellite-based estimates of absolute dynamic topography (ADT) used in this study were obtained from the EU Copernicus Marine Environment Monitoring Service (CMEMS; `https://marine.copernicus.eu/`). Since we need coverage of the entire Gulf Stream and glider sampling area, we use the gridded 0.25°×0.25° product (Fig. 4-1b) rather than along-track data. We use daily delayed-time products (SEALEVEL_GLO_PHY_L4_REP_OBSERVATIONS_008_047) when available (until 7 March 2020) during the occupation of an entire glider transect, and we use near-real time products (SEALEVEL_GLO_PHY_L4_NRT_OBSERVATIONS_008_046) otherwise. ADT is defined as the sea surface height with respect to the geoid (a gravitational equipotential surface, i.e. the shape of the sea surface only due to Earth's rotation and gravity, without the influence of wind, tides, currents, or other perturbing forces) from the GOCE model. See section 1.4.2 for more information on how ADT is derived from altimetry measurements of instantaneous sea surface height (SSH) above an arbitrary reference ellipsoid. Gridded ADT with respect to a twenty-year (1993–2012) mean sea surface is computed by merging altimetry data from all the available satellite missions (Jason-1, Jason-2, Jason-3, Sentinel-3A, HY-2A, Saral/AltiKa, Topex/Poseidon, ENVISAT, Cryosat-2, GFO, and ERS1/2) using optimal interpolation (Pujol et al. 2016). The gridded product provides estimates of ADT at daily resolution, but since a satellite repeats a track approximately every ten days to a month (ten days for the Jason and Topex/Poseidon satellites and between 14 and 35 days for the other satellites), the daily observations in this highly interpolated product are not independent from each other. Depending on the location and time, different altimeters (and different numbers of altimeters) factor into the estimate. Since large spatial scales are used in the mapping procedure that produces the gridded product, it likely underestimates gradients. Gridded ADT only resolves time scales of about a month and wavelengths of about 200 km (Chelton et al. 2019), which corresponds to feature radius scales around 50 km (Chelton et al. 2011).

4.2.3 Estimating Gulf Stream transport from glider observations

For more details of how Gulf Stream transport is estimated for individual glider transects, see Heiderich and Todd (2020), i.e., Chapter 2. Here, we only summarize the key points.

We select cross–Gulf Stream glider transects using the same criteria as in Heiderich and Todd (2020). A total of 182 out of the 225 available transects fulfill these criteria and are therefore used for transport calculations (Fig. 4-1a), adding 27 additional glider transects compared to Heiderich and Todd (2020). Of those transects, 13 only have geostrophic velocity estimates while all others also have direct velocity estimates from AD2CPs. The transects are placed in a local streamwise coordinate system following Heiderich and Todd (2020). Along-stream position is determined by projecting the midpoint of a transect onto an along-stream coordinate system that is based on the 40-cm ADT contour averaged over 1 January 2004–31 December 2020, a time frame spanning one more calendar year compared to Heiderich and Todd (2020) to account for the extended sampling period due to additional glider observations. The intersection of this contour with 25°N (at 80.05°W) is taken as the origin of this coordinate system (black line with dots in Fig. 4-1b). As in Heiderich and Todd (2020), we project the northwestern-most tip of Little Bahama Bank at the 500-m isobath (white square in Fig. 4-1b) and “The Point" offshore of Cape Hatteras (white triangle in Fig. 4-1b) to the along-stream coordinate system to find the along-stream distances that separate the three different dynamical regions (FS, SAB, MAB; separated by white lines at along-stream distances of 304 and 1367 km in Fig. 4-1b). 11 of the transects used in the transport calculations are in the Florida Strait, 123 are in the South Atlantic Bight, and 48 are in the Middle Atlantic Bight.

For discrete observations, Gulf Stream transport can be computed as the sum of the downstream transports through each measurement cell T_{ij} that is considered to be within the Gulf Stream. As in Heiderich and Todd (2020), we construct upper- and lower-bound transport estimates for each individual glider transect across the Gulf

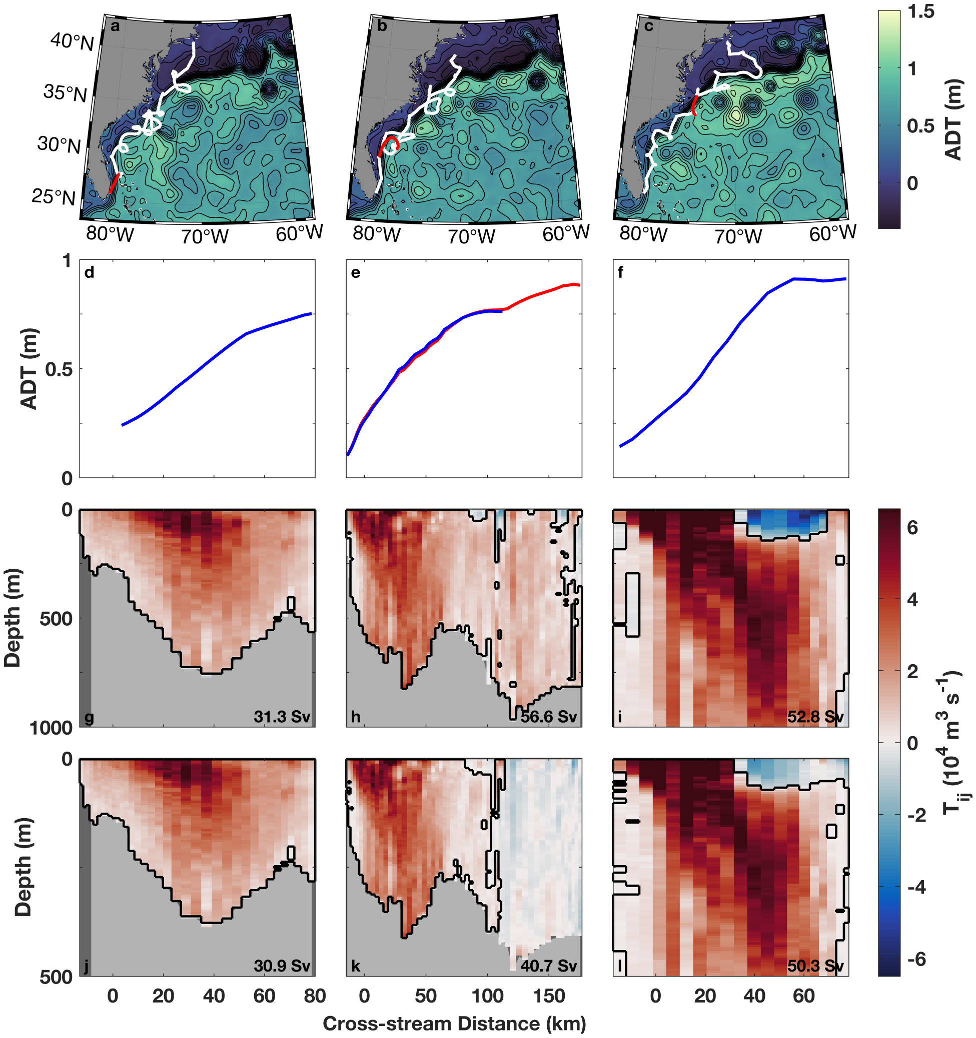

Figure 4-2: Gulf Stream transport and SSH for three example glider transects, one in the Florida Strait from March 2019 (left column), one in the South Atlantic Bight from May 2017 (middle column), and one near Cape Hatteras from October/November 2015 (right column). (a–c) Maps of absolute dynamic topography (ADT) averaged over the time period of the glider transects indicated in red. SSH contours with 10-cm intervals are shown as thin black lines. The white line shows the path of full mission corresponding to the transect. (d–f) ADT averaged over the time period of the glider transect interpolated to the glider transect. The blue lines are averaged over the time period that it took the glider to complete the transect between the edges of the upper-bound transport estimate, while the red lines represent ADT averaged over the time period for the lower-bound transport estimate. In (d) and (f), the red and blue lines are identical. (g–i) Upper-bound estimate of transport through each measurement cell. The integration region for the transport estimates is outlined in black. The bathymetry measured by the glider's AD2CP is shaded in gray, while regions without bathymetry data are shown in dark gray. (j–l) Lower-bound transport estimate, using the same as notation as in (g–i).

Stream due to the challenges of defining a downstream direction for transects that do not cross the current perpendicularly and defining “throughput” in the presence of corotating eddies. The upper-bound estimate captures the maximum possible Gulf Stream transport (e.g., Figs. 4-2g–i), including all the locally downstream flow in a curved Gulf Stream and contributions from eddies along the edges of the current, as long as they fall within the selected transects. Integrating all of the water flowing parallel to the local depth-average current for each profile in the cross-stream direction is equivalent to this upper bound. For the lower-bound estimate (e.g., Figs. 4-2j–l), we scale the upper-bound estimate based on the angle between the local current and a chosen representative direction of the Gulf Stream to exclude flow in directions other than that of the Gulf Stream. The limits of integration in each transect (black outlines in Figs. 4-2g–l) are determined by finding the 4-connected region with the largest transport using the edge finding algorithm described in Heiderich and Todd (2020).

4.2.4 Estimating ΔSSH over a glider transect

For each cross–Gulf Stream glider transect, we calculate the mean absolute dynamic topography averaged over the time period of the glider transect and interpolate it to the locations of each glider dive in the transect. Since altimeter observations near the coast are prone to errors (Vignudelli et al. 2019), the gridded product does not provide estimates of ADT for some of the inshore glider dives in the Florida Strait (dark blue in Fig. 4-1 and inshore gap in Fig. 4-2d). If the Gulf Stream were a purely geostrophic current, the surface transport per unit depth would be directly proportional to the difference in sea level height between the endpoints bracketing the Gulf Stream. Since satellite altimetry frequently misses the inner edge of the Gulf Stream in the Florida Strait, we truncate the glider transects based on where SSH data are available and recalculate transports as described in section 4.2.3. Comparison of the full transport estimates with the estimates from the truncated transects shows that for the 10 transects with AD2CP data in the Florida Strait, the portion of the transects missed by SSH carries on average about 2.5 Sv (1 Sv $\equiv 10^6$ m^3 s^{-1}) or 7%

of the total transport for both the upper- and lower-bound estimates. Upper- and lower-bound transport estimates are almost identical in the Florida Strait where the current has basically no curvature and no corotating eddies (e.g., Figs. 4-2g,j). For the 11 transport estimates based on geostrophic velocities in the Florida Strait, the missed fraction is slightly higher (3.4 Sv or 10%).

We define the cross-stream sea level height difference ΔSSH as the difference in ADT between the first and last dives of the transect that are considered to be within the respective bounds. Thus, for transects with significant curvature or corotating eddies where the lower bound is markedly different from the upper bound (e.g., Fig. 4-2h,k), ΔSSH will often be smaller because the transect is shorter (e.g., Fig. 4-2e). Moreover, ΔSSH is calculated from ADT averaged over a slightly shorter time period (this is why ADT for the upper and lower bounds in Fig. 4-2e are slightly different). The core of the Gulf Stream is tilted (Johns et al. 1995) and thus farther offshore at depth (Fig. 4-2i,l), requiring careful consideration of the endpoints of a transect to make sure that the Gulf Stream core at depth is included. Our transect endpoints and integration limits depend on the depth-average and depth-dependent velocity (see Heiderich and Todd 2020) rather than the surface current. We choose to compute ΔSSH over the lateral span of the entire Gulf Stream in our transects instead of just its surface expression, since surface currents may oppose the mean Gulf Stream direction (as in Fig. 4-2i,l) due to a variety of factors.

Note that we also estimated ΔSSH across each transect using each daily ADT estimate during the transect and then averaging, resulting in basically identical estimates of ΔSSH compared to first averaging the ADT maps in time. Though the absolute value of ADT at a single dive location can in rare cases vary by up to 60 cm in the core of the Gulf Stream over the time span of a transect, the net difference in SSH across the transect normally barely changes. This suggests that the endpoints of our transects are far enough from the Gulf Stream axis that they are not influenced by high-frequency cross-stream shifts in SSH within the Gulf Stream (i.e., the endpoints are outside of the range that meandering of the Gulf Stream axis can reach on the approximately one-week time scale required to complete a single glider transect).

The ΔSSH values using the averages of daily estimates are not shown or discussed further.

4.3 Results and discussion

Having calculated the transport for each transect and the corresponding sea surface height difference ΔSSH across each transect, we now consider the correlations between them to investigate how well satellite altimetry captures the observed variability in Gulf Stream transport. If the variability in Gulf Stream transport is geostrophic and barotropic, we would expect ΔSSH and total transport to be correlated. We will explore this in section 4.3.1. Section 4.3.2 investigates whether satellite altimetry mostly captures spatial or temporal variability. In section 4.3.3, we examine the vertical structure of correlations between ΔSSH and Gulf Stream transport fluctuations. If the variability in transport was dominated by the first baroclinic mode, we would still expect correlation, since our Gulf Stream transport estimates exclude any flow in the opposite direction of the depth-average current by definition. ΔSSH is related to the surface geostrophic velocity through geostrophy, but wind-driven ageostrophic effects like Ekman transport may play an important role in the shallower layers. Lastly, we also consider the correlations between ΔSSH and variations in transports of waters with different properties in section 4.3.4.

4.3.1 Correlation between depth-integrated transport estimates and sea surface height

Full-depth Gulf Stream transport (or transport in the upper kilometer where the ocean is deeper than the gliders' maximum profiling depth) generally increases in the along-stream direction, but is highly variable from transect to transect (Fig. 4-3, also see Fig. 2-10 in Chapter 2). Total transport is around 32 Sv in the Florida Strait and can reach up to 120 Sv in the MAB. Consistent with a geostrophic balance, SSH generally increases in the offshore direction across the Gulf Stream (e.g., Fig. 4-

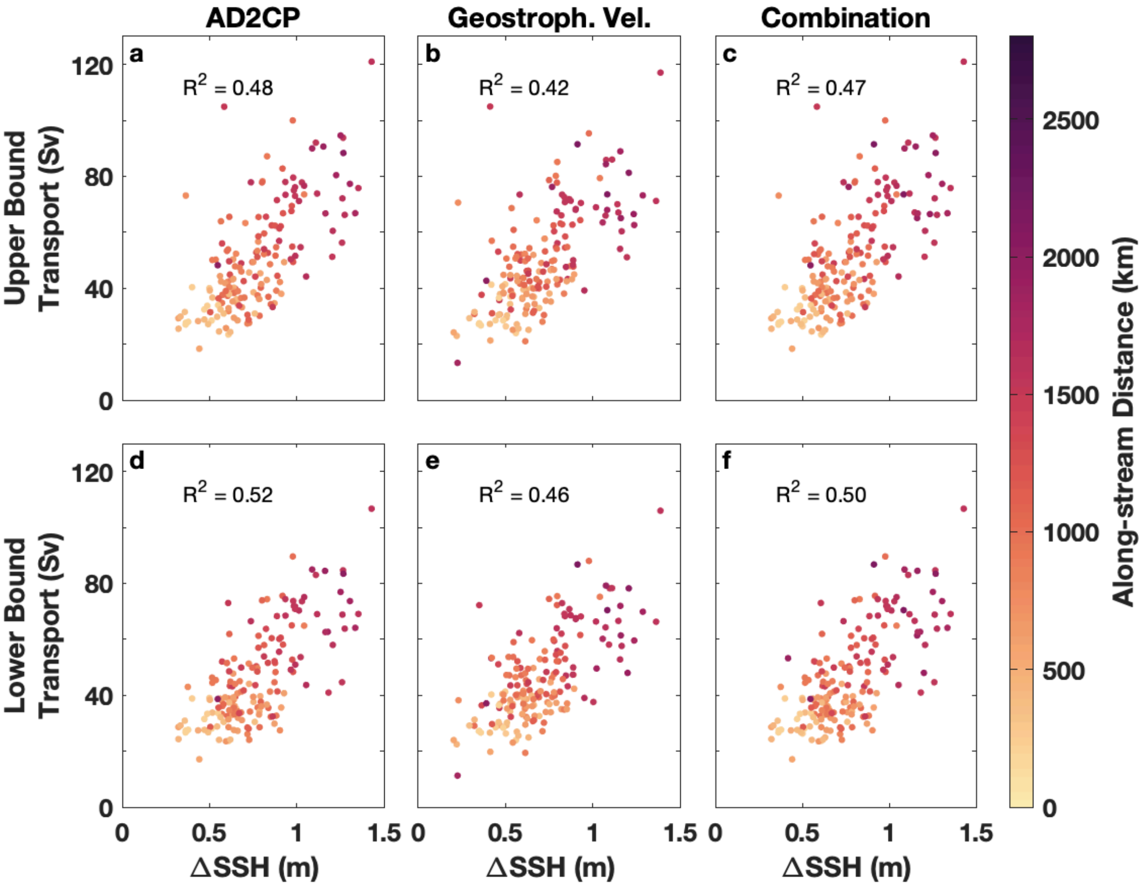

Figure 4-3: Scatter plots of the transport estimates for all the glider transects for the upper bound (a–c) and lower bound (d–f) vs the sea level difference ΔSSH along the glider transect. All dots are colored based on the along-stream distance of the corresponding transect (using the along-stream coordinate system in Fig. 4-1b). (a,d) show transport estimates from AD2CP data only, (b,e) corresponds to transport estimates from geostrophic velocities, and (c,f) use transport estimates from AD2CP data when available and geostrophic velocities otherwise. The corresponding coefficient of determination R^2 is shown in the top left of each panel.

1b). Moreover, ΔSSH also generally increases in the along-stream direction, from about 0.4 meters in the Florida Strait to almost 1.5 m in the MAB (Fig. 4-3). This indicates that, to first order,the along-stream evolution of ΔSSH reflects the along-stream increase in Gulf Stream transport. The 40-cm ΔSSH between glider transect endpoints in the Florida Strait based on the mapped ADT product is lower than the along-track estimates in Volkov et al. (2020) (on average 50 cm and 70 cm for their two satellite tracks). The satellite tracks examined by Volkov et al. (2020) and the gliders both cross the current obliquely, but the gliders cross the current more perpendicularly than does the altimeter track. In the presence of an along-stream gradient in cross-stream sea surface height difference, the impact of the oblique crossing will be less for the gliders, which helps explain the smaller range in ADT that the gliders observe.

Using a linear model, we compute the coefficient of determination R^2 between ΔSSH and full-depth transport estimates derived from AD2CP-based velocities, geostrophic velocities, or a combination thereof. Coefficients of determination are highest for transport estimates based solely on AD2CP data (Fig. 4-3a,d) for both the upper-bound and the lower-bound estimates, explaining 48% and 52% of variability, respectively. Thus, the mapped satellite altimetry product captures fluctuations in Gulf Stream transport along the entire U.S. East Coast to a similar extent as independent estimates assessing temporal variability in isolated locations using along-track altimetry products (e.g., Volkov et al. 2020) and tide gauges and bottom pressure recorders (Maul et al. 1990; Meinen et al. 2010). Worst et al. (2014) found higher correlations (capturing 77% of the variability) at the CMV *Oleander* line using the same mapped ADT product as this study, but they compared annual averages and thus looked at temporal scales that are well resolved by the gridded altimetry product. Even for annual averages, the correlation is highly dependent on the endpoints chosen to bracket the Gulf Stream (Worst et al. 2014). We observe something similar when comparing our lower- and upper-bound estimates. The lower-bound estimates are more highly correlated with ΔSSH than the upper-bound estimates, likely because they exclude curvature and corotating eddies and better capture the part of the flow that is in geostrophic balance.

Although satellite altimetry captures geostrophic velocities at the surface, the correlations with full-depth transport estimates from geostrophic velocities (Fig. 4-3b,e) are lower than for estimates using the AD2CP, generally explaining about 6% less of the variability. More discussion on the geostrophic transport estimates, their limitations and comparability with ΔSSH can be found in section 4.3.3. Combining the AD2CP transport estimates with geostrophic estimates when AD2CP data are not available as we did in Heiderich and Todd (2020) adds information from 13 additional transects (Fig. 4-3c,f), but it does not improve the correlation compared to the AD2CP-only transects, since the geostrophic velocities are less correlated with ΔSSH. In the following discussion, we will generally focus on lower-bound estimates from AD2CP data only (except for a discussion of the geostrophic transport estimates in section 4.3.3), since the coefficient of determination is highest for this combination (explaining 52% of the variability).

We also calculated correlations between Gulf Stream transport and the cross-stream difference in sea surface height using a different definition for ΔSSH: In this case, we define ΔSSH as the range in SSH across a transect (i.e., the difference between maximum and minimum SSH anywhere along the transect where SSH data are available). For some transects, extrema in SSH occur within the transect rather than at the endpoints. This is mostly the case for the upper-bound estimates that include the flow associated with corotating eddies along the margins of the Gulf Stream and for long or unusually shaped transects that capture significant along-stream variation in SSH due to the gliders' oblique crossing. We note that the range in ΔSSH across a transect captures the same amount of Gulf Stream transport variability as ΔSSH between the endpoints, and thus we will not show this metric. For both the upper and the lower bound and AD2CP-based or geostrophic-velocity-based transport estimates (or a combination thereof), the range captures about 1–4% more of the variance in transport than the endpoints, which is not a substantial difference. The range particularly improves the correlation for the transport estimates from geostrophic velocities (4%).

4.3.2 The effect of spatial vs temporal variability on correlations

Coloring the Gulf Stream transport estimates and corresponding sea surface height difference based their along-stream distance using the SSH-based coordinate system reveals that there is a strong along-stream trend (Fig. 4-3). This raises the question whether satellite altimetry mostly captures spatial variability and how much temporal variability it reflects.

Satellites and underwater gliders capture different spatial and temporal scales. Our gliders do not provide time series of transport in any particular location, but rather transport estimates collected over time scales of about a week (the time that it takes a glider to complete a Gulf Stream crossing) that are spread all over the Gulf Stream. Since the gliders are moving with respect to the water, we cannot completely separate spatial and temporal variability. An individual glider transect mostly captures local variability in transport, where "local" refers to spatial scales of $\mathcal{O}(200)$ km (the typical along-stream extent of a glider transect, see Chapter 2) and time scales of about a week (the typical duration of a glider crossing). Since the collection of transects spans the entire U.S. East Coast, the gliders also provide

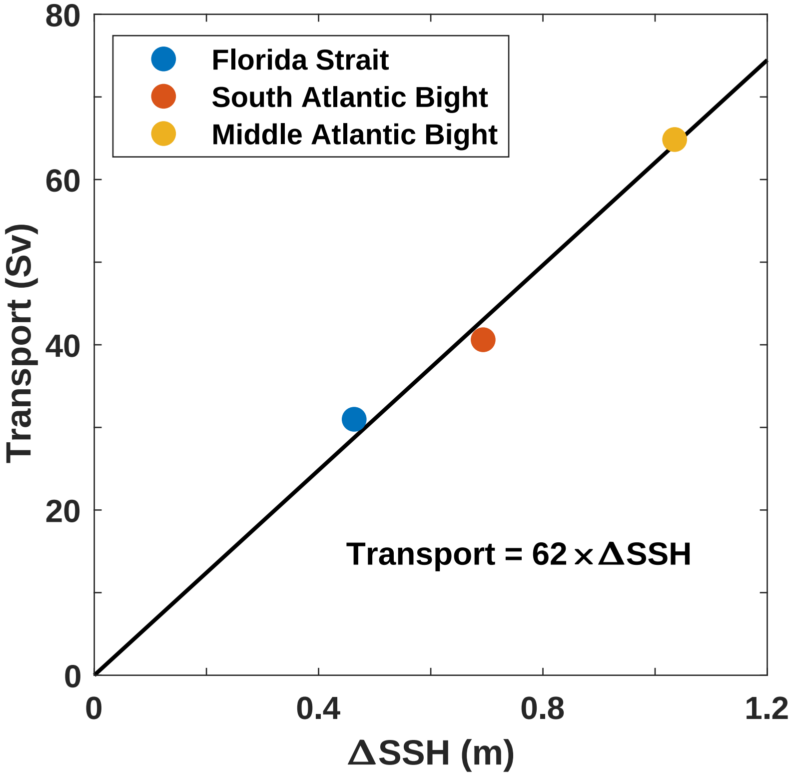

Figure 4-4: Mean transport for all the glider transects in a given region vs mean ΔSSH across the glider transects in this region. See legend for regions. The mean transports are based on the lower-bound estimates of transport from AD2CP data only. The black line is a trend line forced to go through zero; the corresponding equation is listed in the lower right.

information about the along-stream variation in Gulf Stream transport (spatial extent of $\mathcal{O}(2000)$ km). It takes a glider approximately the same time to cross the Gulf Stream as it takes a Jason or Topex/Poseidon satellite to complete a repeat cycle. The other satellites with repeat cycles of up to a month might entirely miss a glider crossing and any short-term transport fluctuations. Since the effective temporal resolution of the gridded altimetry product is about a month (Chelton et al. 2019), we expect the satellites to capture more of the spatial (i.e., along-axis) variability than short-term temporal variability.

In order evaluate the relative contributions of spatial and temporal variability to the correlations in Fig. 4-3, we first assess the along-stream spatial trend (Fig. 4-4). Mean transport estimates and the corresponding mean sea surface height difference ΔSSH for transects in three individual subregions (the Florida Strait, the South Atlantic Bight, and the Middle Atlantic Bight) show a clear along-stream trend. This indicates that the variability captured by the gridded satellite altimetry product is likely dominated by spatial variability, as already expected from Fig. 4-3. Fitting a linear model that is forced to go through zero to the regional mean estimates allows us to express the along-stream increase in transport as a function of ΔSSH.

To assess how much of the temporal variability in the glider-based transport estimates is reflected in satellite altimetry, we remove the along-stream spatial trends in both the transport and the ΔSSH estimates (Fig. 4-5). For the transport estimates, we simply subtract the Gaussian-weighted mean transport derived in Chapter 2 at the location of the respective transect. Since we are focusing on the lower-bound transport estimates only based on AD2CP data in the following (the combination with the highest correlation), we are subtracting the corresponding Gaussian-weighted mean that is based on the lower-bound transport estimates from glider AD2CPs only. This keeps comparisons consistent, but it also means the weighted mean in this chapter is slightly different from the red line shown in Fig. 2-10 in Chapter 2. Differences between the two weighted means are very small, even though we added more recent glider AD2CP-based transport estimates and excluded transport estimates based on geostrophic velocities and from Line W here. For ΔSSH, we also subtract the weighted

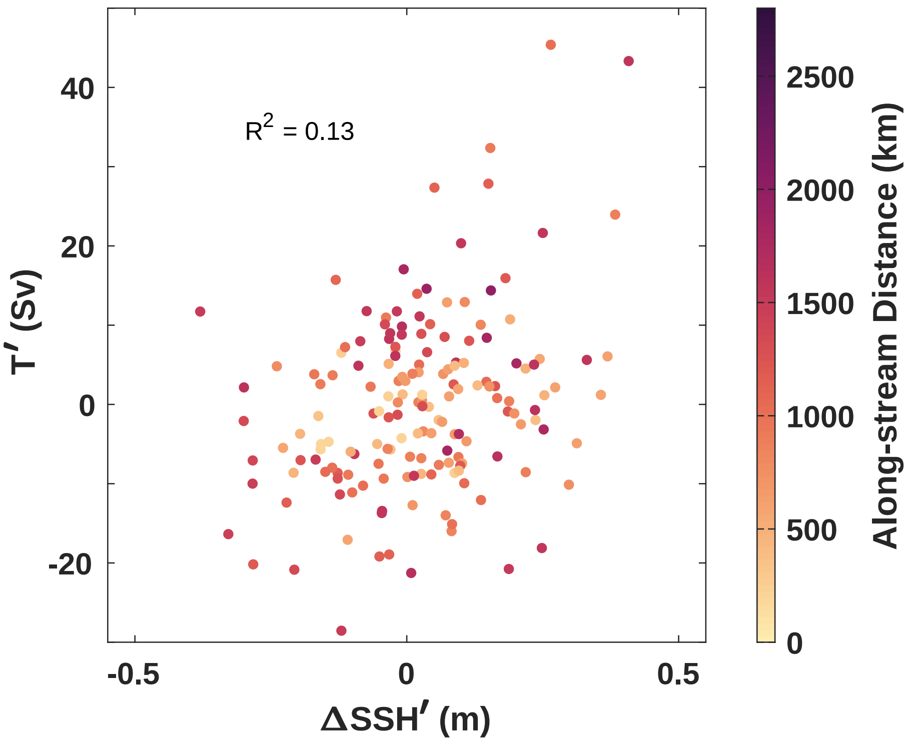

Figure 4-5: Scatter plot as in Fig. 4-3d, but for deviations in transport T′ and sea surface height ΔSSH′ after the removal of mean along-stream trends. The corresponding coefficient of determination R^2 is shown in the top left.

mean transport at the transect locations, but divided by the slope of the linear model describing the relationship between ΔSSH and transport in Fig. 4-4. After removing the large-scale spatial trends, the correlation between deviations in transport (T′) and sea surface height difference (ΔSSH′) drops substantially. For the AD2CP-only-based lower-bound transport estimates, only about 13% of the variance is explained. Due to their low temporal resolution of approximately one month, the gridded altimetry product barely captures the short-term transport variability in the glider observations.

Since we only removed a mean large-scale spatial trend, the remaining estimates contain both local spatial variability and temporal variability. We investigate whether the remaining variability captured by satellite altimetry is localized in smaller dynamically distinct regions with along-stream extents of 1000 km or less. Correlations are similarly low when the deviations in transport (T′) and sea surface height difference (ΔSSH′) are compared in following individual subregions: the Florida Strait, the

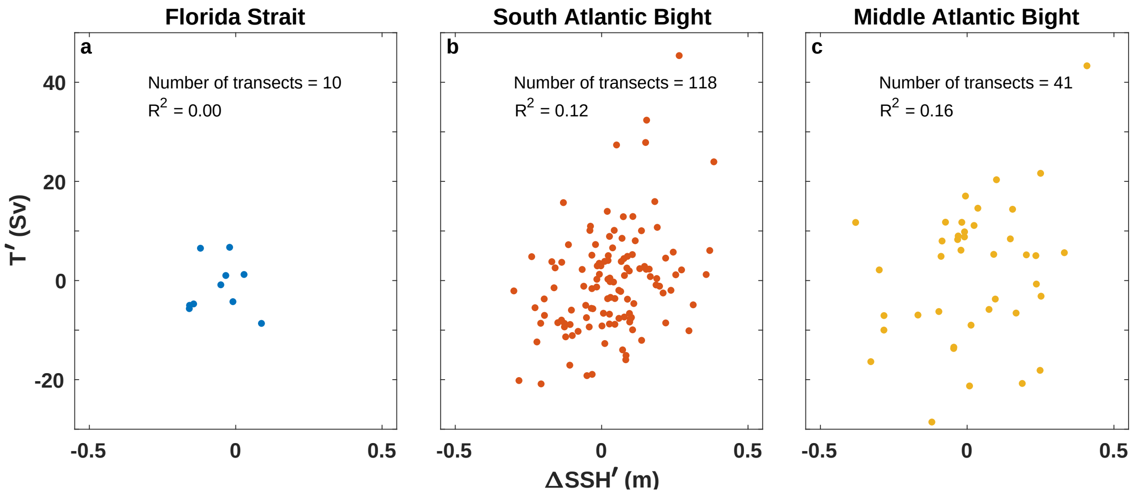

Figure 4-6: As in Fig. 4-5, but separating the transects into different regions: (a) the Florida Strait, (b) the South Atlantic Bight, and (c) the Middle Atlantic Bight. The corresponding coefficient of determination R^2 is shown in each panel.

South Atlantic Bight, and the Middle Atlantic Bight (Fig. 4-6). In the Florida Strait, where only 10 transects with AD2CP data exist, all of which had to be truncated due to the lack of SSH data on the inshore edge, ΔSSH′ and T′ are uncorrelated. For the South Atlantic Bight and the Middle Atlantic Bight, the coefficients of determination are similar and explain about 12% and 16% of the variance, respectively. There are more transects with AD2CP data in the SAB compared to the MAB (118 vs 41). In individual subregions, both short-term temporal variability and local spatial variability are high. They are captured by the gliders to the extent of the scales that the gliders resolve (see above), but mostly missed by the mapped altimetry product.

In summary, the gridded altimetry product captures variability in Gulf Stream transport along the U.S. East Coast reasonably well (about 50% of the variance), but most of that is dominated by the large-scale spatial variability. While the along-stream evolution is captured, local and/or short-term temporal variations are not represented adequately (only 10%–15% of the variance). For the remainder of this chapter, we will return to computing correlations for full transport and ΔSSH estimates without the removal of along-stream trends (i.e., not the deviations T′ and ΔSSH′), keeping in mind that any subsequent analyses are mostly representative of large-scale spatial trends.

4.3.3 Correlations between transport per unit depth and sea surface height

That satellite altimetry captures about 50% of the fluctuations in full-depth transport estimates from gliders already gives us an indication that subsurface Gulf Stream velocities are correlated with the surface velocities. The glider observations also allow us to investigate the correlation between ΔSSH and Gulf Stream transport as a function of depth. We calculate the coefficient of determination between ΔSSH and Gulf Stream transport per unit depth for each 10-m vertical bin of the glider observations (i.e., dividing the cross-stream integrated T_{ij} by 10 m, the vertical extent of each bin).

The correlation between ΔSSH and the surface transport per unit depth estimate from geostrophic velocities is higher than with the AD2CP-based transport estimates (Fig. 4-7). ΔSSH captures 39% of the variance in surface geostrophic transport es-

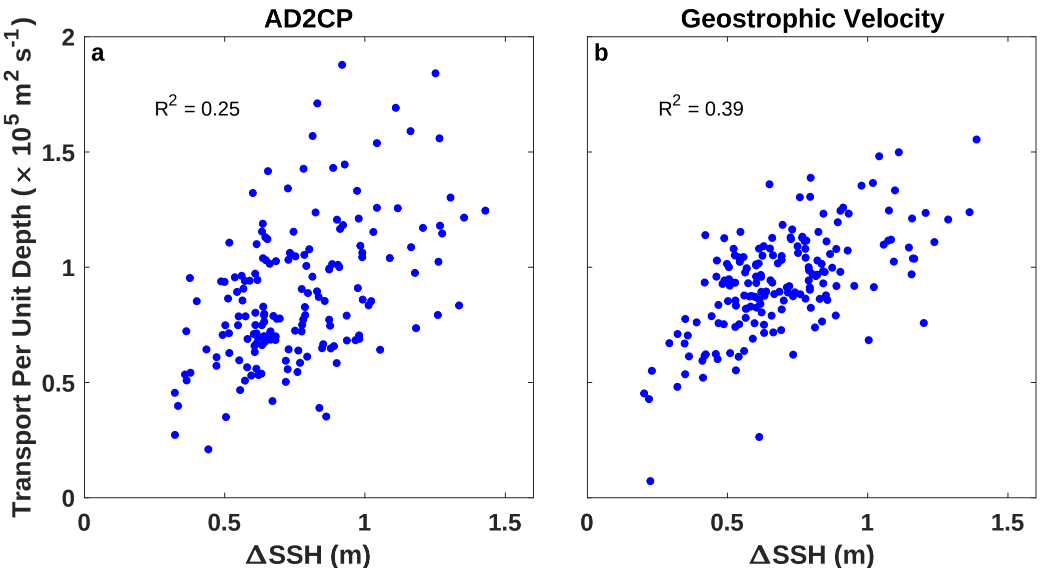

Figure 4-7: Scatter plots of the lower-bound surface layer transport estimates for the glider transects vs the sea level difference ΔSSH along the glider transect. The surface layer estimate describes the transport in the uppermost 10-m bin of the glider observations (from 5 to 15 m depth). (a) shows transport estimates from AD2CP data only, and (b) shows transport estimates from geostrophic velocities only. The corresponding coefficient of determination R^2 is shown in the top left of each panel.

timates, but only 25% of the variance in AD2CP-based surface transport estimates. The "surface" for the glider observations refers to the upper-most bin between depths of 5 and 15 m. At the surface, ageostrophic effects due to wind (e.g., Ekman transport) play an important role and are captured by the gliders' AD2CPs and likely explain the low correlation. Though ΔSSH is related to the surface geostrophic velocity, it might not be entirely comparable with our geostrophic velocity-based transport estimates, which might explain the observed fairly low correlation. Our geostrophic velocity estimates also contain ageostrophic components: the geostrophic shear is referenced to the depth-average current, which includes all ageostrophic components. Other ageostrophic effects (e.g., vertical heave by internal waves that influences the thermal wind estimate) are mostly filtered out by the objective mapping procedure used to estimate the geostrophic velocities (Todd et al. 2011, 2016; Rudnick et al. 2017). Furthermore, the relatively low correlation between ΔSSH and glider-based surface geostrophic velocity estimates may be related to uncertainties in our geostrophic velocity estimates, including how accurately we can estimate the density gradient. Note that we always miss some geostrophic transport along the edges of the Stream due to the effects of objective mapping, which shrink the transect. Consequently, we adjust the distance over which ΔSSH is computed for comparability. Even though the correlations between ΔSSH and glider-based geostrophic transport estimates are therefore internally consistent (Fig. 4-7b), it complicates comparison with the correlations for the AD2CP-based transport estimates (Fig. 4-7a) since the transports were computed over transects of different lengths.

Below the surface, the correlation between ΔSSH and geostrophic transport estimates in each layer decreases (not shown). In contrast, the coefficients of determination for AD2CP-based transports in each layer increase below the surface (gray line in Fig. 4-8a). Below 250 m depth, where ageostrophic effects due to wind are less important, R^2 is relatively constant with depth (around 0.4). This agrees with an equivalent barotropic current where the flow is in the same direction with depth (Neumann 1960) and may explain why ΔSSH and the corresponding surface geostrophic velocities explain as much of the transport variability as they do.

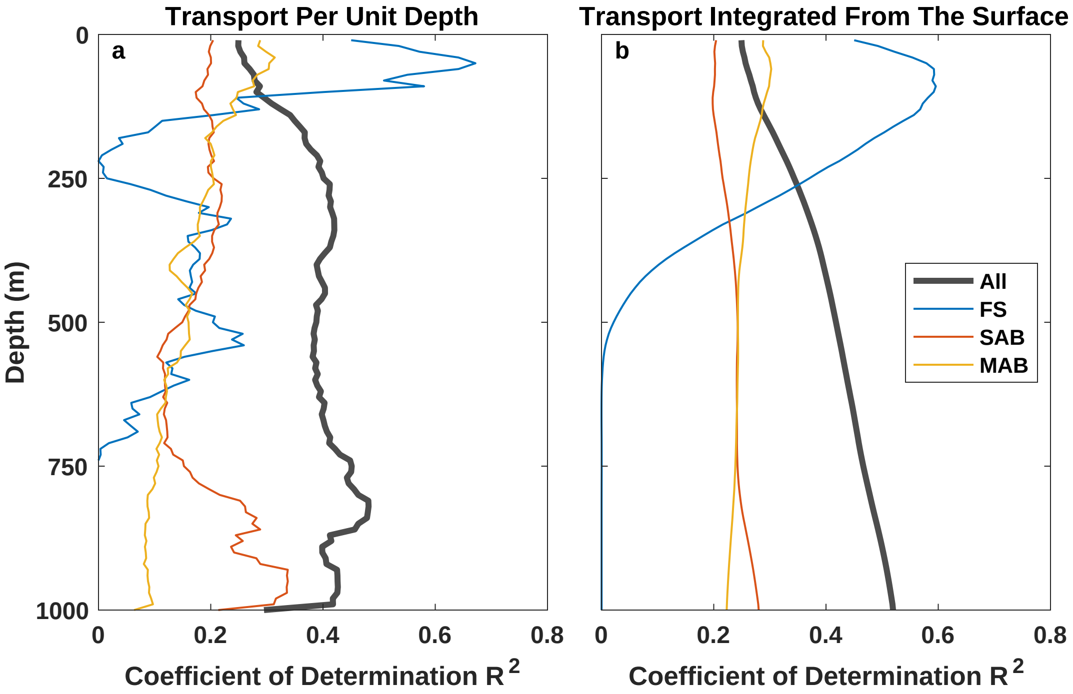

Figure 4-8: The coefficient of determination R^2 between the lower-bound estimate of Gulf Stream layer transport from AD2CP data only and the sea surface height difference ΔSSH as a function of depth: (a) using transport in each 10-m depth layer, and (b) using transport integrated from the surface to the given depth. The coefficients of determination for all transects are shown in gray, while the colors represent R^2 in the three different dynamical regions: the Florida Strait (FS), the South Atlantic Bight (SAB) and the Middle Atlantic Bight (MAB), see legend.

We also calculate the coefficient of determination for transports per unit depth in the different dynamical regions (colored lines in Fig. 4-8a). For the Florida Strait and South Atlantic Bight, only a few profiles reach to the deepest depths, so we only calculate R^2 for the depths where at least 10 profiles are contributing. In general, the coefficient of determination is not very meaningful for the Florida Strait where only 10 transects with AD2CP data contribute. R^2 in the surface layer in the Florida is about twice as large as in the other two regions and goes to zero around 200 m depth because transport above 200 m is correlated with ΔSSH, while transport below 200 m is anti-correlated with ΔSSH (not shown). This agrees with the two layer structure of the Florida Strait observed by Meinen and Luther (2016) in lowered acoustic Doppler current profiler (LADCP) data. Below 200 m, they also found a reduction in correlation between velocities at these depths and the surface velocity. In the SAB, the coefficient of determination is fairly constant with depth, until it increases below 800 m where only the deeper profiles near Cape Hatteras contribute. At Cape Hatteras, where the Gulf Stream crosses over the Deep Western Boundary Current, greater variability and larger ranges in ΔSSH compared to the rest of the SAB are expected. The layer transport for all regions combined also shows a slight increase in R^2 around 800 m depth, possibly due to the influence of glider profiles near Cape Hatteras. In the MAB, correlations between layer transport and ΔSSH decrease slightly with depth.

The coefficient of determination R^2 between ΔSSH and transport integrated from the surface to a given depth increases with depth (gray line in Fig. 4-8b). Most ageostrophic effects like Ekman transport are stronger at the surface and therefore become less important for increasingly thicker layers that extend farther away from the surface. For the SAB and MAB, R^2 for transport integrated from the surface to a given depth is fairly constant and comparable for the two regions. As already indicated in section 4.3.2, the mapped altimetry product captures the large-scale spatial variability along the U.S. East Coast better than the local short-term variability in different dynamical regions; R^2 for all the regions combined is larger at all depths, except for at the surface in the Florida Strait and the MAB where ageostrophic effects are largest.

Since the Gulf Stream often exhibits substantial curvature, particularly in the MAB and downstream of the Charleston Bump (an underwater ridge and trough feature in the SAB; Bane and Brooks 1979; Gula et al. 2015), the cyclostrophic component of the velocity, which is related to the centrifugal acceleration acting on curved flow, may be important. We estimate a representative Gulf Stream radius of curvature for each glider transect by first computing the local radius of curvature between successive glider dives as the ratio of the along-stream distance between dives to the change in direction of the depth-average current between those dives (Todd et al. 2016) and then averaging these estimates within each individual transect. The transects exhibit both cyclonic and anti-cyclonic curvature and the radii of curvature

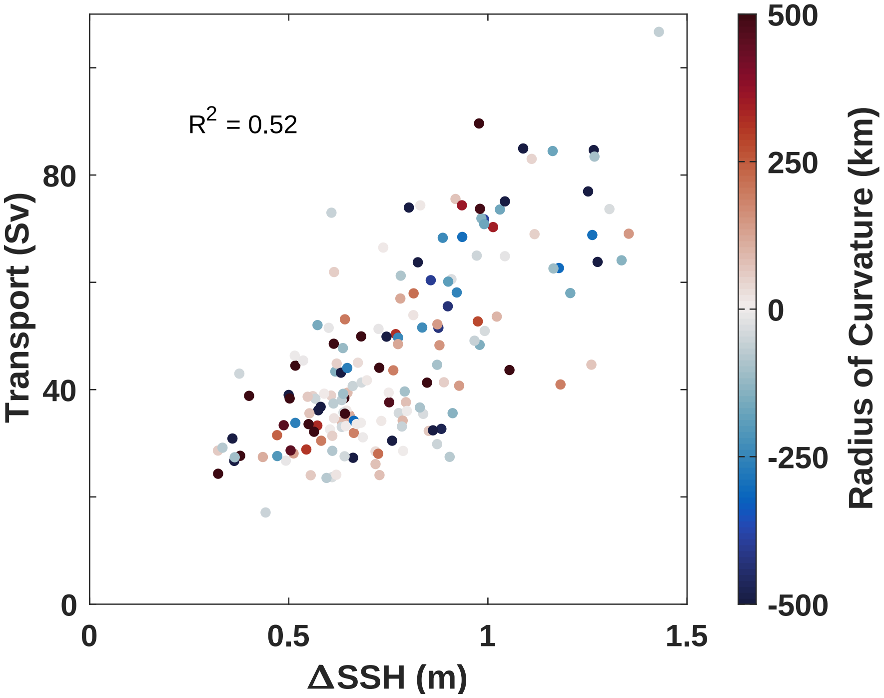

Figure 4-9: Scatter plot of the lower-bound transport estimates from AD2CP data only for all the glider transects vs the sea level difference ΔSSH along the corresponding glider transects (as in Fig. 4-3d), but colored by the mean radius of curvature for each transect. Note that some transects exceed the color scale: 39 transects have radii of curvature with absolute values larger than 500 km and are shown in the darkest colors.

span a wide range from 1 to 8000 km (Fig. 4-9), with no recognizable pattern. Radii of curvature are very large where the current exhibits essentially no curvature, and can be very small for transects where the Gulf Stream exhibits both cyclonic and anti-cyclonic curvature that is averaged out across the stream. Estimating radii of curvature is difficult and noisy. If there were a consistent pattern, we could assume a gradient wind balance rather than a geostrophic balance and examine whether the correlation of our transport estimates with ΔSSH improves.

4.3.4 Correlations for different water classes

The gliders provide concurrent observations of hydrography and velocity and thus allow us to investigate whether fluctuations in the transport of certain water classes in the Gulf Stream are correlated with ΔSSH through geostrophy. Heiderich and Todd (2020) divided Gulf Stream transport into 7 different water classes: near-surface Gulf Stream waters (SW), near-surface waters originating from the Middle Atlantic Bight shelf and the Slope Sea (MABW), thermocline waters including Salinity Maximum Water (TW), Eighteen Degree Water and related waters below the thermocline (EDW), Antarctic Intermediate Water (AAIW), upper Labrador Sea Water (uLSW), and other intermediate waters (IW). We use the same classification to calculate water class transports in each transect and compare them with ΔSSH over the transects. Coefficients of determination R^2 are only calculated for water classes observed in at least 10 transects in a given region. R^2 is highest for the subthermocline water classes (i.e., EDW, IW, uLSW) where ageostrophic effects are smaller (Fig. 4-10a), as we expect from Fig. 4-8. Satellite altimetry captures almost 50% of the variance in these water classes along the entire U.S. East Coast. Local short-term variability in the individual dynamical regions is less well represented (Fig. 4-10b–d) as seen previously in Figs. 4-6, 4-5 and 4-8. Correlations for AAIW decrease as the Gulf Stream flows northward and its signal is eroded away (yellow bars in Fig. 4-10b–d; also see

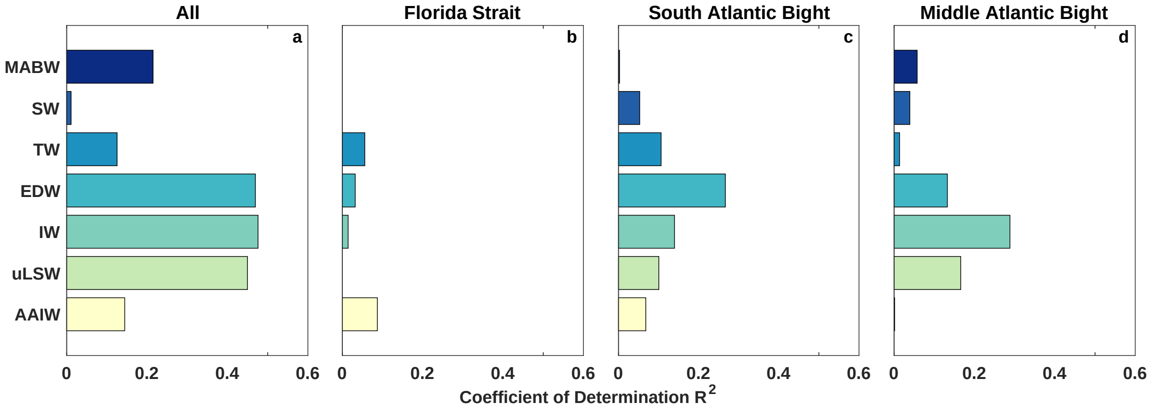

Figure 4-10: The coefficient of determination R^2 between water class transports and the sea level difference ΔSSH across the corresponding glider transect for (a) all the glider transects and in the three different dynamical regions: the Florida Strait (b), the South Atlantic Bight (c), and the Middle Atlantic Bight (d). The different water classes are as in Heiderich and Todd (2020): Middle Atlantic Bight Water (MABW), surface waters (SW), thermocline waters (TW), Eighteen Degree Water and related waters (EDW), intermediate waters (IW), upper Labrador Sea Water (uLSW), and Antarctic Intermediate Water (AAIW).

Chapter 2). Conversely, as the volume of uLSW in the Gulf Stream increases downstream through entrainment from the offshore side (see Heiderich and Todd 2020, and Chapter 3), correlations between uLSW and ΔSSH increase (light green bars in Fig. 4-10b–d). As before, correlations are highest in the MAB and not very reliable in the Florida Strait where only 10 transects contribute to the estimates. MABW is only observed in the MAB and near Cape Hatteras, whereas uLSW and SW are not encountered in the Florida Strait (or at least not often enough to be counted in the calculation of R^2, particularly for SW).

4.4 Summary

In this analysis, we have investigated how well satellite-altimetry-based estimates of cross-stream sea surface height differences represent the variance in Gulf Stream transport along the U.S. East Coast that has been measured by underwater gliders. Both transport and ΔSSH increase in the along-stream direction, indicating that geostrophy does capture the along-stream increase in Gulf Stream transport to first order. We assess the correlations between ΔSSH and transport as a function of depth, for three different dynamical regions (the Florida Strait, South Atlantic Bight, and Middle Atlantic Bight), and for different water classes following the classification in Heiderich and Todd (2020).

Correlations are highest for our lower-bound transport estimate based solely on AD2CP data. For these estimates, ΔSSH from satellite altimetry captures about 50% of the variability along the entirety of the U.S. East Coast (Fig. 4-3), most of which is large-scale spatial variability ($\mathcal{O}(2000)$ km). Removing the along-stream trends reveals that the satellites only capture about 10%–15% of the local and/or short-term temporal variability over the whole domain (Fig. 4-5), as well as in the smaller subregions of the Florida Strait, South Atlantic Bight, and Middle Atlantic Bight (Fig. 4-6). This is due to the difference in the temporal resolution of the observations: gliders observe processes on time scales of about a week, whereas the gridded altimetry product has a $\mathcal{O}(1)$ month temporal resolution. That ΔSSH and depth-integrated transport fluctuations are correlated over the scale of the entire U.S. East Coast is reflective of our result in Chapter 2 that the along-stream increase in transport is barotropic (see Fig. 2-11).

Fluctuations in subsurface Gulf Stream velocities are at least somewhat correlated with fluctuations in surface velocities. At the surface, transport estimates from geostrophic velocities are more highly correlated with ΔSSH than AD2CP-based surface transport estimates (Fig. 4-7). In general, correlations between ΔSSH and transport per unit depth increase below 250 m depth since ageostrophic effects (e.g., wind-driven Ekman transport) are stronger at the surface. When comparing ΔSSH to transport integrated from the surface, correlations increase with depth because ageostrophic effects that are mainly found at the surface contribute a smaller fraction of the transport (Fig. 4-8). Consequently, the variability in water class transport is captured best by satellite altimetry for the water classes below the thermocline (i.e., Eighteen Degree Water, upper Labrador Sea Water, and other intermediate waters; Fig. 4-10).

More detailed investigations of how good the geostrophic velocity estimates are remain, especially since the geostrophic transects miss transport along the edges due to the objective mapping. For individual transects, the differences in geostrophic transports compared to AD2CP-based transport estimates can be quite large, but they capture the same mean along-stream evolution (not shown, calculated in response to a reviewer question on Heiderich and Todd (2020), i.e. Chapter 2). Moreover, further studies on the effects of estimating ΔSSH along transects that are oblique with respect to the Gulf Stream axis (as is the case for both the gliders and the satellite tracks in the Florida Strait) would be beneficial, since geostrophic velocities estimates from ΔSSH would be perpendicular to the line connecting the two endpoints of this transect. To assess this, one could compute SSH on either side of the Gulf Stream (i.e., parallel to the Gulf Stream axis) and average it over the along-stream distance that the glider occupied during each oblique crossing.

Considering that gridded satellite altimetry captures about half of the variability in upper 1000-m Gulf Stream transport along the U.S. East Coast, it may be possible to develop an SSH-only-based metric to monitor Gulf Stream transport over large scales and on shorter time scales than is feasible using in situ platforms. However, choosing the endpoints over which the sea level difference should be computed will require careful consideration, as will estimates of the uncertainty in transport estimates from SSH over large spatial scales. Since half of the variability in Gulf Stream transport (and even more at smaller spatial scales) is not captured by satellite altimetry data, persistent in situ measurement by platforms like the underwater gliders used here will remain important to monitoring the Gulf Stream.

Chapter 5

Conclusions

This thesis explores the along-stream evolution of the Gulf Stream in terms of volume transport and water characteristics using a large data set collected by underwater gliders in combination with other observations. Chapter 2 presents an overview of Gulf Stream volume transport and its water class constituents, while Chapter 3 investigates the mechanisms involved in the erosion of one of those water classes (namely Antarctic Intermediate Water). Chapter 4 examines how well the observed variability in Gulf Stream transport is captured by satellite altimetry. All of these chapters are connected through the question of how the Gulf Stream evolves as it flow through different dynamical regimes along the U.S. East Coast and how these regimes affect its transport and water properties. This concluding section synthesizes the primary findings and contributions of the chapters in this thesis (Section 5.1) and discusses their implications, as well as any open questions that arise and potential future research directions (Section 5.2).

5.1 Contributions

Chapter 2 revisits the well-known along-stream increase in Gulf Stream volume transport through a novel large data set of finescale, subsurface observations of hydrography and velocity collected by autonomous underwater gliders in combination with shipboard measurements along Line W. The main contributions in Chapter 2 are:

- A detailed characterization of the time-mean along-stream evolution of Gulf Stream volume transport in the upper kilometer of the ocean between Florida and New England that fills in large spatial gaps between existing time series of Gulf Stream transport.

- An examination of the water classes that contribute to the along-stream increase in Gulf Stream volume transport through entrainment.

We derive upper- and lower-bound estimates of Gulf Stream transport from each cross–Gulf Stream transect to assess the effects of corotating eddies and curvature on Gulf Stream transport. The observations confirm the long established along-stream increase in volume transport, yet they also reveal high transect-to-transect variability at similar along-stream locations. Waters are divided into seven classes based on their potential temperature and salinity properties, revealing that most of the increase in Gulf Stream volume transport above 1000 m is due to the entrainment of subthermocline waters including Eighteen Degree Water, upper Labrador Sea Water, and other intermediate waters. We also show that the volume transport of Antarctic Intermediate Water within the Gulf Stream diminishes as the flow progresses downstream from the Florida Strait.

Chapter 3 delves into the mechanisms contributing to the poleward erosion of Antarctic Intermediate Water and the entrainment of upper Labrador Sea Water into the Gulf Stream far south of Cape Hatteras found in Chapter 2. We compute three-dimensional fields of mean and eddy salt fluxes from the glider observations. Those fluxes are then integrated over the surfaces of control volumes that we choose to enclose the Antarctic Intermediate Water. The primary findings of Chapter 3 include:

- The low salinity signature of Antarctic Intermediate Water in potential temperature–salinity (θ–S) space is eroded in the Gulf Stream between the Florida Strait and Cape Hatteras through both lateral stirring and vertical mixing with different processes dominating in different locations along the Blake Plateau.
- Variable flow allows upper Labrador Sea Water to cross f/H contours and flow over the relatively shallow Blake Plateau just north of the Bahamas, where it

is entrained into the Gulf Stream as shown in Chapter 2 and contributes to the erosion of Antarctic Intermediate Water due to its relatively higher salinity at similar densities.

Returning to the glider-based estimates of Gulf Stream volume transport developed in Chapter 2, Chapter 4 assesses how well satellite-altimetry-based estimates of cross-stream sea surface height differences (ΔSSH) capture the transport variability observed by the gliders. The central conclusions in Chapter 4 are:

- The gridded and objectively mapped satellite altimetry product captures only about 50% of the variability observed in glider-based transport estimates along the entire U.S. East Coast. In individual subregions where local and/or short-term temporal variability is high, ΔSSH explains much less of the variance in transport.

- Correlations between ΔSSH and transport per unit depth are higher at depths where ageostrophic effects are less important. Altimetry best captures the variability of transport for waters below the main thermocline (i.e., Eighteen Degree Water, upper Labrador Sea Water, and other intermediate waters).

- Though previous studies have shown that along-track satellite data can be used to derive Gulf Stream transport in isolated locations at time scales of several weeks or longer, creating a satellite-based metric that captures the along-stream variability of Gulf Stream transport is only feasible to a certain extent for large scales and cannot replace in situ observational platforms.

5.2 Implications, open questions, and future directions

The large Gulf Stream glider field program that provides the main observational basis for this thesis provides uniquely detailed insights into the along-stream evolution of the Gulf Stream. Acting as a platform that connects observations in the shelf regions and the open ocean as part of the Global Ocean Observing System, autonomous underwater gliders are particularly well suited to monitor the upper kilometer of western boundary currents, improving the coverage of observations along ocean boundaries (Davis et al. 2012; Rainville et al. 2013; Rudnick et al. 2013; Schaeffer and Roughan 2015; Schönau et al. 2015; Todd et al. 2016; Krug et al. 2017; Todd 2017). They provide finescale observations for months at a time and can continue sampling during hurricanes and other severe weather events when shipboard operations are not possible (Todd et al. 2018). Since deployments and recoveries only require day trips on small vessels, the glider observations are cost effective compared to traditional shipboard sampling. Hopefully this valuable Gulf Stream glider field program will be continued into the future, so that it can be used to identify and quantify potential changes in Gulf Stream behavior that are likely to occur due to anthropogenic climate change (e.g., IPCC 2013, and references therein). Several studies suggest that the Gulf Stream may already be changing (e.g., Ezer et al. 2013; Andres 2016; Piecuch 2020; Caesar et al. 2021), emphasizing the need for large data sets to provide a robust climatological reference baseline to compare future changes to and that can help us understand the present dynamics, variability, and structure of western boundary currents. At its current size, the data set allows estimation of time-mean properties (e.g., Chapters 2 and 3), variability with respect to that mean (Chapter 3), and transect-to-transect variability in the along-stream direction (Chapters 2 and 4). More observations are needed to assess the climatological seasonal variability and variability on interannual time scales in the Gulf Stream.

Many questions remain about the pathways of the different water masses and their variability or persistence. Though Chapters 2 and 3 have established where and how water masses including upper Labrador Sea Water or Antarctic Intermediate Water become entrained or are eroded, many details remain unknown because the gliders only measure horizontal fluxes. Analysis of numerical simulations, particularly those constrained to match the glider observations via data assimilation, could shine more light on vertical fluxes, the pathways of other water masses, Gulf Stream structure and variability below the depths where gliders cannot measure (below 1000 m), and vertical diffusivities as outlined in Chapter 3.

Satellites provide broad scale observations of the surface ocean over relatively short time scales as discussed in Chapter 4. Though along-track altimetry has proven useful to track Gulf Stream transport in isolated locations, the gridded and mapped products miss much of the local temporal variability because satellites have repeat periods on the order of 10 days or larger (Chapter 4). Further work is needed to determine the degree to which remote sensing of the sea surface can be used to fill spatial or temporal gaps in monitoring Gulf Stream transport with in situ platforms. Questions remain about how to define the offshore boundary of the Gulf Stream from satellite observations, especially due to the tilted core of the current, eddies, and flow curvature.

The glider data set provides ample opportunities for future studies. Among other potential topics, it would be interesting to have a more detailed look at the exchange between the Gulf Stream and the DWBC at Cape Hatteras, the processes controlling the stability and structure of the benthic front between AAIW and uLSW on the southern Blake Plateau, and horizontal momentum fluxes in the Gulf Stream.

References

Andres, M., 2016: On the recent destabilization of the Gulf Stream path downstream of Cape Hatteras. *Geophysical Research Letters*, **43 (18)**, 9836 – 9842, doi: 10.1002/2016GL069966.

Andres, M., K. A. Donohue, and J. M. Toole, 2020: The Gulf Stream's path and time-averaged velocity structure and transport at 68.5°W and 70.3°W. *Deep Sea Research Part I: Oceanographic Research Papers*, **156**, 103 179, doi: 10.1016/j.dsr.2019.103179.

Andres, M., M. Muglia, F. Bahr, and J. Bane, 2018: Continuous Flow of Upper Labrador Sea Water around Cape Hatteras. *Scientific Reports*, **8 (1)**, 4494, doi: 10.1038/s41598-018-22758-z.

Androulidakis, Y., V. Kourafalou, M. Le Hénaff, H. Kang, N. Ntaganou, and C. Hu, 2020: Gulf Stream evolution through the Straits of Florida: the role of eddies and upwelling near Cuba. *Ocean Dynamics*, **70 (8)**, 1005 – 1032, doi: 10.1007/s10236-020-01381-5.

Arakawa, A., and V. R. Lamb, 1977: Computational design of the basic dynamical processes of the UCLA general circulation model. *General circulation models of the atmosphere*, **17 (Supplement C)**, 173 – 265.

Atkinson, L. P., 1983: Distribution of Antarctic intermediate water over the Blake Plateau. *Journal of Geophysical Research: Oceans*, **88 (C8)**, 4699 – 4704, doi: 10.1029/JC088iC08p04699.

Bane, J. M., Jr., and D. A. Brooks, 1979: Gulf Stream meanders along the continental margin from the Florida Straits to Cape Hatteras. *Geophysical Research Letters*, **6 (4)**, 280 – 282, doi: 10.1029/GL006i004p00280.

Bane, J. M., Jr., D. A. Brooks, and K. R. Lorenson, 1981: Synoptic Observations of the Three-Dimensional Structure and Propagation of Gulf Stream Meanders Along the Carolina Continental Margin. *Journal of Geophysical Research*, **86 (C7)**, 6411 – 6425, doi: 10.1029/JC086iC07p06411.

Bane, J. M., Jr., and W. K. Dewar, 1988: Gulf Stream Bimodality and Variability Downstream of the Charleston Bump. *Journal of Geophysical Research*, **93 (C6)**, 6695 – 6710, doi: 10.1029/JC093iC06p06695.

Baringer, M. O'N., and J. C. Larsen, 2001: Sixteen years of Florida Current Transport at 27°N. *Geophysical Research Letters*, **28 (16)**, 3179 – 3182, doi: 10.1029/2001GL013246.

Beal, L. M., and S. Elipot, 2016: Broadening not strengthening of the Agulhas Current since the early 1990s. *Nature*, **540**, 570 – 573, doi: 10.1038/nature19853.

Blaha, J. P., 1984: Fluctuations of Monthly Sea Level as Related to the Intensity of the Gulf Stream From Key West to Norfolk. *Journal of Geophysical Research*, **89 (C5)**, 8033 – 8042, doi: 10.1029/JC089iC05p08033.

Bower, A. S., and H. D. Hunt, 2000a: Lagrangian Observations of the Deep Western Boundary Current in the North Atlantic Ocean. Part I: Large-Scale Pathways and Spreading Rates. *Journal of Physical Oceanography*, **30 (5)**, 764 – 783, doi: 10.1175/1520-0485(2000)030<0764:LOOTDW>2.0.CO;2.

Bower, A. S., and H. D. Hunt, 2000b: Lagrangian Observations of the Deep Western Boundary Current in the North Atlantic Ocean. Part II: The Gulf Stream–Deep Western Boundary Current Crossover. *Journal of Physical Oceanography*, **30 (5)**, 784 – 804, doi: 10.1175/1520-0485(2000)030<0784:LOOTDW>2.0.CO;2.

Bretherton, F. P., R. E. Davis, and C. B. Fandry, 1976: A technique for objective analysis and design of oceanographic experiments applied to MODE-73. *Deep Sea Research and Oceanographic Abstracts*, **23 (7)**, 559 – 582, doi: 10.1016/0011-7471(76)90001-2.

Brooks, D. A., and J. M. Bane, Jr., 1983: Gulf Stream Meanders off North Carolina During Winter and Summer 1979. *Journal of Geophysical Research*, **88 (C8)**, 4633 – 4650, doi: 10.1029/JC088iC08p04633.

Brooks, I. H., and P. P. Niiler, 1977: Energetics of the Florida Current. *Journal of Marine Research*, **35 (1)**, 163 – 191.

Caesar, L., G. D. McCarthy, D. J. R. Thornalley, N. Cahill, and S. Rahmstorf, 2021: Current Atlantic Meridional Overturning Circulation weakest in last millennium. *Nature Geoscience*, **14 (3)**, 118 – 120, doi: 10.1038/s41561-021-00699-z.

Charney, J. G., 1955: The Gulf Stream as an inertial boundary layer. *Proceedings of the National Academy of Sciences of the United States of America*, **41 (10)**, 731 – 740, doi: 10.1073/pnas.41.10.731.

Chelton, D. B., M. G. Schlax, and R. M. Samelson, 2011: Global observations of nonlinear mesoscale eddies. *Progress in Oceanography*, **91 (2)**, 167 – 216, doi: 10.1016/j.pocean.2011.01.002.

Chelton, D. B., M. G. Schlax, R. M. Samelson, J. T. Farrar, M. J. Molemaker, J. C. McWilliams, and J. Gula, 2019: Prospects for future satellite estimation of small-scale variability of ocean surface velocity and vorticity. *Progress in Oceanography*, **173**, 256 – 350, doi: h10.1016/j.pocean.2018.10.012.

Cole, S. T., C. Wortham, E. Kunze, and W. B. Owens, 2015: Eddy stirring and horizontal diffusivity from Argo float observations: Geographic and depth variability. *Geophysical Research Letters*, **42 (10)**, 3989 – 3997, doi: 10.1002/2015GL063827.

Cornillon, P., 1986: The Effect of the New England Seamounts on Gulf Stream Meandering as Observed from Satellite IR Imagery. *Journal of Physical Oceanography*, **16 (2)**, 386 – 389, doi: 10.1175/1520-0485(1986)016<0386:TEOTNE>2.0.CO;2.

Csanady, G. T., and P. Hamilton, 1988: Circulation of slopewater. *Continental Shelf Research*, **8 (5-7)**, 565 – 624, doi: 10.1016/0278-4343(88)90068-4.

Cunningham, S. A., and Coauthors, 2007: Temporal Variability of the Atlantic Meridional Overturning Circulation at 26.5°N. *Science*, **317 (5840)**, 935 – 938, doi: 10.1126/science.1141304.

Davis, R. E., C. C. Eriksen, and C. P. Jones, 2002: Autonomous bouyancy-driven underwater gliders. *Technology and Applications of Autonomous Underwater Vehicles*, G. Griffiths, Ed., Taylor & Francis, 37 – 58, doi: 10.1201/9780203522301.ch3.

Davis, R. E., W. S. Kessler, and J. T. Sherman, 2012: Gliders Measure Western Boundary Current Transport from the South Pacific to the Equator. *Journal of Physical Oceanography*, **42 (11)**, 2001 – 2013, doi: 10.1175/JPO-D-12-022.1.

Ezer, T., 2016: Can the Gulf Stream induce coherent short-term fluctuations in sea level along the US East Coast? A modeling study. *Ocean Dynamics*, **66 (2)**, 207 – 220, doi: 10.1007/s10236-016-0928-0.

Ezer, T., L. P. Atkinson, W. B. Corlett, and J. L. Blanco, 2013: Gulf Stream's induced sea level rise and variability along the U.S. mid-Atlantic coast. *Journal of Geophysical Research: Oceans*, **118 (2)**, 685 – 697, doi: 10.1002/jgrc.20091.

Ezer, T., L. P. Atkinson, and R. Tuleya, 2017: Observations and operational model simulations reveal the impact of Hurricane Matthew (2016) on the Gulf Stream and coastal sea level. *Dynamics of Atmospheres and Oceans*, **80 (Supplement C)**, 124 – 138, doi: https://doi.org/10.1016/j.dynatmoce.2017.10.006.

Flagg, C. N., M. Dunn, D.-P. Wang, H. T. Rossby, and R. L. Benway, 2006: A study of the currents of the outer shelf and upper slope from a decade of shipboard ADCP observations in the Middle Atlantic Bight. *Journal of Geophysical Research: Oceans*, **111 (C6)**, C06003, doi: 10.1029/2005JC003116.

Fofonoff, N. P., 1954: Steady flow in a frictionless homogeneous ocean. *Journal of Marine Research*, **13**, 254 – 262.

Ford, W. L., J. R. Longard, and R. E. Banks, 1952: On the nature, occurrence and origin of cold low salinity water along the edge of the Gulf Stream. *Journal of Marine Research*, **11**, 281 – 293.

Franklin, B., 1786: A Letter from Dr. Benjamin Franklin, to Mr. Alphonsus le Roy, Member of Several Academies, at Paris. Containing Sundry Maritime Observations. *Transactions of the American Philosophical Society*, **2**, 294–329, URL `http://www.jstor.org/stable/1005200`.

Fratantoni, P. S., T. N. Lee, G. P. Podesta, and F. Muller-Karger, 1998: The influence of Loop Current perturbations on the formation and evolution of Tortugas eddies in the southern Straits of Florida. *Journal of Geophysical Research: Oceans*, **103 (C11)**, 24 759 – 24 779, doi: 10.1029/98JC02147.

Fu, L.-L., and A. Cazenave, 2001: *Satellite Altimetry and Earth Sciences: a Handbook of Techniques and Applications*, International Geophysics Series, Vol. 69. Academic Press, San Diego, CA, 463 pp.

Fu, L.-L., and C. Ubelmann, 2014: On the Transition from Profile Altimeter to Swath Altimeter for Observing Global Ocean Surface Topography. *Journal of Atmospheric and Oceanic Technology*, **31 (2)**, 560 – 568, doi: 10.1175/JTECH-D-13-00109.1.

Fuglister, F. C., and A. D. Voorhis, 1965: A New Method of Tracking the Gulf Stream. *Limnology and Oceanography*, **10 (Suppl.)**, R115 – R124, doi: 10.4319/lo.1965.10.suppl2.r115.

Gangopadhyay, A., G. Gawarkiewicz, E. N. S. Silva, M. Monim, and J. Clark, 2019: An Observed Regime Shift in the Formation of Warm Core Rings from the Gulf Stream. *Scientific Reports*, **9 (1)**, 12 319, doi: 10.1038/s41598-019-48661-9.

Gatz, D. F., and L. Smith, 1995: The standard error of a weighted mean concentration–I. Bootstrapping vs other methods. *Atmospheric Environment*, **29 (11)**, 1185 – 1193, doi: 10.1016/1352-2310(94)00210-C.

Gawarkiewicz, G., and Coauthors, 2018: The Changing Nature of Shelf-Break Exchange Revealed by the OOI Pioneer Array. *Oceanography*, **31 (1)**, 60 – 70, URL `http://www.jstor.org/stable/26307788`.

Gawarkiewicz, G. G., R. E. Todd, A. J. Plueddemann, M. Andres, and J. P. Manning, 2012: Direct interaction between the Gulf Stream and the shelfbreak south of New England. *Scientific Reports*, **2**, 553, doi: 10.1038/srep00553.

Glenn, S. M., and C. C. Ebbesmeyer, 1994: Observations of Gulf Stream frontal eddies in the vicinity of Cape Hatteras. *Journal of Geophysical Research*, **99 (C3)**, 5047 – 5055, doi: 10.1029/93JC02787.

Goni, G., and Coauthors, 2010: The ship of opportunity program. *Proceedings of OceanObs '09: Sustained Ocean Observations and Information for Society*, J. Hall, D. Harrison, and D. Stammer, Eds., ESA Publication WPP-306, Venice, Italy, 21-25 September 2009, Vol. 2, doi: 10.5270/OceanObs09.cwp.35.

Gula, J., T. M. Blacic, and R. E. Todd, 2019: Submesoscale Coherent Vortices in the Gulf Stream. *Geophysical Research Letters*, **46 (5)**, 2704 – 2714, doi: 10.1029/2019GL081919.

Gula, J., M. J. Molemaker, and J. C. McWilliams, 2015: Gulf Stream Dynamics along the Southeastern U.S. Seaboard. *Journal of Physical Oceanography*, **45 (3)**, 690 – 715, doi: 10.1175/JPO-D-14-0154.1.

Halkin, D., and T. Rossby, 1985: The Structure and Transport of the Gulf Stream at 73°W. *Journal of Physical Oceanography*, **15 (11)**, 1439 – 1452, doi: 10.1175/1520-0485(1985)015<1439:TSATOT>2.0.CO;2.

Hall, M. M., and H. L. Bryden, 1985: Profiling the Gulf Stream with a current meter mooring. *Geophysical Research Letters*, **12 (4)**, 203 – 206, doi: 10.1029/GL012i004p00203.

Hansen, D. V., 1970: Gulf stream meanders between Cape Hatteras and the Grand Banks. *Deep Sea Research and Oceanographic Abstracts*, **17 (3)**, 495 – 511, doi: 10.1016/0011-7471(70)90064-1.

Heiderich, J., and R. E. Todd, 2020: Along-Stream Evolution of Gulf Stream Volume Transport. *Journal of Physical Oceanography*, **50 (8)**, 2251 – 2270, doi: 10.1175/JPO-D-19-0303.1.

Hoarfrost, A., J. P. Balmonte, S. Ghobrial, K. Ziervogel, J. Bane, G. Gawarkiewicz, and C. Arnosti, 2019: Gulf Stream Ring Water Intrusion on the Mid-Atlantic Bight Continental Shelf Break Affects Microbially Driven Carbon Cycling. *Frontiers in Marine Science*, **6**, 394, doi: 10.3389/fmars.2019.00394.

Hogg, N. G., 1992: On the transport of the Gulf Stream between Cape Hatteras and the Grand Banks. *Deep Sea Research Part A. Oceanographic Research Papers*, **39 (7)**, 1231 – 1246, doi: 10.1016/0198-0149(92)90066-3.

Hogg, N. G., 1993: Toward parameterization of the eddy field near the Gulf Stream. *Deep Sea Research Part I: Oceanographic Research Papers*, **40 (11)**, 2359 – 2376, doi: 10.1016/0967-0637(93)90110-O.

Hogg, N. G., R. S. Pickart, R. M. Hendry, and W. J. Smethie, Jr., 1986: The Northern Recirculation Gyre of the Gulf Stream. *Deep Sea Research Part A. Oceanographic Research Papers*, **33 (9)**, 1139 – 1165, doi: 10.1016/0198-0149(86)90017-8.

Hogg, N. G., and H. Stommel, 1985: On the relation between the deep circulation and the Gulf Stream. *Deep Sea Research Part I: Oceanographic Research Papers*, **32 (10)**, 1181 – 1193, doi: 10.1016/0198-0149(85)90002-0.

Holland, W. R., 1972: Baroclinic and topographic influences on the transport in western boundary currents. *Geophysical Fluid Dynamics*, **4 (1)**, 187 – 210, doi: 10.1080/03091927208236095.

Holland, W. R., and P. B. Rhines, 1980: An Example of Eddy-Induced Ocean Circulation. *Journal of Physical Oceanography*, **10 (7)**, 1010 – 1031, doi: 10.1175/1520-0485(1980)010<1010:AEOEIO>2.0.CO;2.

Hood, C. A., and J. M. Bane, Jr., 1983: Subsurface Energetics of the Gulf Stream Cyclonic Frontal Zone off Onslow Bay, North Carolina. *Journal of Geophysical Research*, **88 (C8)**, 4651 – 4662, doi: 10.1029/JC088iC08p04651.

IPCC, 2013: *Climate Change 2013: The Physical Science Basis. Contribution of Working Group I to the Fifth Assessment Report of the Intergovernmental Panel on Climate Change*. Cambridge University Press, 1535 pp., doi: 10.1017/CBO9781107415324.

Iselin, C. O'D., 1940: Preliminary Report on the Long-Period Variations in the Transport of the Gulf Stream System. *Papers in Physical Oceanography and Meteorology*, **8 (1)**.

Johns, E., D. R. Watts, and H. T. Rossby, 1989: A Test of Geostrophy in the Gulf Stream. *Journal of Geophysical Research: Oceans*, **94 (C3)**, 3211 – 3222, doi: 10.1029/JC094iC03p03211.

Johns, W. E., T. J. Shay, J. M. Bane, and D. R. Watts, 1995: Gulf Stream structure, transport, and recirculation near 68°W. *Journal of Geophysical Research: Oceans*, **100 (C1)**, 817 – 838, doi: 10.1029/94JC02497.

Joyce, T. M., C. Deser, and M. A. Spall, 2000: The Relation between Decadal Variability of Subtropical Mode Water and the North Atlantic Oscillation. *Journal of Climate*, **13 (14)**, 2550 – 2569, doi: 10.1175/1520-0442(2000)013<2550:TRBDVO>2.0.CO;2.

Klymak, J. M., and Coauthors, 2016: Submesoscale streamers exchange water on the north wall of the Gulf Stream. *Geophysical Research Letters*, **43 (3)**, 1226 – 1233, doi: 10.1002/2015GL067152.

Knauss, J. A., 1969: A note on the transport of the Gulf Stream. *Deep-Sea Research*, **16 (Suppl.)**, 117 – 123.

Krug, M., S. Swart, and J. Gula, 2017: Submesoscale cyclones in the Agulhas current. *Geophysical Research Letters*, **44 (1)**, 346 – 354, doi: 10.1002/2016GL071006.

Kunze, E., E. Firing, J. M. Hummon, T. K. Chereskin, and A. M. Thurnherr, 2006: Global Abyssal Mixing Inferred from Lowered ADCP Shear and CTD Strain Profiles. *Journal of Physical Oceanography*, **36 (8)**, 1553 – 1576, doi: 10.1175/JPO2926.1.

Kwon, Y.-O., M. A. Alexander, N. A. Bond, C. Frankignoul, H. Nakamura, B. Qiu, and L. A. Thompson, 2010: Role of the Gulf Stream and Kuroshio–Oyashio Systems in Large-Scale Atmosphere–Ocean Interaction: A Review. *Journal of Climate*, **23 (12)**, 3249 – 3281, doi: 10.1175/2010JCLI3343.1.

Le Bras, I. A., I. Yashayaev, and J. M. Toole, 2017: Tracking Labrador Sea Water property signals along the Deep Western Boundary Current. *Journal of Geophysical Research: Oceans*, **122 (7)**, 5348 – 5366, doi: 10.1002/2017JC012921.

Leaman, K. D., E. Johns, and T. Rossby, 1989: The Average Distribution of Volume Transport and Potential Vorticity with Temperature at Three Sections across the

Gulf Stream. *Journal of Physical Oceanography*, **19 (1)**, 36 – 51, doi: 10.1175/1520-0485(1989)019<0036:TADOVT>2.0.CO;2.

Lee, T. N., and L. P. Atkinson, 1983: Low-frequency current and temperature variability from Gulf Stream frontal eddies and atmospheric forcing along the southeast U.S. outer continental shelf. *Journal of Geophysical Research*, **88 (C8)**, 4541 – 4567, doi: 10.1029/JC088iC08p04541.

Lee, T. N., L. P. Atkinson, and R. Legeckis, 1981: Observations of a Gulf Stream frontal eddy on the Georgia continental shelf, April 1977. *Deep-Sea Research*, **28A (4)**, 347 – 378, doi: 10.1016/0198-0149(81)90004-2.

Lee, T. N., J. A. Yoder, and L. P. Atkinson, 1991: Gulf Stream Frontal Eddy Influence on Productivity of the Southeast U.S. Continental Shelf. *Journal of Geophysical Research*, **96 (C12)**, 22 191 – 22 205, doi: 10.1029/91JC02450.

Legeckis, R., 1975: Application of synchronous meteorological satellite data to the study of time dependent sea surface temperature changes along the boundary of the Gulf Stream. *Geophysical Research Letters*, **2 (10)**, 435 – 438, doi: 10.1029/GL002i010p00435.

Lentz, S. J., 2008: Observations and a Model of the Mean Circulation over the Middle Atlantic Bight Continental Shelf. *Journal of Physical Oceanography*, **38 (6)**, 1203 – 1221, doi: 10.1175/2007JPO3768.1.

Levine, E. R., D. N. Connors, P. C. Cornillon, and H. T. Rossby, 1986: Gulf Stream Kinematics along an Isopycnal Float Trajectory. *Journal of Physical Oceanography*, **16 (7)**, 1317 – 1328, doi: 10.1175/1520-0485(1986)016<1317:GSKAAI>2.0.CO;2.

Lillibridge, J. L., III, and A. J. Mariano, 2013: A statistical analysis of Gulf Stream variability from 18+ years of altimetry data. *Deep Sea Research Part II: Topical Studies in Oceanography*, **85**, 127 – 146, doi: 10.1016/j.dsr2.2012.07.034.

Linder, C. A., and G. Gawarkiewicz, 1998: A climatology of the shelfbreak front in the Middle Atlantic Bight. *Journal of Geophysical Research: Oceans*, **103 (C9)**, 18 405 – 18 423, doi: 10.1029/98JC01438.

MacLeish, W. H., 1989: *The Gulf Stream: Encounters with the Blue God*. Houghton Mifflin Harcourt.

Maul, G. A., F. Chew, M. Bushnell, and D. A. Mayer, 1985: Sea Level Variation as an Indicator of Florida Current Volume Transport: Comparisons with Direct Measurements. *Science*, **227 (4684)**, 304 – 307, doi: 10.1126/science.227.4684.304.

Maul, G. A., D. A. Mayer, and M. Bushnell, 1990: Statistical Relationships Between Local Sea Level and Weather With Florida-Bahamas Cable and Pegasus Measurements of Florida Current Volume Transport. *Journal of Geophysical Research: Oceans*, **95 (C3)**, 3287 – 3296, doi: 10.1029/JC095iC03p03287.

Meinen, C. S., M. O. Baringer, and R. F. Garcia, 2010: Florida Current transport variability: An analysis of annual and longer-period signals. *Deep Sea Research Part I: Oceanographic Research Papers*, **57 (7)**, 835 – 846, doi: 10.1016/j.dsr.2010.04.001.

Meinen, C. S., and D. S. Luther, 2016: Structure, transport, and vertical coherence of the Gulf Stream from the Straits of Florida to the Southeast Newfoundland Ridge. *Deep Sea Research Part I: Oceanographic Research Papers*, **112**, 137 – 154, doi: 10.1016/j.dsr.2016.03.002.

Meinen, C. S., R. H. Smith, and R. F. Garcia, 2021: Evaluating pressure gauges as a potential future replacement for electromagnetic cable observations of the Florida Current transport at 27°N. *Journal of Operational Oceanography*, **14 (2)**, 166 – 176, doi: 10.1080/1755876X.2020.1780757.

Meinen, C. S., and Coauthors, 2019: Structure and Variability of the Antilles Current at 26.5°N. *Journal of Geophysical Research: Oceans*, **124 (6)**, 3700 – 3723, doi: 10.1029/2018JC014836.

Mellor, G. L., and T. Ezer, 1991: A Gulf Stream model and an altimetry assimilation scheme. *Journal of Geophysical Research*, **96 (C5)**, 8779 – 8795, doi: 10.1029/91JC00383.

Minnett, P., and Coauthors, 2019: Half a century of satellite remote sensing of sea-surface temperature. *Remote Sensing of Environment*, **233**, 111 366, doi: 10.1016/j.rse.2019.111366.

Molinari, R. L., 2011: Information from low-density expendable bathythermograph transects: North Atlantic mean temperature structure and quasi-decadal variability. *Progress in Oceanography*, **88 (1)**, 131 – 149, doi: 10.1016/j.pocean.2010.12.013.

Munk, W. H., 1950: On the wind-driven circulation. *Journal of Meteorology*, **7 (2)**, 80 – 93, doi: 10.1175/1520-0469(1950)007<0080:OTWDOC>2.0.CO;2.

Munk, W. H., 1966: Abyssal recipes. *Deep-Sea Research*, **13 (4)**, 707 – 730, doi: 10.1016/0011-7471(66)90602-4.

Neumann, G., 1960: On the Dynamical Structure of the Gulf Stream as an Equivalent-Barotropic Flow. *Journal of Geophysical Research*, **65 (1)**, 239 – 247, doi: 10.1029/JZ065i001p00239.

Noble, M. A., and G. R. Gelfenbaum, 1992: Seasonal Fluctuations in Sea Level on the South Carolina Shelf and Their Relationship to the Gulf Stream. *Journal of Geophysical Research*, **97 (C6)**, 9521 – 9529, doi: 10.1029/92JC00811.

Oort, A. H., 1964: Computations of the eddy heat and density transports across the Gulf Stream. *Tellus*, **16 (1)**, 55 – 63, doi: 10.1111/j.2153-3490.1964.tb00143.x.

Palter, J. B., and M. S. Lozier, 2008: On the source of Gulf Stream nutrients. *Journal of Geophysical Research: Oceans*, **113 (C6)**, doi: 10.1029/2007JC004611.

Parsons, A. T., 1969: A two-layer model of Gulf Stream separation. *Journal of Fluid Mechanics*, **39 (3)**, 511 – 528, doi: 10.1017/S0022112069002308.

Pickart, R. S., and W. M. Smethie, Jr., 1993: How Does the Deep Western Boundary Current Cross the Gulf Stream? *Journal of Physical Oceanography*, **23 (12)**, 2602 – 2616, doi: 10.1175/1520-0485(1993)023<2602:HDTDWB>2.0.CO;2.

Pickart, R. S., and D. R. Watts, 1990: Deep Western Boundary Current variability at Cape Hatteras. *Journal of Marine Research*, **48 (4)**, 765 – 791.

Pickart, R. S., and D. R. Watts, 1993: Gulf Stream Meanders Over Steep Topography. *Journal of Geophysical Research: Oceans*, **98 (C4)**, 6895 – 6905, doi: 10.1029/92JC02792.

Piecuch, C. G., 2020: Likely weakening of the Florida Current during the past century revealed by sea-level observations. *Nature Communications*, **11 (1)**, 3973, doi: 10.1038/s41467-020-17761-w.

Polzin, K. L., J. M. Toole, J. R. Ledwell, and R. W. Schmitt, 1997: Spatial Variability of Turbulent Mixing in the Abyssal Ocean. *Science*, **276 (5309)**, 93 – 96, doi: 10.1126/science.276.5309.93.

Pratt, R. M., 1963: Bottom currents on the Blake Plateau. *Deep Sea Research*, **10 (3)**, 245 – 249, doi: 10.1016/0011-7471(63)90360-7.

Pujol, M.-I., Y. Faugère, G. Taburet, S. Dupuy, C. Pelloquin, M. Ablain, and N. Picot, 2016: DUACS DT2014: the new multi-mission altimeter data set reprocessed over 20 years. *Ocean Science*, **12 (5)**, 1067 – 1090, doi: 10.5194/os-12-1067-2016.

Qu, T., S. Gao, and I. Fukumori, 2013: Formation of salinity maximum water and its contribution to the overturning circulation in the North Atlantic as revealed by a global general circulation model. *Journal of Geophysical Research: Oceans*, **118 (4)**, 1982 – 1994, doi: 10.1002/jgrc.20152.

Rainville, L., C. M. Lee, D. L. Rudnick, and K.-C. Yang, 2013: Propagation of internal tides generated near Luzon Strait: Observations from autonomous gliders. *Journal of Geophysical Research: Oceans*, **118 (9)**, 4125 – 4138, doi: 10.1002/jgrc.20293.

Redfield, A. C., 1936: An Ecological Aspect of the Gulf Stream. *Nature*, **138 (3502)**, 1013, doi: 10.1038/1381013a0.

Rhein, M., D. Kieke, and R. Steinfeldt, 2015: Advection of North Atlantic Deep Water from the Labrador Sea to the southern hemisphere. *Journal of Geophysical Research: Oceans*, **120 (4)**, 2471 – 2487, doi: 10.1002/2014JC010605.

Rhines, P. B., and W. R. Holland, 1979: A theoretical discussion of eddy-driven mean flows. *Dynamics of Atmospheres and Oceans*, **3 (2)**, 289 – 325, doi: 10.1016/0377-0265(79)90015-0.

Richardson, P. L., 1985: Average velocity and transport of the Gulf Stream near 55°W. *Journal of Marine Research*, **43 (1)**, 83 – 111, doi: 10.1357/002224085788437343.

Richardson, P. L., and N. T. Adams, 2018: Uncharted Waters – Nantucket Whalers and the Franklin-Folger Chart of the Gulf Stream. *Historic Nantucket*, **68 (1)**, 17 – 24.

Rossby, T., 1987: On the energetics of the Gulf Stream at 73W. *Journal of Marine Research*, **45 (1)**, 59 – 82, doi: 10.1357/002224087788400918.

Rossby, T., and R. L. Benway, 2000: Slow variations in mean path of the Gulf Stream east of Cape Hatteras. *Geophysical Research Letters*, **27 (1)**, 117 – 120, doi: 10.1029/1999GL002356.

Rossby, T., C. Flagg, and K. Donohue, 2010: On the variability of Gulf Stream transport from seasonal to decadal timescales. *Journal of Marine Research*, **68 (3 – 4)**, 503 – 522, doi: 10.1357/002224010794657128.

Rossby, T., C. N. Flagg, K. Donohue, A. Sanchez-Franks, and J. Lillibridge, 2014: On the long-term stability of Gulf Stream transport based on 20 years of direct measurements. *Geophysical Research Letters*, **41 (1)**, 114 – 120, doi: 10.1002/2013GL058636.

Rudnick, D. L., 2016: Ocean Research Enabled by Underwater Gliders. *Annual Review of Marine Science*, **8 (1)**, 519 – 541, doi: 10.1146/annurev-marine-122414-033913.

Rudnick, D. L., and S. T. Cole, 2011: On sampling the ocean using underwater gliders. *Journal of Geophysical Research: Oceans*, **116 (C8)**, C08010, doi: 10.1029/2010JC006849.

Rudnick, D. L., R. E. Davis, C. C. Eriksen, D. M. Fratantoni, and M. J. Perry, 2004: Underwater Gliders for Ocean Research. *Marine Technology Society Journal*, **38 (2)**, 73 – 84, doi: 10.4031/002533204787522703.

Rudnick, D. L., R. E. Davis, and J. T. Sherman, 2016: Spray Underwater Glider Operations. *Journal of Atmospheric and Oceanic Technology*, **33 (6)**, 1113 – 1122, doi: 10.1175/JTECH-D-15-0252.1.

Rudnick, D. L., T. M. S. Johnston, and J. T. Sherman, 2013: High-frequency internal waves near the Luzon Strait observed by underwater gliders. *Journal of Geophysical Research: Oceans*, **118 (2)**, 774 – 784, doi: 10.1002/jgrc.20083.

Rudnick, D. L., J. T. Sherman, and A. P. Wu, 2018: Depth-Average Velocity from Spray Underwater Gliders. *Journal of Atmospheric and Oceanic Technology*, **35 (8)**, 1665 – 1673, doi: 10.1175/JTECH-D-17-0200.1.

Rudnick, D. L., K. D. Zaba, R. E. Todd, and R. E. Davis, 2017: A climatology of the California Current System from a network of underwater gliders. *Progress in Oceanography*, **154**, 64 – 106, doi: 10.1016/j.pocean.2017.03.002.

Sanchez-Franks, A., C. N. Flagg, and T. Rossby, 2014: A comparison of transport and position between the Gulf Stream east of Cape Hatteras and the Florida Current. *Journal of Marine Research*, **72 (4)**, 291 – 306, doi: 10.1357/002224014815460641.

Schaeffer, A., and M. Roughan, 2015: Influence of a western boundary current on shelf dynamics and upwelling from repeat glider deployments. *Geophysical Research Letters*, **42 (1)**, 121 – 128, doi: 10.1002/2014GL062260.

Schmittner, A., and E. D. Galbraith, 2008: Glacial greenhouse-gas fluctuations controlled by ocean circulation changes. *Nature*, **456**, 373 – 376, doi: 10.1038/nature07531.

Schmitz, W. J., Jr., and P. P. Niiler, 1969: A note on the kinetic energy exchange between fluctuations and mean flow in the surface layer of the Florida current. *Tellus*, **21 (6)**, 814–819, doi: 10.3402/tellusa.v21i6.10147.

Schönau, M. C., D. L. Rudnick, I. Cerovecki, G. Gopalakrishnan, B. D. Cornuelle, J. L. McClean, and B. Qiu, 2015: The Mindanao Current: Mean Structure and Connectivity. *Oceanography*, **28 (4)**, 34 – 45, doi: 10.5670/oceanog.2015.79.

Schott, F., and R. Zantopp, 1985: Florida Current: Seasonal and Interannual Variability. *Science*, **227 (4684)**, 308 – 311, doi: 10.1126/science.227.4684.308.

Schott, F. A., T. N. Lee, and R. Zantopp, 1988: Variability of Structure and Transport of the Florida Current in the Period Range of Days to Seasonal. *Journal of Physical Oceanography*, **18 (9)**, 1209 – 1230, doi: 10.1175/1520-0485(1988)018<1209:VOSATO>2.0.CO;2.

Shay, T. J., J. M. Bane, D. R. Watts, and K. L. Tracey, 1995: Gulf Stream flow field and events near 68°W. *Journal of Geophysical Research: Oceans*, **100 (C11)**, 22 565 – 22 589, doi: 10.1029/95JC02685.

Sherman, J., R. E. Davis, W. B. Owens, and J. Valdes, 2001: The Autonomous Underwater Glider "Spray". *IEEE Journal of Oceanic Engineering*, **26 (4)**, 437 – 446, doi: 10.1109/48.972076.

Shoosmith, D. R., M. O. Baringer, and W. E. Johns, 2005: A continuous record of Florida Current temperature transport at 27°N. *Geophysical Research Letters*, **32 (23)**, L23603, doi: 10.1029/2005GL024075.

Spall, M. A., 1996a: Dynamics of the Gulf Stream/Deep Western Boundary Current Crossover. Part I: Entrainment and Recirculation. *Journal of Physical Oceanography*, **26 (10)**, 2152 – 2168, doi: 10.1175/1520-0485(1996)026<2152:DOTGSW>2.0.CO;2.

Spall, M. A., 1996b: Dynamics of the Gulf Stream/Deep Western Boundary Current Crossover. Part II: Low-Frequency Internal Oscillations. *Journal of Physical Oceanography*, **26 (10)**, 2169 – 2182, doi: 10.1175/1520-0485(1996)026<2169:DOTGSW>2.0.CO;2.

Stammer, D., and J. Theiss, 2004: Velocity Statistics Inferred from the TOPEX/Poseidon-Jason-1 Tandem Mission Data. *Marine Geodesy*, **27 (3-4)**, 551 – 575, doi: 10.1080/01490410490902052.

Stommel, H., 1948: The westward intensification of wind-driven ocean currents. *Eos Transactions American Geophysical Union*, **29 (2)**, 202 – 206, doi: 10.1029/TR029i002p00202.

Stommel, H., and A. B. Arons, 1959: On the abyssal circulation of the world ocean – I. Stationary planetary flow patterns on a sphere. *Deep Sea Research (1953)*, **6 (Supplement C)**, 140 – 154, doi: 10.1016/0146-6313(59)90065-6.

Strong, A. E., E. J. Kearns, and K. K. Gjovig, 2000: Sea surface temperature signals from satellites – an update. *Geophysical Research Letters*, **27 (11)**, 1667 – 1670, doi: 10.1029/1999GL002392.

Sverdrup, H. U., 1947: Wind-driven currents in a baroclinic ocean; with application to the equatorial currents of the eastern Pacific. *Proceedings of the National Academy of Sciences*, **33 (11)**, 318 – 326, doi: 10.1073/pnas.33.11.318.

Szuts, Z. B., and C. S. Meinen, 2017: Florida Current Salinity and Salinity Transport: Mean and Decadal Changes. *Geophysical Research Letters*, **44 (20)**, 10 495 – 10 503, doi: 10.1002/2017GL074538.

Talley, L. D., and M. S. McCartney, 1982: Distribution and Circulation of Labrador Sea Water. *Journal of Physical Oceanography*, **12 (11)**, 1189 – 1205, doi: 10.1175/1520-0485(1982)012<1189:DACOLS>2.0.CO;2.

Talley, L. D., G. L. Pickard, W. J. Emery, and J. H. Swift, 2011: *Descriptive Physical Oceanography: An Introduction*. 6th ed., Academic Press, doi: 10.1016/C2009-0-24322-4.

Thompson, J. D., and W. J. Schmitz, Jr., 1989: A Limited-Area Model of the Gulf Stream: Design, Initial Experiments, and Model-Data Intercomparison. *Journal of Physical Oceanography*, **19 (6)**, 791 – 814, doi: 10.1175/1520-0485(1989)019<0791:ALAMOT>2.0.CO;2.

Thyng, K. M., C. A. Greene, R. D. Hetland, H. M. Zimmerle, and S. F. DiMarco, 2016: True Colors of Oceanography: Guidelines for Effective and Accurate Colormap Selection. *Oceanography*, **29 (3)**, 9 – 13, doi: 10.5670/oceanog.2016.66.

Todd, R. E., 2017: High-frequency internal waves and thick bottom mixed layers observed by gliders in the Gulf Stream. *Geophysical Research Letters*, **44 (12)**, 6316 – 6325, doi: 10.1002/2017GL072580.

Todd, R. E., 2020: Export of Middle Atlantic Bight Shelf Waters Near Cape Hatteras From Two Years of Underwater Glider Observations. *Journal of Geophysical Research: Oceans*, **125**, e2019JC016 006, doi: 10.1029/2019JC016006.

Todd, R. E., 2021: Gulf Stream Mean and Eddy Kinetic Energy: Three-Dimensional Estimates From Underwater Glider Observations. *Geophysical Research Letters*, **48 (6)**, 2020GL090 281, doi: 10.1029/2020GL090281.

Todd, R. E., T. G. Asher, J. Heiderich, J. M. Bane, and R. A. Luettich, 2018: Transient Response of the Gulf Stream to Multiple Hurricanes in 2017. *Geophysical Research Letters*, **45 (19)**, 10 509 – 10 519, doi: 10.1029/2018GL079180.

Todd, R. E., and L. Locke-Wynn, 2017: Underwater Glider Observations and the Representation of Western Boundary Currents in Numerical Models. *Oceanography*, **30 (2)**, 88 – 89, doi: 10.5670/oceanog.2017.225.

Todd, R. E., and W. B. Owens, 2016: Gliders in the Gulf Stream. Scripps Institution of Oceanography, Instrument Development Group, Publicly available dataset, doi: 10.21238/S8SPRAY2675.

Todd, R. E., W. B. Owens, and D. L. Rudnick, 2016: Potential Vorticity Structure in the North Atlantic Western Boundary Current from Underwater Glider Observations. *Journal of Physical Oceanography*, **46 (1)**, 327 – 348, doi: 10.1175/JPO-D-15-0112.1.

Todd, R. E., D. L. Rudnick, M. R. Mazloff, R. E. Davis, and B. D. Cornuelle, 2011: Poleward flows in the southern California Current System: Glider observations and numerical simulation. *Journal of Geophysical Research*, **116 (C2)**, C02026, doi: 10.1029/2010JC006536.

Todd, R. E., D. L. Rudnick, J. T. Sherman, W. B. Owens, and L. George, 2017: Absolute Velocity Estimates from Autonomous Underwater Gliders Equipped with Doppler Current Profilers. *Journal of Atmospheric and Oceanic Technology*, **34 (2)**, 309 – 333, doi: 10.1175/JTECH-D-16-0156.1.

Todd, R. E., and Coauthors, 2019: Global Perspectives on Observing Ocean Boundary Current Systems. *Frontiers in Marine Science*, **6**, 423, doi: 10.3389/fmars.2019.00423.

Toole, J. M., M. Andres, I. A. Le Bras, T. M. Joyce, and M. S. McCartney, 2017: Moored observations of the Deep Western Boundary Current in the NW Atlantic: 2004 – 2014. *Journal of Geophysical Research: Oceans*, **122 (9)**, 7488 – 7505, doi: 10.1002/2017JC012984.

Toole, J. M., R. G. Curry, T. M. Joyce, M. McCartney, and B. Peña-Molino, 2011: Transport of the North Atlantic Deep Western Boundary Current about 39°N, 70°W: 2004 – 2008. *Deep Sea Research Part II: Topical Studies in Oceanography*, **58 (17 – 18)**, 1768 – 1780, doi: 10.1016/j.dsr2.2010.10.058.

Tsuchiya, M., 1989: Circulation of the Antarctic Intermediate Water in the North Atlantic Ocean. *Journal of Marine Research*, **47 (4)**, 747 – 755, doi: 10.1357/002224089785076136.

Vellinga, M., and R. A. Wood, 2008: Impacts of thermohaline circulation shutdown in the twenty-first century. *Climatic Change*, **91 (1)**, 43 – 63, doi: 10.1007/s10584-006-9146-y.

Vignudelli, S., F. Birol, J. Benveniste, L.-L. Fu, N. Picot, M. Raynal, and H. Roinard, 2019: Satellite Altimetry Measurements of Sea Level in the Coastal Zone. *Surveys in Geophysics*, **40 (6)**, 1319 – 1349, doi: 10.1007/s10712-019-09569-1.

Visbeck, M., 2002: Deep Velocity Profiling Using Lowered Acoustic Doppler Current Profilers: Bottom Track and Inverse Solutions. *Journal of Atmospheric and Oceanic Technology*, **19 (5)**, 794 – 807, doi: 10.1175/1520-0426(2002)019<0794:DVPULA>2.0.CO;2.

Volkov, D. L., R. Domingues, C. S. Meinen, R. Garcia, M. Baringer, G. Goni, and R. H. Smith, 2020: Inferring Florida Current Volume Transport From Satellite Altimetry. *Journal of Geophysical Research: Oceans*, **125 (12)**, e2020JC016 763, doi: 10.1029/2020JC016763.

Waterhouse, A. F., and Coauthors, 2014: Global Patterns of Diapycnal Mixing from Measurements of the Turbulent Dissipation Rate. *Journal of Physical Oceanography*, **44 (7)**, 1854 – 1872, doi: 10.1175/JPO-D-13-0104.1.

Watts, D. R., and W. E. Johns, 1982: Gulf Stream Meanders: Observations on Propagation and Growth. *Journal of Geophysical Research: Oceans*, **87 (C12)**, 9467 – 9476, doi: 10.1029/JC087iC12p09467.

Watts, D. R., K. L. Tracey, J. M. Bane, and T. J. Shay, 1995: Gulf Stream path and thermocline structure near 74°W and 68°W. *Journal of Geophysical Research: Oceans*, **100 (C9)**, 18 291 – 18 312, doi: 10.1029/95JC01850.

Webster, F., 1961: A description of Gulf Stream Meanders off Onslow Bay. *Deep Sea Research (1953)*, **8 (2)**, 130 – 143, doi: 10.1016/0146-6313(61)90005-3.

Webster, F., 1965: Measurements of eddy fluxes of momentum in the surface layer of the Gulf Stream. *Tellus*, **17 (2)**, 240 – 245, doi: 10.3402/tellusa.v17i2.9030.

Williams, R. G., 2012: Centennial warming of ocean jets. *Nature Climate Change*, **2 (3)**, 149 – 150, doi: 10.1038/nclimate1393.

Worst, J. S., K. A. Donohue, and T. Rossby, 2014: A Comparison of Vessel-Mounted Acoustic Doppler Current Profiler and Satellite Altimeter Estimates of Sea Surface Height and Transports between New Jersey and Bermuda along the CMV *Oleander* Route. *Journal of Atmospheric and Oceanic Technology*, **31 (6)**, 1422 – 1433, doi: 10.1175/JTECH-D-13-00122.1.

Worthington, L. V., 1959: The 18° water in the Sargasso Sea. *Deep Sea Research*, **5 (2)**, 297 – 305, doi: 10.1016/0146-6313(58)90026-1.

Worthington, L. V., 1976: *On the North Atlantic Circulation*, Vol. 6. The Johns Hopkins University Press, 110 pp.

Wunsch, C., 2005: The Total Meridional Heat Flux and Its Oceanic and Atmospheric Partition. *Journal of Climate*, **18 (21)**, 4374 – 4380, doi: 10.1175/JCLI3539.1.

Wunsch, C., and D. Roemmich, 1985: Is the North Atlantic in Sverdrup Balance? *Journal of Physical Oceanography*, **15 (12)**, 1876 – 1880, doi: 10.1175/1520-0485(1985)015<1876:ITNAIS>2.0.CO;2.

Wyrtki, K., L. Magaard, and J. Hager, 1976: Eddy Energy in the Oceans. *Journal of Geophysical Research*, **81 (15)**, 2641 – 2646, doi: 10.1029/JC081i015p02641.

Yang, H., G. Lohmann, W. Wei, M. Dima, M. Ionita, and J. Liu, 2016: Intensification and poleward shift of subtropical western boundary currents in a warming climate. *Journal of Geophysical Research: Oceans*, **121 (7)**, 4928 – 4945, doi: 10.1002/2015JC011513.

Yoder, J. A., L. P. Atkinson, S. Stephen Bishop, E. E. Hofmann, and T. N. Lee, 1983: Effect of upwelling on phytoplankton productivity of the outer southeastern United States continental shelf. *Continental Shelf Research*, **1 (4)**, 385 – 404, doi: 10.1016/0278-4343(83)90004-3.

Zeng, X., and R. He, 2016: Gulf Stream variability and a triggering mechanism of its large meander in the South Atlantic Bight. *Journal of Geophysical Research: Oceans*, **121 (11)**, 8021 – 8038, doi: 10.1002/2016JC012077.